A radiotherapy compatible QA phantom for HIFU

UCL

PhD in Medical Physics and Biomedical engineering

I confirm that the work presented in this thesis is my own. Where information has been derived from other sources, I confirm that this has been indicated in the thesis.

Abstract

In order to produce a phantom that would be suited for combined radiotherapy and HIFU quality assurance, a gellan gum-based tissue mimicking material (TMM) has been developed. Gellan gum is a material that has been used for the creation of acoustic phantoms but has not been applied to any radiotherapy work. The TMM's acoustic properties have been characterized. Geared toward enabling it to perform metrology of acoustic sources, a thermochromic variant has been developed. The thermochromic and non-thermochromic variants of the TMM have been compared in terms of their acoustic properties to ensure that the materials could be combined for the creation of phantoms. To test the TMM's applicability to radiotherapy applications the samples have been characterized pre- and post-irradiation (up to 3kGy) to ensure the applicability of the phantom to uses that require the material be exposed to ionizing radiation. The TMM has also been characterized in terms of its Hounsfield Units to assess its possible use as a phantom for radiation applications, and a comparison of measured and simulated attenuation has been used to verify that the effective atomic number is similar to that of human tissues. The TMMs have been combined for the development of a Quality Assurance (QA) phantom for an ultrasound guided HIFU therapy. A QA process has been developed, with associated software, which allows a simple QA process that can identify changes in power output and assess the targeting capabilities of an US-guided thermal therapy inexpensively. The thermochromic TMM has also been applied to the detection of the focal position in a mouse skull phantom. The materials have been shown to be applicable to both combined, and separate, radiotherapy and HIFU applications, as well as to ultrasound guided therapies.

IMPACT STATEMENT

The characterization of the various materials with different compositions is a valuable resource for any research laboratory in need of materials for evaluation of equipment and exposures, be they acoustic, radiological or both. This project includes detailed characterization of the materials at different concentrations and temperatures, thus facilitating any future work based on their use. It also includes evaluation of their response up to doses of 3kGy, which encompasses a good amount of radiation work. The material's thermochromic properties would be useful to other non-acoustic thermal methods. The phantom designed is not only applicable to the QA of the specific equipment for which it was designed, but also for any other ultrasound guided ultrasound therapies. The application to QA processes will provide valuable information to ensure that medical equipment is capable of delivering treatment to patients and test its accuracy. The modular design and its principles make it a versatile tool that could be adjusted for different applications. The manufacturing of the phantom offers an avenue for commercialization that could be streamlined and offered to clients in need of the evaluation of similar equipment.

Contents

List of figures

List of tables

List of equations

List of Abbreviations

BBB	Blood-Brain Barrier
CT	Computerized Tomography
DNA	Deoxyribonucleic acid
EBRT	External Beam Radiotherapy
FAIS	Finite Amplitude Insertion Substitution
FUS	Focused Ultrasound
GG	Gellan Gum
HIFU	High Intensity Focused Ultrasound
HU	Hounsfield Units
HVL	Half Value Layer
IAEA	International Atomic Energy Agency
MLC	Multileaf Collimator
MR	Magnetic Resonance
MU	Monitor Units
OAR	Organ At Risk
PAA	Polyacrylamide
PDD	Percentage Depth Dose
PVA	Polyvinyl alcohol
QA	Quality Assurance
SiO	Silicon Oxide
SoS	Speed of Sound
SSD	Source Skin Distance
TMM	Tissue mimicking material
TTTS	Twin-to-Twin Transfusion Syndrome
UI	User Interface

US	Ultrasound
ZnOAc	Zinc Acetate

1. Introduction

Radiotherapy is a therapeutic modality that relies on the use of high energy photon interactions with matter in order to deliver energy to the body with the aim of causing biological damage[1].

High Intensity Focused Ultrasound (HIFU) is a therapy that makes use of high frequency acoustic pressure waves to produce biological effect[2]. The energy is focused into small volumes in which the acoustic energy is absorbed, resulting in heating. These foci tend to be small[3], on the scale of the wavelength, λ, of the sound wave (λ=1mm for a frequency, f, of 1.5MHz), and so covering large volumes becomes time consuming. Regions in the path of the beam can be unintentionally heated during exposure[2] which can lead, for example, to skin burns. Bone and air-filled regions, such as the lungs, limit the access of ultrasound therapy to underlying structures, due to the reflection of ultrasound[2]. The attenuation of the wave energy as it propagates limits the depth at which a focus can be generated.

Radiotherapy is limited by opposite phenomena, since the energy distribution becomes more diffuse as beams propagate through tissue[1]. Treatments are then restricted by dose delivered to healthy tissue and OARs (Organs At Risk). OARs are radiosensitive organs outside the target, that lie in the path of the beam[1]. Additionally, radiotherapy's efficacy is limited where oxygen levels are low (hypoxic regions)[1].

The combination of these modalities is particularly interesting as they complement each other's weaknesses. Radiotherapy is able to deliver dose to large volumes in a short period of time. This is not feasible with ultrasound. HIFU enables exposure of small regions of particular interest, for example, hypoxic regions, reducing the total radiological dose needed to control the tumour and reducing the dose to healthy tissue in turn. This works because radiotherapy becomes less effective in low oxygen regions, whereas HIFU does not and can take advantage of the poor blood supply associated with hypoxia[4] due to the reduction in the cooling effect associated with blood perfusion[5], resulting in increased heating in the area. Additionally, radiosensitivity has been found to increase with increasing temperature[6] providing further synergistic benefits from this combination. Recent studies have evaluated the effects of combining both therapies, obtaining promising results[7,8].

The combination of these therapies has led to the need for accurate quantification of the resulting biological effects[1,9,10]. Such an initiative requires the ability to characterize the systems that apply these treatments reliably. This can be done independently for each modality using phantoms, quality assurance (QA) processes and different calibration methods[1,9,10] that characterise the energy distributions under a varied range of exposure conditions, as well as assessing the performance of the equipment over time. However, the ability to perform these measurements simultaneously or sequentially, would remove the uncertainties associated with co-registration when using separate measuring devices.

Finding a material that can be manufactured reproducibly in terms of its ultrasonic, thermal and radiological properties is a prerequisite for the development of a phantom for the QA, calibration and dosimetry processes required for the combined therapy. Additionally, the closer that this material mimics ultrasound/tissue and radiation/tissue interactions, the less the need for tissue/material correction factors for dosimetry and associated uncertainties. Materials that have physical properties that resemble human tissues can be used as tissue mimicking materials (TMMs).

There is a wide range of properties that have to be matched in terms of acoustic and thermal properties. The density, attenuation, and speed of sound (SoS) determine the propagation of the pressure field. The acoustic energy is transformed into heat through absorption mechanisms. This then propagates in a manner determined by the thermal properties of the material, including the specific heat capacity, the thermal conductivity, and the thermal diffusivity. Additionally, high negative pressures can induce the formation of gas bubbles in a process called cavitation. When this occurs, it can disrupt the acoustic pressure distribution in ways that are difficult to predict[2]. The occurrence of cavitation events depends on the parameters of the sonication[11,12]: pulse repetition frequency, peak negative pressure, number of pulses, length of the pulses, the frequency spectrum of the pulses, the physical properties of the material, the amount of gas dissolved in it, its temperature and the ambient pressure, and its acoustic history, (previous exposures in the region and previous cavitation events).

Radiotherapy phantoms are either water or tissue equivalent in terms of their interactions with ionising radiation [1,13]. Due to the variety of interactions that occur and the dependence of these on the energy of the photons used and the atomic number of the materials, phantoms are created for different energy ranges[13]where different phenomena are considered[1].

An additional requirement for a radiotherapy phantom is radioresistance. The material should be able to withstand irradiation, and the associated damage, without changing its properties in a way that prevents its use as a test object.

For this project, we have explored gellan gum. Gellan gum is a polysaccharide obtained from bacteria that produces gelatine-like hydrogels at low concentrations (1-4% in wt.). It is a cheap and adaptable material that offers a good starting point for the development of TMMs for acoustic and radiologic processes due to its high water content, making its physical properties close to those of water.

The assessment of acoustic exposure has been done through the addition of a thermochromic dye. Thermochromic materials are those that change colour after exposure to heat. The associated colour change has been used to examine the power output of different systems.

The evaluation of radioresistance has been done through the comparison of selected properties pre- and post- exposure to ionising radiation. The evaluation of the applicability of the phantom to radiotherapy applications has been carried out through the comparison of simulated and experimental results which, when compared, indicate that the material matches the effective atomic number of tissues.

A phantom has been constructed from the gellan gum TMM which has been used to evaluate the power output and targeting capabilities of a therapeutic system. A MATLAB function has been developed for the evaluation of heat deposition patterns and the quantification of their size. The phantom, along with the MATLAB function, provides an accessible and cheap way of assessing the outcome of acoustic exposures.

1.1 Thesis Outline

Chapter 2 covers the theoretical background of ultrasound and radiotherapy as they are applied to the medical field, as well as the principles behind the metrology and quantification of these technologies and how they affect the biological tissues to manage their effects. This chapter also introduces the ideas that led to the use of a phantom, and specifically a thermochromic phantom.

Chapter 3 covers the manufacturing of the TMMs used throughout the thesis. The description of the manufacturing process used provides details of the standard process to produce a sample, as well as the necessary steps for adding the different doping materials that were used. This chapter also presents the techniques used to measure the different physical properties that were considered of interest for this project, as well as other measurements that were necessary.

Chapter 4 presents the results from the measurements described in chapter 3 as well as comparisons of the measured properties of the different TMMs produced with different concentrations and components, in order to assess the effects of the different components of the TMMs. These measurements were necessary to identify the effect of the different components on the acoustic properties, as well as to assess the radioresistance of the different samples by measuring the changes in the acoustic properties following exposure to ionizing radiation.

Chapter 5 presents the implementation of the TMMs, and the phantom developed in this project for the specific case of a QA application in a system designed to treat Twin-to-Twin Transfusion Syndrome (TTTS). The chapter shows the phantom design and the process of refinement that led to the final iteration of the phantom. It shows the viability of the phantom to assess acoustic power of exposures as well as showing its application in assessing the targeting accuracy. This chapter also describes the MATLAB function, which was developed for the examination of power output, as well as guidance on how it is to be used.

Chapter 6 presents the application of the thermochromic TMM to a Blood Brain Barrier (BBB) opening experiment. In this case the intent was to test whether the phantom could be used for the localization of the focus of an acoustic system, using the heat deposition patterns arising from an exposure and the resulting changes in the thermochromic TMM.

Chapter 7 provides an analysis of the results of this project and the applicability of the TMMs and the phantom, as well as a discussion of possible future work.

2 Background

2.1 Focused Ultrasound

Therapeutic ultrasound refers to a range of therapies that make use of ultrasound to perform their treatment. Ultrasound is used in medical modalities such as focused ultrasound surgery (FUS)[14] which encompasses high intensity focused ultrasound (HIFU)[2] and histotripsy[15]. Sound is a mechanical wave that travels through a physical medium[2]. This wave produces an alteration of the local pressure relative to the equilibrium state[2]. It propagates at a constant speed, known as the speed of sound (SoS), which is determined by the elastic properties of the propagation medium[3]. The product of the density and the SoS is the acoustic impedance (Z)[3]. This determines the transmission and reflection processes that occur at the boundaries of two different media[3]. Even though FUS and HIFU are often used interchangeably, I will be using HIFU to exclusively refer to thermal therapies and FUS to include HIFU and histotripsy.

2.1.1 Physical principles of therapeutic ultrasound

Ultrasound waves have an associated energy[2]. As the waves propagate, they interact with the medium, they can transfer part of their energy to it. Ultrasound can be focused in order to accumulate its effects in a region of choice, while minimizing them in the surrounding regions[2]. The size of the region is determined by the properties of the wave, the dimensions of the transducer generating the ultrasound and by the properties of the material in which it propagates[3]. In therapeutic ultrasound, these foci tend to be the size of a grain of rice.

$$D_t \propto k_t \left(\frac{R}{A}\right) \lambda$$ *Equation 2.1*

$$D_a \propto k_a D_t$$

Equation 2.2

The width of the focus D_t increases linearly with λ and the ratio of the radius of curvature of the transducer R and the aperture of the transducer A. Fry and Dunn[16] found that k_t can often be taken as 1 and k_a is always larger than 1, resulting in elliptical shapes. For typical HIFU applications the wavelength is approximately 1mm.

As acoustic waves propagate, part of their energy is deposited in the medium, producing physical changes that can result in therapeutic benefit[2]. When the acoustic wave reaches the interface between two media there is a reflection of the waves, the amplitude of which depends on the differences between the acoustic impedances[3]. The energy of the incoming wave is distributed between the transmitted and the reflected portions[3]. The greater the difference between the acoustic impedances, the more the energy will be reflected[3]. This means that, in practice, ultrasound will be obstructed by bones, which have both higher density and speed of sound than other tissues, and the lungs, which are filled with air and have lower densities and speed of sound. Reflections are characterized as follows:

$$R = \left(\frac{Z_1 - Z_1}{Z_1 + Z_2}\right)^2$$

Equation 2.3

Where R is the reflection coefficient, a measure of how much the wave is reflected relative to the incoming wave, Z_1 and Z_2 are the acoustic impedances of the two media respectively[3]. The reflection coefficient characterizes the ratio of the power of the incident and reflected waves. This formula is only applicable to planar waves during normal incidence.

As a wave propagates, energy is lost to the surrounding medium. This is called attenuation and is represented as:

$$W = W_0 \cdot e^{-\mu x}$$

Equation 2.4

where W_0 and W are the starting total power and the power after traveling the length x through a material of attenuation coefficient μ [3]. This formulation gives the attenuation coefficient in units of nepers per centimetre.

However, in the field of acoustics it is more typical to use the ratio of amplitudes rather than the ratio of powers and to use units of decibels, which use powers of 10. The power is then attenuated as:

$$W = W_0 \cdot 10^{-\frac{\mu x}{10}}$$

Equation 2.5

And for the pressure:

$$P = P_0 \cdot 10^{-\frac{\alpha x}{20}}$$

Equation 2.6

In these formulations μ and α are numerically equal and expressed in units of dB/cm.

The attenuation is further divided into two components, absorption and scatter, depending on the way the energy is transferred to the medium[3].

$$\alpha = \alpha_a + \alpha_s$$

Equation 2.7

Absorption (α_a) represents a direct conversion to heat[3,17]. Scatter (α_s) represents energy losses that do not convert directly into heat[3]. These result from inhomogeneities in the acoustic impedance of the material[2,3]. Scatter tends to represent 20 to 40% of the attenuation in soft tissues.

Attenuation is easier to measure than scatter or absorption on their own as it is the total loss of energy of the acoustic wave. There is much literature that confuses absorption and attenuation.

When ultrasound involves sufficiently high pressures, it can produce a phenomenon known as acoustic cavitation[2,3]. Cavitation is the phenomenon in which bubbles form within a fluid[2,3]. The term is used both to refer to the generation of the bubbles and to their activity within the acoustic field[2,3]. This is caused by the negative going excursion of the pressure wave that leads either to the fluid dropping below its vapour pressure, causing it to vaporize, or to dropping below the saturation pressure of the gases dissolved in the fluid, causing them to create bubbles[18]. Biological tissues, while not being fluids, can also cavitate since tissues also contain various fluids that can cavitate.

When these bubbles form, they can experience a regime in which they grow to many times their original size and collapse, this is called transient or inertial cavitation[2,3]. Alternatively, there can be sustained growth and shrinkage as their boundaries oscillate under the acoustic field[2,3]. These bubbles alter the processes of propagation and energy deposition. When they collapse, they deliver their energy locally and can produce thermal and/or mechanical damage[2,3]. These bubbles may disrupt the therapeutic processes and may either be detrimental to the medical intent, or may be used intentionally[19].

Cavitation is typically characterized by a pressure threshold[2,3]. Historically this value has been given as the negative pressure that must be reached within a material in order to produce bubble activity at a particular frequency[20]. It has been found that the threshold varies as $\frac{1}{f}$. More recent papers have shown that for a given exposure, cavitation is probabilistic in nature and that it is also dependent in the history of the material, since previous exposures can condition, or prevent, future cavitation events from occurring[11].

A pulse can be presented as a sum of idealized waves of given frequencies, each one with its own energy[3]. This is the frequency spectrum. As a wave travels there is an additional phenomenon that transfers energy from the low frequency region of the spectrum into the high frequency part [3]. This is non-linearity and is typically characterized by the non-linearity or the "B/A" parameter[3]. This parameter is derived from consideration of the pressure P as a function of the density ρ. The Taylor series for this relationship gives:

$$P = A\rho + \frac{1}{2}B\rho^2 + O(\rho^3)$$

Equation 2.8

B/A, is used as an indicator of the nonlinearity of the medium in question.

$$P = c^2\left[\rho + \frac{1}{2}\frac{B}{A}\frac{\rho^2}{\rho_0}\right] + O(\rho^3)$$

Equation 2.9

2.1.2 Biological effects of FUS

When FUS is used in a regime which relies on the deposition of heat with therapeutic intent it is called hyperthermia or HIFU, depending on the range of temperatures induced. When it is used in a regime that relies solely on the use of mechanical damage to produce tissue emulsification, it is referred to as histotripsy.

For HIFU, the biological effects are due to the temperature rise produced by the sonication. The scale of the resulting damage is linked both to the temperature rise and to its duration. When biological tissues are exposed to temperatures above 55°C for a few seconds it produces rapid protein denaturation[21,22]. This results in cell death and is referred to as ablation. Further increases in temperature lead to desiccation, and reaching 100°C will lead to vaporization of fluids and boiling of the tissues[21].

Alternatively, when tissues are maintained at temperatures of 42°C, their proteins start to degrade[23]. If this process progresses faster than the body can repair, for a long enough time, this will lead to cell death.

Clinically, a distinction is made between hyperthermia, where the maximum temperature is 45°C and ablative exposures, which start at 55°C. Additionally, in the case of ablative exposures, there is always a neighbouring region that experiences hyperthermic temperatures, as the heat from the main region diffuses out through conduction and the perfusion mechanisms of the body.

Histotripsy makes use of controlled cavitation effects in order to produce mechanical damage[19,24]. The exposure results in a liquefaction of the tissue[19,24]. The biological damage is caused by the direct breakage of the cells and once this effect has been achieved there is no benefit in prolonging the exposure. The exact damaging processes are not entirely understood[25] and histotripsy can also produce heating, not just exclusively mechanical damage[25–27]

The strength of FUS in comparison to other modalities is its ability to deliver treatment to localized parts of the patient non-invasively with little to no damage being caused to healthy tissue, causing skin burns at worst[2,14]. Other side effects can be caused when failing to account for internal reflections of the acoustic waves due to the presence of bone or gas and due to a misplacement or suboptimal placement of the focus[2]. FUS is frequently applied in prostate cancer[2,14] using transrectal devices. Cancer in organs that can be accessed through external surfaces such as the thyroid, breast, kidney, liver, pancreas, uterus and testes[2,14]are also treated. It is also used for palliative treatment of pain from bone cancer[14] and producing ablation in the brain for the treatment of essential and Parkinson's tremor[28]. These treatments result in fewer side effects than radiotherapy treatments and avoid the risks associated with open surgery[14].

2.1.3 Metrology of FUS

Acoustic fields are typically characterized in terms of their pressure (or intensity) and its spatial distribution. Properties such as the peak positive and negative pressures, temporal and spatial average intensities, the position and size of the focus along with parameters such as the frequency of the wave, the length of the pulses and the pulsing regime are also important in reporting exposures[9].

Measurements necessary for the characterization of acoustic fields are typically carried out in water[10]. This is due to the water's low attenuation, meaning that the energy losses associated with the propagation of the acoustic field can be ignored. The SoS of water is also very similar to that of tissues, meaning that many of the associated properties of the wave are also similar to those that would be measured in tissues.

Acoustic power is typically measured with a radiation force balance[9]. This is done by introducing a target in the path of the beam and measuring the energy delivered [3]. As the wave impacts the target, it exerts a force on it which is proportional to the power in the wave[3]. This force can be measured using a balance, and needs to be corrected with different mathematical factors depending on the specific configuration of the system[3]. The target may be absorbing or reflecting[29,30].

Measurements are performed across a range of energy settings in order to characterize the system's efficiency and to calibrate its output.

When working with focused transducers it is important to characterize the position and size of the focus. This characterization of the spatial distribution of the pressure field is done with a hydrophone[9]. A hydrophone is a device that, when exposed to an acoustic wave, produces an electrical signal[3]. It uses piezoelectric materials. These generate a voltage when deformed and vice versa[3]. The probe is scanned through the acoustic field to obtain the pressure distribution[3,9].

2.1.4 Dosimetry of FUS

The parameter used for characterisation of thermal therapies is thermal dose[3]. This is based on the observation that for temperatures above 43°C a one degree increase in temperature requires a halving of the exposure time to accomplish the same biological effect[3,31]. For temperatures below 43°C the time must be multiplied by four[3]. This results in an equation of the form:

$$TD_{43} = \int_{t_0}^{t_{end}} R^{43-T(t)} dt$$

Equation 2.10

R has been determined to be 0.5 for temperatures above 43°C and 0.25 for temperatures below that[3].

This formula allows comparison of exposures by converting them to an "equivalent-time" exposure at a selected temperature, usually taken to be 43°C. The unit of thermal dose is CEM43 (cumulative equivalent minutes at 43°C).

For mechanical modalities of FUS there is no standardized measure of dose. While an individual exposure can be quantified, there is no universal quantity connecting exposures. In contrast, thermal therapies can have specific targets of thermal dose, for example, thermal ablation is presumed to occur at a thermal doses of 240 CEM.

2.2 Radiotherapy

Radiotherapy refers to treatments that use ionizing radiation for medical purposes[1]. Ionizing radiation is comprised of particles that, upon interacting with matter are capable of ejecting their electrons, ionizing them. These particles are produced either through nuclear reactions, such as the decay of radioactive materials, or by the acceleration of charged particles, such as the acceleration of electrons to produce x-rays. Radiotherapy is broadly divided into external beam radiotherapy (EBRT)[32], also known as teletherapy, and brachytherapy. EBRT covers a series of techniques that make use of external sources of radiation to deliver radiation dose to the desired tissues[32]. These include photon, electron and proton beam[1] therapies. Brachytherapy makes use of sealed radioactive sources which are placed next to the targeted regions in the form of needles, seeds or patches[32]. The particles emitted depend on the source being used.

Depending on the particles being used by a specific therapy, there may be different processes that take place to deliver the radiation dose[1].

2.2.1 Physical principles of radiotherapy

Charged particles produce ionizations through collisions with the surrounding media[1]. Charged particles generate an electric field around them through which they interact with the electrons in the matter, colliding with them, transferring their kinetic energy in the process, ejecting the electrons [1]. This is described by the Bethe-Bloch formula which describes the rate at which a charged particle transfers its energy to the surrounding medium[1].

$$-\left\langle \frac{dE}{dx} \right\rangle = \frac{4\pi}{m_e c^2} \frac{nz^2}{\beta^2} \left(\frac{e^2}{4\pi\varepsilon_0} \right)^2 \left[\ln\left(\frac{2m_e c^2 \beta^2}{I(1-\beta^2)} \right) - \beta^2 \right]$$

Equation 2.11

This is energy E lost per unit length for a particle with charge z and speed v traveling through a medium of electron density n with an average excitation potential I, where m_e is the mass of an electron at rest, e is the charge of the electron, ε_0 is the electric permittivity of vacuum, c is the speed of light and β is the ratio between the speed of the particle and c.

Additionally, charged particles can also transfer their energy through bremsstrahlung[1]. Any charged particle that experiences acceleration loses some of its energy in the form of electromagnetic radiation, photons. This phenomenon is more relevant to electrons than any other charged particles, due to their low mass, and can be used to generate photon beams in linear accelerators and x-rays[1].

Photons interact with matter through three main mechanisms:

The photoelectric effect describes the process in which a photon is absorbed by the electron in an atom[1]. When the amount of energy is enough to unbind the electron from the atom, it will be ejected.

Scattering encompasses both coherent scattering (Rayleigh scattering) and incoherent scattering (Compton scattering). In both processes the photon, which is massless, transfers energy or momentum to the electron it collides with. During coherent scattering, there is no transference of energy between the photon and the medium but there is a change in the momentum of the photon, diverting it from its original path. During incoherent scattering there is a net transfer of energy between the photon and matter, the photon collides with an electron causing it to be ejected while not being absorbed by it[1]. In this process the photon will transfer part of its energy and continue existing. This process is often approximated by the Klein-Nishina formula[33], which treats the electron as being at rest and having the photon collide and transfer its momentum to the electron, ejecting it from the atom in the process. This approximation is better at higher energies, where the kinetic and binding energies of the electron become significantly smaller than the energy transferred during the collision.

Pair production is the process in which the photon interacts with the electric field of the nucleus to create an electron-positron pair[1]. This can only occur for photons with an energy sufficiently large to produce the masses of the electron-positron pair (1.02 MeV) and the remaining energy, if any, will be distributed equally between the resulting pair as kinetic energy[1].

Additionally there is the less frequent triplet production in which the photon interacts with the electric field of the electron to produce an electron-positron pair and eject the electron from the atom[1]. This results in three charged particles (thus triplet) and is only possible at energies above 2.04 MeV and is a lot less likely than other processes.

These three processes have different relative probabilities depending on the atomic number of the nuclei with which the photon interacts and the photon's energy[1]. Typical radiotherapy energies cover from 1 to 10 MeV energies[34] However, higher energy treatments are being phased out by more complex and accurate treatments such as IMRT, which has brought the typical threshold to 6MeV[34]. Imaging modalities, on the other hand, will typically go down to 40keV[35], with the exception of mammographies, were they go to 20keV[35]. Considering the typical energies used and the constituent elements of the body (96% of the body mass is accounted for by hydrogen, oxygen, nitrogen and carbon[36]), most radiotherapy and radioimaging processes are driven by Compton scatter.

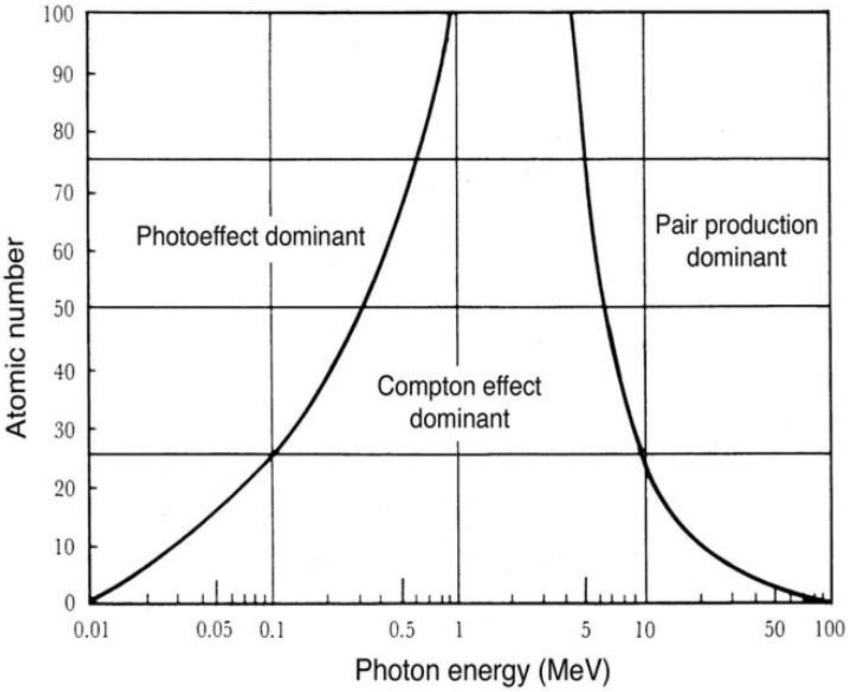

Figure 2-1. Relative dominance of the corresponding interaction depending on the atomic number of the irradiated material and the energy of the irradiation[1]. The curve on the left shows the region were the cross section for the photoelectric effect and the Compton effect are equal. The curve on the right shows the region where the cross section for the Compton effect and pair production are equal.

While Pair production and Photoelectric absorption eliminate the photon after the interaction, Compton scatter reduces the energy of the photon[1]. This means that as a beam of photons progresses through a medium there is a change in the energy spectrum of the beam. Lower energy photons are more likely to be absorbed while higher energy photons tend to propagate, losing their energy until they are absorbed[1].

The process by which photons cause ionization is not straightforward. Photons deliver part of their energy to the electrons which then in turn travel, colliding with other electrons in the medium and distributing the energy[1]. This leads to a shift between the energy distributed in a medium and the flow of photons by the average pathlength of the electrons generated by a beam[1].

For a given monochromatic (only one energy) narrow beam travelling through matter, the intensity of the beam evolves as[1]:

$$I = I_0 \cdot e^{-\mu x}$$

Equation 2.12

Where I_0 is the initial intensity of the beam and μ is related to the probability of interaction per unit path length. The coefficient μ is the linear attenuation coefficient. It will be a function of the energy of the beam and the properties of the material. The coefficient μ is often given in units of cm^{-1} but it can also be found as the mass attenuation coefficient which is obtained by dividing it by the medium's density[1]. This attenuation coefficient μ is named in the same way as the acoustic attenuation coefficient, as they characterize similar behaviour, but they represent entirely different phenomena. Since these fields of physics do not often intersect, these naming conventions have not needed further clarification.

This is a simplistic approach that is useful for some calculations, while the best approach is to use Monte-Carlo simulations in which each photon and its interactions are calculated through their relative probabilities and the generation of random numbers[1]. When a sufficiently large number of particles are simulated, these methods can accurately predict the behaviour of the beams. Other systems use pre-calculated models derived from Monte-Carlo simulations for the path of a narrow beam and combine these to make predictions[37].

2.2.2 Biological effects of radiotherapy

Radiotherapy damages living tissue through the ionization it causes[1]. A cell can die directly as a result of the irradiation, or the radiation can cause damage that only leads to its death when it attempts to perform its function, divide or even repair the damage[1]. Though unlikely, a photon can directly impact the DNA of the cell, causing it to be damaged in the process[1]. However, the more likely event is that the ionization will create free radicals which will then cause the damage to the different parts of the cell[1].

The ability to generate these radicals is influenced by the medium itself[1]. Therefore, the oxygenation of an area has an effect on the efficacy of radiation therapy. This phenomenon is of particular interest in larger tumours, as their chaotic growth tends to lead to hypoxia in their centres, making these regions resistant to radiation killing[1].

Different organs have different susceptibilities to irradiation and the consequences of damaging them vary[1]. The susceptibility of cells also depends on the part of the reproductive cycle in which they find themselves. For this reason, radiation doses tend to be delivered in fractions that are repeated over several days[1].

Photon beams travel through matter, delivering energy all along their paths. Charged particle beams have a maximum range to which they travel and deliver most of their energy[38]. In either case, there is always a radiation dose delivered to healthy tissues, carrying a related risk.

2.2.3 Metrology in radiotherapy

Radiation beams are typically characterized by their dimensions, and their energy spectrum, the particles that form them or measures of their penetrative power. Photon beams produced through bremsstrahlung are referred to in terms of their maximum energy, even though there is a wide range of energy values within the field. Other relevant information is the half-value layer[1] (HVL), which is the thickness of a given material that reduces the intensity by half.

A radiotherapy machine will be characterized in terms of its output and the geometry of the beam produced[1]. The output can be characterized using many different terms, such as the fluence of energy or photons and the amount of energy transferred to the air by the beam at given points[1]. The beam will also be characterized in terms of the energy spectrum of its photons, whether it is monoenergetic or not[1]. Other parameters describe the flatness of the beam[1], which characterizes the intensity distribution of the beam at specific planes perpendicular to the direction of propagation, and its symmetry[1]. The penetrative capabilities can be measured in terms of the HVL or the percentage depth dose (PDD) depending on the energy of the beam[1]. All these measures tend to involve measurements in phantoms and in different relative positions in order to describe the spatial distribution of the particles and energies resulting from the beam adequately.

Ionization chambers are amongst the most used devices for the characterization of radiotherapy beams[1]. These are cavities containing an electrode, that measure the ionization produced by the beam within the chamber[1]. Their design varies in shape and size depending on the specific use[1].

Other measurement devices, such as gafchromic film[1], rely on chemical processes that are mediated or initiated by radiation, resulting in some physical change that can be measured.

Starting in 1987 the IAEA recommended that dosimetry measurements be performed in water[39]. This was reinforced in 1997[40] and remains the standard in their 2005 report[41]. Water has been chosen as the reference for these measurements due to its availability, making measurement conditions reproducible across laboratories in the world, and its close resemblance to soft tissues. Additionally, it was found that ionization chambers designed for operating in water performed more consistently[41] than chambers designed for measurements in air. Measurements can also be made in water-equivalent phantoms or plastics. These are designed to replicate the interactions of water with radiation by mimicking its mass density, number of electrons per gram and effective atomic number[1]. Water mimics are recommended for circumstances in which a water tank would be impractical[1].

Beams are shaped using different collimators[1]. Dosimetry measurements are often performed with square sections in order to provide consistent and reproducible reference conditions in the evaluation of the beams. However, rectangular, circular, and irregular fields are also of interest. Irregular fields, which are produced using multileaf collimators (MLCs), are much more relevant for the targeting of specific organs that for the overall evaluation of radiation output of the machine[1]. Any collimators must be assessed in terms of their mobility and the sharpness of the regions produced after collimation.

2.2.4 Dosimetry of radiotherapy

Radiation dosimetry is centred around the characterization of two different entities. The beam, which is described in terms of output, and the energy of the particles constituting the beam, and its ability to deposit energy in a given medium.

Beams can be characterized in terms of the photon fluence or the energy fluence. These characterize the flow of the corresponding magnitudes (number of photons and energy) through a given area. These two magnitudes can also be converted to the photon fluence rate and the energy fluence rate by dividing the fluences by their duration to obtain the corresponding amounts per unit time[1].

The parameter used to characterize therapies in radiotherapy is the gray[1]. A gray measures the amount of energy delivered to a given mass and has units of Joules per kilogram.

The Kerma, kinetic energy released per unit mass, is a measure of the average energy transferred from indirectly ionizing radiation, such as photons, to directly ionizing radiation per unit mass of the medium where the transfer occurs[1]. This is quoted in grays.

The Cema, converter energy per unit mass, represents the energy lost by charged particles per unit mass of medium[1]. This is, again, quoted in grays.

Absorbed dose describes the total energy deposited by ionizing radiation per unit mass of medium[1]. For the case of indirectly ionizing radiation this will be a two-step process of transferring the energy and producing ionizations (this energy will be the kerma), and then the resulting particles transferring the energy to the medium[1]. Because the electrons travel in the medium as they deposit their energy there is a shift between the kerma and absorbed dose distributions[1].

It is important to note that the energy delivered per unit mass is often in a range so small that it barely increases the temperature of its target[1]. This highlights the fact that the processes involved in ionising radiation therapy are dramatically different from those in HIFU.

Treatment planning is done using structural information of the patient, often a CT-scan, and simulating the dose from different beam configurations trying to optimize the radiation delivered to the target while minimizing the dose to healthy and/or sensitive tissues[1].

There are other ways of characterizing a treatment, such as the biologically effective dose. This attempts to compare two different treatments[42]. The BED uses data about the recovery rates of different tissues to make a better prediction of the outcome of a given treatment[1,42].

In the characterization of radiotherapy beams, profiles are often produced to identify the spatial volume of distribution of dose[1]. These profiles are influenced by a variety of factors both physical, such as the energy of the beam itself and the amount of scatter occurring in the acquisition, and geometrical, such as the divergence of the beam, and its collimation[1].

Chief among these characterizations are percentage depth dose profiles (PDDs)[1], which show the change of dose along the central axis of the beam and highlight features such as the build-up region, and transversal profiles, which can be used to evaluate the beam flatness and the dose to the umbral and penumbral regions of the beam[1]. Examples of these can be seen in Figure 2-2. These are fundamental tools that are used to evaluate the dose delivery and the planning of therapies[1].

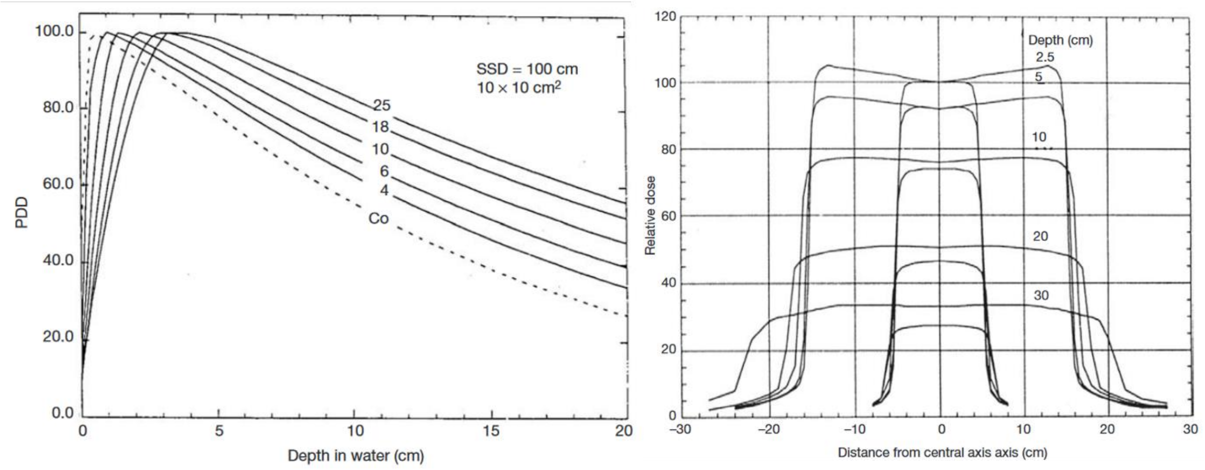

Figure 2-2: Left, PDDs for various sources of different energies (MV) with a fixed field size at a specific source to skin distance (SSD)[1]. Right, beam profiles for two different field sizes (10x10 cm and 30x30 cm) at different depths in water[1].

Typical radiotherapy doses will deliver up to 80 Gy per treatment[43], this being divided into fraction. Fractionation has been known as a enhancer of the therapeutic benefits of therapies[1] and the standard faction is 2Gy per fraction[43,44]. Hypofractionation is a more recent development[43] also presents benefits in certain applications[43,44]. Hypofractionated therapies can reach as much as 20 Gy per fraction[44].

2.3 Combined FUS and radiotherapy

2.3.1 Rationale for using two combined treatments

Radiotherapy and FUS have very complementary modes of delivery. Radiotherapy is capable of covering large volumes with ease due to their beam widths, typically around 10x10 cm^2, and their ability to penetrate human tissues. They are capable of delivering radiation through the entire thickness of the patient. Therapy ultrasound beams, on the other hand, have a small focal size, they have a limited range, typically reaching depths of around 15 cm.

While FUS has little to no side effects, skin burns in some cases, it can be obstructed by bones and the lungs and have a limited reach. Treatment of targets larger than the focus requires multiple applications which can become time consuming and the overlap between exposures can lead to skin burns. Radiotherapy has a limitless potential to reach any part of the body and can be delivered much faster, but it delivers a dose to healthy tissue, thus presenting the low, but finite long-term risk of inducing secondary cancers, and if there may be additional side effects in any radiosensitive organs.

Additionally, as was mentioned above, hypoxic regions are radioresistant, whereas FUS may be delivered more efficiently in these volumes as they have poor blood supply.

All these characteristics mean that it might be advantageous to target specific parts of tumours, such a hypoxic regions or areas that need a higher radiological dose, in order to reduce the overall dose delivered to the rest of the body without compromising the length of a treatment entirely. Moreover, it has been suggested that the heating produced by ultrasound therapy could have a vasodilative effect, promoting blood flow to the hypoxic regions and increasing their radiosensitivity[45].

2.3.2 Preliminary results in literature

Research has found that hyperthermia has radiosensitizing effects [45–53]. Hyperthermia refers to temperature increases above the normal body temperature of 37°C typically reaching from 39 to 45°C.

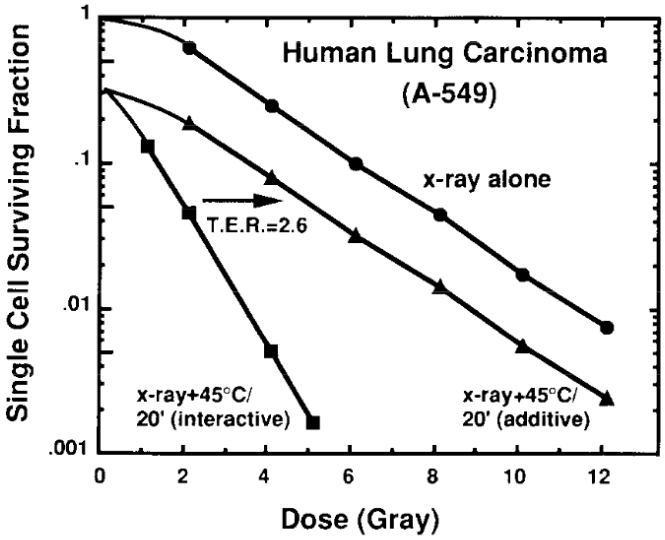

Figure 2-3. Survival curves with increasing dose comparing the radiotherapy alone (●) with the combined treatment (▲) and the expected calculated results if both treatments were merely additive (■) [48]. TER was calculated as the ratio of the D_0 of the two curves, where D_0 is the parameter corresponding to fitting the survival curve to a function of the type $S(D) = e^{-D/D_0}$.

In vitro studies in rodent and human cells have shown that the effects of the combination of x-ray doses and hyperthermia treatments goes beyond an additive effect (Figure 2-3). Survival curves show the fraction of viable cells present at a certain point in time compared to the starting population.

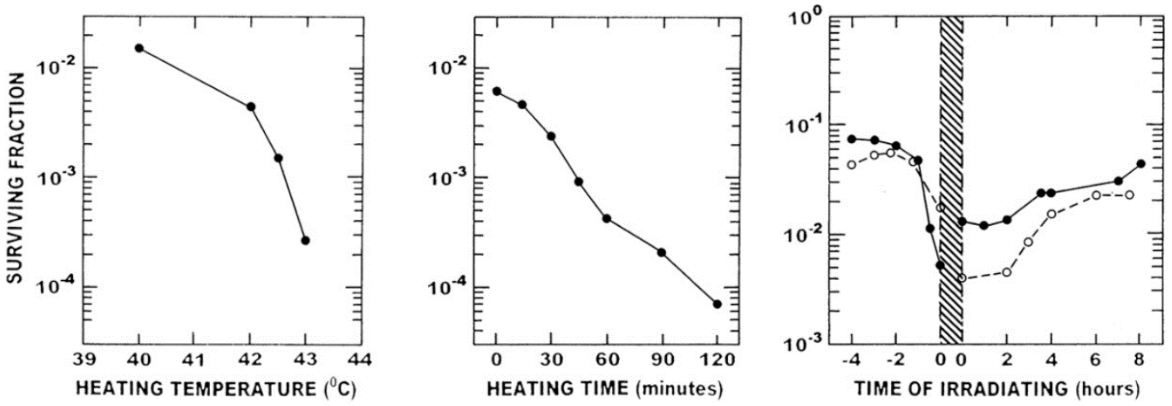

Figure 2-4. Left: Surviving fraction for 12 Gy doses is shown to reduce with increasing temperature for a fixed time (2 hours). Centre: Surviving fraction for 12 Gy doses is shown to reduce with increasing time at a fixed temperature (43°C). Right: The effect of the time between between iradiation (6Gy) and heating (43°C; 60 min). The symbols ∘ and • correspond to different cell lines and the data seems to coincidentally show a discontinuity between them at the offset of 0 where the shaded area represents heating[52]*.*

Figure 2-4 shows that the enhancing effects of hyperthermia increase with increasing temperature and heating times[52]. These enhancing effects seem to reduce significantly 4 hour after heating,[52] and the benefits appear to be dependent on the order of application of the therapies[51,52].

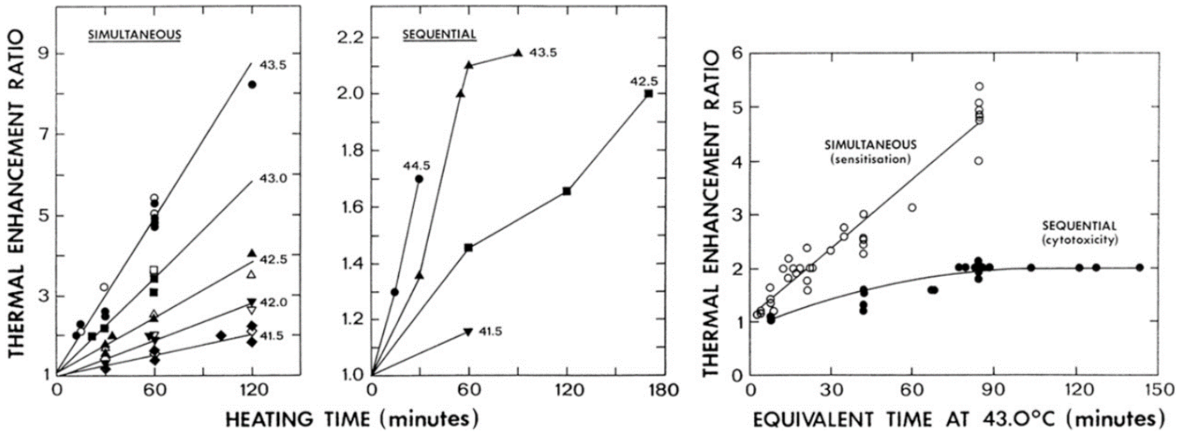

Figure 2-5. Thermal enhancement ratios for increasing temperatures and exposure times for simultaneous and sequential (Left and centre) exposures. Right: comparison of sequential and simultaneous exposures. Thermal enhancement ratios were calculated as the dose ratio to produce the same biological effect[52]*.*

The comparison of sequential and simultaneous deliveries (Figure 2-5) shows that simultaneous treatments offer the best enhancement effects[52]. However, this is still limited by the availability of the equipment able to perform both treatments.

Research into the mechanisms by which hyperthermia enhances the effect of radiation has found variety of mechanisms[49,54] and is still in progress.

Recent interest in the application of such effects has developed into a large scale project for the development of combined hyperthermia and radiotherapy applications[55].

The need for optimization, and interest in the application of this combined therapy makes the development of a framework for QA and metrology a field ripe for study.

2.3.3 Current limitations of phantoms for combined radiotherapy and HIFU

The main limiting factor in the creation of a phantom for these combined therapies is the use of a system that allows the simultaneous measurement of both radiological and thermal dose. Ionisation chambers would prevent the propagation of ultrasound through them since they are air filled with metallic walls. Gafchromic film would similarly prevent the propagation of ultrasound due to the acoustic mismatch with water which would lead to reflections. In addition, instructions warn against getting them wet or above temperatures of 50°C.

While there has been an attempt to use PRESAGE, a phantom commonly used in radiotherapy, for the metrology of ultrasound[56]. this would not allow independent identification of the radiation and the thermal doses and would only allow sequential measurement of these. It would be more appropriate to perform sequential measurements with devices optimized for each therapeutic modality. The use of leucodyes offers an avenue of work in which identifying dyes exclusively responsive to thermal effects or radiation effects could be used, however, the tests with PRESAGE raise questions about this possibility and it would be crucial to ensure that any dyes offer a distinguishable and separable change in colour.

While this is a limitation that prevents the possibility of measuring both doses, a system that allows sequential measurements would be a great improvement and can still feasibly be designed. This would remove problems of co-registration that two separate measuring methods would produce. A phantom material suitable for both radiotherapy and ultrasound applications is a first step in this direction.

Phantoms for the visualization of lesions in HIFU exposures have seen some applications[57–60]. Optically transparent phantoms provide very valuable information about the process of the formation of the lesion, and the opportunity of real time imaging. These systems will, by nature of the lesions formed, provide an outline of the region that has reached the transition temperature, as the lesion grows, and its opacity blocks the view of the inner regions. These systems offer the possibility of 3D reconstruction via the use of optical tomography. However, such a setup will be costly and require a very precise setup and alignment along with expensive equipment in order to provide quantitative data of the size of the lesion.

Other attempts at developing QA phantoms such as Kevin Martin and Richard Fernandez[61] have required complex setups to examine the heat patterns that make the setup less adaptable to other transducers and while the comparisons of the thermal images and the intensity plots is remarkable, it lack any indication of the scale of the thermal images.

The work of Qureshi[62] et al show the application of a material provided by precision acoustics for QA. While the material itself provides a remarkable heat pattern that offers appreciable colour gradient that could be applied to a great thermal resolution, the publication is unremarkable in the development of a code that produces a simulation of the heat patterns associated with the power input when such work could be simply replaced with an experimental calibration by exposing the Precision Acoustic's material and measuring the size of the lesions.

Furthermore, both Martin and Fernandez's work[61] and Qureshi's[62] rely in the use of heavily attenuating materials ($27\,dB/(cm \cdot MHz)$ and $28.8 \pm 2.6\,dB/(cm \cdot MHz)$) which would prevent any beam from propagating inside the materials, limiting ultrasound imaging beyond that point and severely altering the distribution of the beam within them. A measure of the penetration of the beam can be approximated from Equation 2.4 as 3 to 5 times the inverse of the attenuation. A distance of 3 times the inverse of μ would represent 95% of the beam being attenuated and 5 times represents 99% of the beam. Considering the attenuation of these phantoms these values would be approximately 1 and 2 mm for the 3 and 5 times respectively.

Similar to the project at hand, the work from Eranki et al[58] uses the Hallcrest MB-60 dye to create a thermochromic TMM which is then sandwiched between two acrylamide samples and exposed to ultrasound. While the use of a thermochromic phantom is an improvement on the use of transparent phantoms, as it can provide information on heated regions across a more continuous spectrum, rather than a binary result regarding a threshold of heating, this design, however, requires the thermochromic sample to be cut to inspect the lesions, in which adds an unnecessary source of error in the examining of the lesions. Additionally, polyacrylamide gels can be dangerous, as the monomer used in its preparation, acrylamide, is neurotoxic[63].

Our project improves on these designs by using a safer option that retains the use of thermochromic dyes, as opposed to BSA, and uses a modular design that removes the need for cutting the samples. The design of the phantom also enables the examination of the samples through simple and accessible systems, such as a smartphone camera, and the project also included the development of code for the analysis of the data. The phantom also includes design elements to evaluate the targeting accuracy of US guided systems.

2.4 Phantoms and TMMs

Tissue mimicking materials (TMMs) are materials that are designed to replicate some of the physical properties of human tissues. The specific properties replicated are those that are relevant to the individual process that is being studied or analysed. Realistic phantoms can attempt to replicate complex physiological processes, such as the addition of perfusion in thermal phantoms[64]. TMMs are typically used in the manufacture of phantoms. Phantoms are surrogates for human tissues and are used for metrological purposes in medical equipment. They can range from a single sample of a given TMM or a combination of TMMs, can have simple geometries (such as boxes or cylinders) or can replicate a specific body part. They can be used for quality assurance or for dosimetry.

2.4.1 Phantoms provide a way of assessing the performance of medical equipment and ensuring that the clinical outcome of a given procedure, diagnostic or therapeutic, will meet appropriate standards and will not harm the patient[9]. When applying these ideas to QA, the need to replicate the human body becomes lightened, as opposed to a dosimetry application. A QA process needs to be repeatable and reliable while providing as much information about the equipment tested. Any discrepancies between the test material and human tissues are irrelevant as long as they do not limit the analysis. Hydrogels as TMMs for FUS

Hydrogels are materials formed by a matrix of polymer chains encasing water, and that form gelatine like solids[65]. Therefore, many of their properties, such as specific heat capacity, thermal conductivity and diffusivity, and their speed of sound and density, are similar to those of water. The acoustic absorption and scattering coefficient are always greater than those in water. Hydrogels such as polyvinyl alcohol (PVA), polyacrylamide (PAA), agar and gellan gum have been used widely as TMMs[66]. The main difference between these TMMs and tissues lies in the values for the absorption and scattering coefficients, which tend to be low in unadulterated gels. However, there are many doping agents that can be used to tune these values.

It was decided to use gellan gum in the work described in this thesis since the gelling process is significantly easier than that for PVA[67] and PAA[59], the low concentration needed for gelation, and the relative increased reported attenuation values compared to agar[66,68].

2.4.2 Thermochromic materials

Thermochromic materials are those that change colour in response to heat. This change can be reversible, or permanent, depending on the colour-change process[69–71]. These materials often rely on some chemical reaction between two components to achieve the colour change[72]. Additionally, some compounds may change their physical structure that changes their colour when exposed to certain temperatures, such as the crystallization of collagen or bovine serum albumin (BSA)[60,71,73] at high temperatures.

While a reversible colour change would allow for a reusable phantom, thermal information must be extracted before the pattern starts to revert. Additionally, these types of dyes tend to exhibit some form of hysteresis, where the colour is not directly related to the current temperature of the object but its history[72].

2.4.3 Hydrogels as TMMs for ionizing radiation

Hydrogels have also been used in radiotherapy[74,75], although they are much less common. Considering the energy range and the elements present in both human tissues and hydrogels, the dominating effect is Compton scattering. Fortunately, the probability of Compton scattering is proportional to electron density which, for most elements is proportional to the density. Additionally, the Bethe-Bloch formula (Equation 2.11), which describes the interaction of charged particles with a given medium, is also directly proportional to the electron density. This means that a material with a density similar to water will have a similar attenuating power for many radiotherapeutic modalities.

The first gels relied on the use of nuclear magnetic resonance to measure ionization caused by the exposure by measuring the conversion of ferrous (Fe^{2+}) to ferric (Fe^{3+}) ions and extracting the dose[74,76,77]. Other gels rely on the chemical effects that occur as a consequence of irradiation to measure the dose[75].

Radiation has also been used to cause the polymerization needed for some gels, or to modify their mechanical properties by increasing polymerization through the gel[67,78]. It is thus important to assess the usability of a gel in certain dose ranges. It is important to note that since there is a lack of any biological processes within the gel, the chemical effects of radiation should occur within microseconds, meaning that any examination of these effects does not require taking fractionation or any other parameters of the exposure beyond the total dose into consideration.

2.5 Physical properties for a combined phantom

The usability of a TMM hinges on the repeatability of the measurements carried out. This can be through a reproducible but perishable phantom that can easily be remade, or through a long-lasting material that does not degrade with use.

The exact values of the properties do not necessarily have to match human tissues, since the results of a given measurement can be adjusted for the differences, but it can still be advantageous. The physical properties of a material can limit the transmission of ultrasound into it and given that our medical devices are designed to work with human tissues, an ultrasound phantom will need to be similar to those tissues in some respects.

For the propagation of ultrasound, the main properties to be considered are the density, speed of sound and the overall attenuation. The ratio between absorption and scatter will determine the echogenicity of the material and the rate of heating of the material. The higher the scatter to absorption ratio, the more echogenic the material will be but the less it will heat up given a particular exposure.

The B/A parameter will affect the propagation of the US waves; however, this effect is much smaller than other considerations, particularly when operating at low powers.

This project concentrated on the evaluation of the attenuation, speed of sound and density. Thermal properties evaluated were the volumetric heat capacity, thermal conductivity, thermal diffusivity, and melting point. CT numbers were also measured to evaluate the radiological absorption of dose.

3 Materials and methods

3.1 Manufacture of the TMMs

Gellan gum is a polysaccharide obtained from bacteria (*Sphyngomonas elodea*) grown in media containing glucose[79]. When dissolved in water and heated up it creates a hydrogel very similar to agar[80].

Gellan gum (PhytagelTM, Sigma-Aldrich) was used at concentrations of 1, 2 and 4% by weight. Silicon oxide (~99% 0.5-10µm, Honeywell FlukaTM, Honeywell) was added as a scattering agent. A thermochromic dye (MB60-NH, LCR Hallcrest) was added where appropriate in order to generate thermochromic samples. A series of samples can thus be produced depending on the addition and relative fractions of the different components.

The manufacturing process starts by pouring degassed water into a beaker. The beaker, containing a magnetic stirrer and a thermocouple to monitor temperature, is placed on a hot plate. Manual stirring would be feasible but is not advised, as it requires the system to be left open, which will lead to the loss of water through evaporation. If silicon oxide (SiO) is to be added, this is done at this point. Stirring SiO in water ensures that any lumps are dissolved, thus preventing inhomogeneities in the sample. While the presence of gellan gum does not affect the solubility of SiO, it raises the viscosity of water, thus preventing the dissolution of SiO lumps. The mixture should be stirred for a few seconds until it becomes homogeneous. At this point, gellan gum is added to the mixture. The beaker should then be covered with cling film to reduce loss of water through evaporation. The mixture is then heated to 95°C. The mixture should remain at 95°C until the mixture homogenizes and no lumps or clots can be seen (10-30 minutes). The mixture is then allowed to cool down.

The gel can be cast into moulds at any temperature, but it is preferable to do so at temperatures of 60 to 70°C, thus making it safer to handle. Additionally, any surface of the gel that is in contact with air when it is setting dries faster that the rest of the gel, and as it cools down it contracts. This can result in surface deformation. Lower pouring temperatures reduce this effect and should be considered, depending on the shape of the mould and the relevance of the area affected. Casting the gel at higher temperatures, on the other hand, results in a less viscous mixture, and better filling of narrow crevices and small moulds, although the design of the mould must accommodate gel shrinkage. This may require a pilot attempt to ensure that the resulting gel is adequately shaped, and a redesign of the mould.

If thermochromic dye is to be added, the mixture should be allowed to cool to 60°C, while the thermochromic dye is separately heated to 50°C. At this point the thermochromic dye can be added to the mixture. It is critical to maintain the temperature of the mixture above 50°C, to prevent the gel from solidifying, and below 60°C, to prevent the dye undergoing permanent change.

3.1.1 Zinc acetate as a doping agent

Zinc acetate (ZnOAc) has been reported as a possible doping agent for increasing the absorption of gellan gum samples. Its addition, however, is not a trivial process since the presence of cationic salts can trigger the gelation process[81]. The addition of ZnOAc solution to the molten gel leads to immediate solidification of the gel, preventing any possible subsequent use. Gelation will also be triggered by contact between these liquids, creating irregular surfaces.

Following Troia et al[82], it is advisable to make the gel and then submerge it in a water solution with excess zinc acetate. The gel itself is a polysaccharide matrix which traps water. This water is able to exchange with its environment, and solutes can be transported into the gel[65,83]. The gel can thus exchange water with its environment and zinc acetate will diffuse into the gel, reaching equilibrium.

In order to prepare the samples and allow for the salt to diffuse into the gel, samples were allowed to sit in the preparing solution overnight.

It is important to consider that the concentration of the final sample will be that of the solute dissolved in the total amount of water.

$$[Salt] = \frac{Salt_{mol}}{Solution_V + Sample_V}$$

Equation 3.1

Where $Salt_{mol}$ represents the mols of salt added to the solution, $Solution_V$ represents the volume of water of the solution and $Sample_V$ represents the volume of water in the sample. This concentration is the molarity M (mol/L), and the magnitudes should be adjusted to the desired units. $Sample_V$ depends on the mass of the sample as well as the concentration of gellan gum and other doping agents added to the sample.

The water contribution from the uninfused gel should be taken into account when preparing a sample but can be circumvented by using a significantly larger volume of solution as seen by taking the limit of Equation 3.1:

$$[Salt] = \frac{Salt_{mol}}{Solution_V\left(1 + \frac{Sample_V}{Solution_V}\right)}$$

Equation 3.2

$$\lim_{Solution_V \gg Sample_V}\left[\frac{Salt_{mol}}{Solution_V\left(1 + \frac{Sample_V}{Solution_V}\right)}\right] = \frac{Salt_{mol}}{Solution_V}$$

Equation 3.3

It should also be noted that our source ZnOAc was zinc acetate dihydrate, which is not pure zinc acetate, but rather zinc acetate molecules bound to water molecules. The addition of such a salt also involves the addition of water (approximately 20% of the weight of the salt), which is taken into consideration when calculating concentrations.

The addition of zinc acetate to increase the absorption of the sample, raises the question of the possibility of the interaction between the zinc acetate and the already gelled sample. To put it mathematically, the attenuation of a gellan gum sample infused with ZnOAc would be:

$$\mathrm{A}(GG, ZnOAc) = \alpha(GG) + \alpha(ZnOAc) + \alpha(GG, ZnOAc)$$

Equation 3.4

Where $\mathrm{A}(GG, ZnOAc)$ represents the attenuation of the sample, $\alpha(GG)$ and $\alpha(ZnOAc)$ represent the contributions to attenuation from the gellan gum and the zinc acetate independently and $\alpha(GG, ZnOAc)$ represents the contribution from the interactions between the gellan gum matrix and the zinc acetate solution. This last factor may represent the changes to the underlaying matrix structure, changing the attenuation, or limits to the mobility of the zinc acetate molecules within the polysaccharide matrix, affecting their contribution to attenuation. It is impossible to say *a* *priori* which of these factors is more dominant, or even if the combined term exists, since as far as we know, zinc acetate causes the gelation of gellan gum, but once the material is already gelled, it is not known if there are any further effects. Additionally, since the attenuation of salts is accounted for as dissociation and recombination processes occurring in the solution that result in a direct transformation into heat, these processes may be unhindered by the limited mobility of the solution.

In order to examine this question, the acoustic properties of samples with different concentrations of gellan gum and zinc acetate were measured and compared.

3.2 Measurement of acoustic properties

3.2.1 Ultrasound measurements

Characterization of acoustic attenuation and speed of sound was carried out using an insertion method, also known as FAIS (Finite Amplitude Insertion Substitution).

The in-house system (Figure 3-1) uses two weakly focused transducers separated by a distance of approximately 20 cm, where one acts as a "transmit/receiver (T/R)" and the other acts as a receiver. The transducers are a nominally identical (matched) pair of broadband transducers (Imasonic A101 & A102, Imasonic SAS, France). They have the same physical dimensions (Active: dimension Ø20 mm, Focal distance in water: 100 mm ± 10 mm) and acoustic properties (Centre frequency: 2.5 MHz ±10%, Bandwidth >70% at -6 dB in T/R mode) and are confocally aligned during measurements. The signals are digitized using a picoscope (PicoScope 5000, Pico Technology). The system also includes a gantry on which the transducers are mounted, along with a series of incremental magnetic encoders (LM13, RLS, Slovenia) atop of which sample holders can be attached. The sample holder can then be moved in and out of position for the various acquisitions performed during the measurements and the sample position is controlled with submillimetric precision. This degree of control allows scans across various points of the sample to be performed, thus mapping its acoustic properties in a range of different positions.

The positioning of the sample, emission and recording of the acoustic pulses, the recording of the temperature and the mathematical analysis of the data are performed using a purpose written MATLAB function.

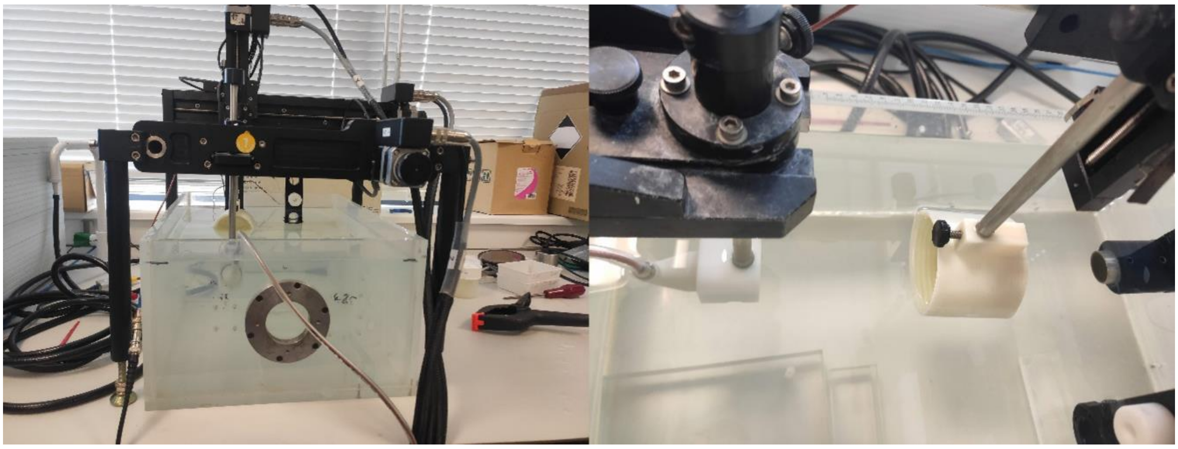

Figure 3-1:Tissue characterization system. Left, the gantry atop a water tank. Right, close up of the sample holder between the transducers.

As shown in Figure 3-2, an initial measurement in water is done by sending an acoustic pulse to provide a reference measurement. This records the amplitude of the pulse after freely propagating through water, which, it is assumed, results in no loss of energy in the acoustic pulse.

A sample is then inserted in the path of the beam. A new pulse is emitted and a transmission measurement performed. This transmission measurement records the amplitude of the pulse after propagation through the sample. The difference in amplitude is then due to the presence of the sample and is denominated the "insertion loss". The transmit transducer sends a signal and records the echoes returning from the sample. The two largest peaks represent the reflections from the front and rear surfaces of the sample which can then be used to derive its thickness. This process is represented in Figure 3-3.

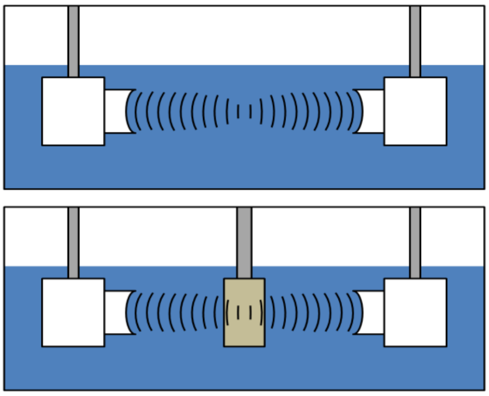

Figure 3-2.Schematic of the FAIS method. Top, the reference measurement. Bottom, the transmission measurement.

The insertion loss reflects the addition of several attenuating effects such as the attenuation, scatter, and reflection losses.

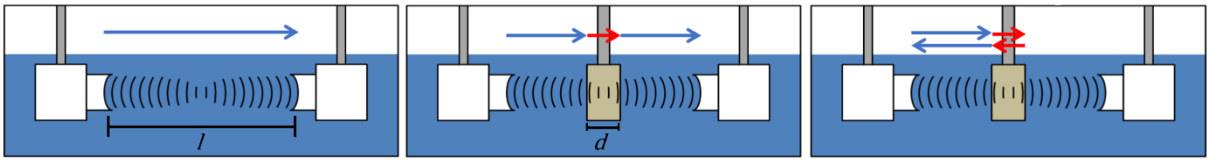

Figure 3-3: Diagram of the signal arrival times. Blue represents the wave traveling at the SoS of water, red represents traveling at the SoS of the sample. Left, the reference measurement. Centre, the transmission measurement. Right, the echo measurements.

The arrival time of the reference measurement pulse t_{ref} corresponds to the time it takes the pulse to cover the distance between the transducers l at the speed of sound in water c_W:

$$t_{ref} = \frac{l}{c_w}$$

Equation 3.5

The arrival time of the transmission measurement t_{trans} corresponds to the time it takes the pulse to cover the distance l minus the thickness d at the speed of sound in water c_W plus the time it took to cover the thickness d at the speed of sound in the sample c_s:

$$t_{trans} = \frac{l-d}{c_w} + \frac{d}{c_s}$$

Equation 3.6

The echo traces show the reflections produced when the pulse crosses the interface of two materials with different acoustic impedances. In this system, the pulse propagates through water, interacts with the water-sample interface at the front of the sample with part of the pulse being reflected back towards the transducer, simultaneously, part of the pulse continues to propagate through the sample until it encounters the sample-water interface, producing a second reflection which propagates back to the transducer. The first reflection will be recorded as a pulse at the time t_1, the second reflection will be recorded as a pulse at time t_2. As such, t_1 represents the time it takes the pulse to reach the sample and back to the transducer, while traveling at the speed of sound in water, and t_2 will be delayed by the time the pulse takes to travel through the sample at its own speed twice, as it travels from the first interface to the second and back.

$$t_1 = \frac{2l}{c_w}$$

Equation 3.7

$$t_2 = \frac{2l}{c_w} + \frac{2d}{c_s}$$

Equation 3.8

$$t_2 - t_1 = \frac{2d}{c_s}$$

Equation 3.9

From the difference in arrival time of the transmission and reference pulses we obtain:

$$t_{trans} - t_{ref} = \frac{l-d}{c_w} + \frac{d}{c_s} - \frac{l}{c_w} = \frac{d}{c_s} - \frac{d}{c_w}$$

Equation 3.10

Subtracting half the difference between the echo times we obtain:

$$t_{trans} - t_{ref} - \frac{t_2 - t_1}{2} = \frac{d}{c_s} - \frac{d}{c_w} - \frac{1}{2}\frac{2d}{c_s} = -\frac{d}{c_w}$$

Equation 3.11

Given that the speed of sound in water at a specific temperature is a known quantity we can obtain the thickness and thus obtain the speed of sound in the sample of interest.

The transmitted and reference signals are then Fourier transformed in order to obtain the frequency spectra of both signals. The ratio of the Fourier transformed transmitted signal to the Fourier transformed reference signal gives a measure of the insertion loss that the pulse experienced at any given frequency. This ratio is then divided by the thickness to obtain the attenuation.

Additionally, the system records a reference at the start of the scanning of the sample and the end of the scan. If there is a temperature difference larger than 0.5°C between the temperature of the tank at the moment the references where measured, the system will calculate the attenuation of each poin with respect to both of the references and provide a result that is the linear combination of both attenuation results weighed by their proximity, in time, to the corresponding reference signal. This is an aproximation that assumes that the temperature increase would have ocurred linearly during the measurements. As of this project a combination of a cooling and heating system were used which resulted in the temperature never drifting appart further than 0.1°C and as such, this function was never used. Additionally the reference singals recorded always overlapped when plotted as per figure Figure 3-4.

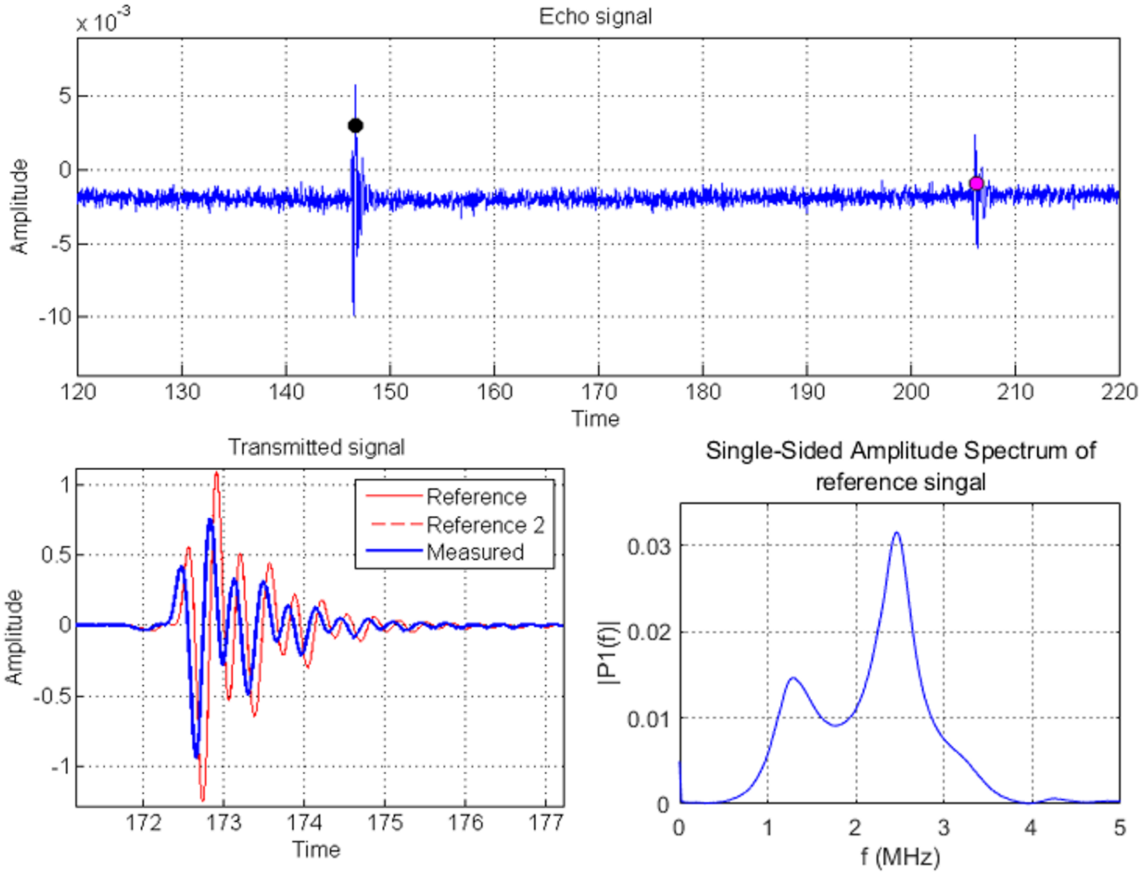

Figure 3-4: Example of a FAIS measurement. Top, the echo signals recorded. Bottom left, the two reference and the transmission signals. Bottom right Fourier transform of the reference signals

This process for calculating the attenuation α uses the approximation:

$$\alpha = \frac{I_{loss}}{d}$$

Equation 3.12

This approximation is only valid for samples acoustically matched to water, where the reflections due to the impedance mismatch are small and their contribution to attenuation can be ignored. A more accurate representation of the insertion loss I_{loss} will be the addition of the attenuation α and the reflection losses. For a single sample, the insertion loss I_{loss} is:

$$I_{loss} = 2 \cdot Refl + \alpha \cdot d$$

Equation 3.13

Where $Refl$ represents the reflection losses. We multiply it by two due to the fat they are present when the wave travels into the sample and out of it. Equation 3.12 is only justified in cases were $\alpha \cdot d \gg Refl$. However, if this approximation is unrealistic, the process can be modified by measuring the attenuation of samples of different lengths. The contribution from reflections can then be removed since $Refl$ is not a function of the thickness of the samples. For two samples with different thicknesses the difference between transmission losses will be:

$$I_{loss} - I'_{loss} = [2 \cdot Refl + \alpha \cdot d] - [2 \cdot Refl' + \alpha \cdot d']$$

Equation 3.14

$$I_{loss} - I'_{loss} = \cancel{(2 \cdot Refl - 2 \cdot Refl')} + \alpha \cdot d - \alpha \cdot d' = \alpha(d - d')$$

Equation 3.15

Thus, the difference between insertion losses of two samples divided by the difference in thicknesses of the samples can be used to accurately measure the attenuation of the material.

In our system, measurements are obtained by sending 200 pulses through the sample and averaging the results. Where the sample is homogeneous, the results of the measurements at different points of the sample can be averaged.

It is important to control the temperature of the water to minimize uncertainties in the value of the SoS. Additionally, water should be degassed, as the presence of gas in water increases its scatter. The resulting attenuation data after processing the insertion losses through the Fourier transform is obtained for frequencies from 1.5 to 3.5 MHz at 0.1 MHz intervals.

3.2.2 Sample holders

In order to hold the gel samples for the FAIS measurements, custom sample holders (Figure 3-5) were designed. These were designed to hold solid samples without the need for membranes, which may add reflections to the measurements. The sample holder consists of a body and a lid. The lid has a helical screw-like thread along a circular opening that offers an acoustic window for characterization. The body has a complementary helical thread, along with an opening of the same dimensions. Both openings align, allowing the propagation of the acoustic pulse through the sample and the screw-like thread allows adjustment of the lid to provide samples of differing thickness.

Figure 3-5: Adjustable, membrane-less solid sample holder. Left, the lid, Right, the body.

The sample holder is designed for cylindrical samples 57mm in diameter. It relies on the extension of the 5mm lips of the acoustic windows into the sample to press the sample from both sides, keeping it in place.

For the characterization of liquid samples, a specific sample holder design (Figure 3-6) was used. This holder consists of a central metallic piece of a quasi-annular section that has six screw-holes on each of its sides. Mylar membranes can be placed on either side along with O-rings that fit into a series of circular grooves that ensure a tight seal. Plastic quasi-annular pieces, which act as lids, are then placed on either side and the sample is screwed firmly. Once the sample holder is mounted, two small screws on the side can be opened in order to fill the sample holder. One of the holes can be used to pour or inject the liquid sample while the other allows air to leave the cavity. To prepare samples of different thicknesses, different central pieces were used.

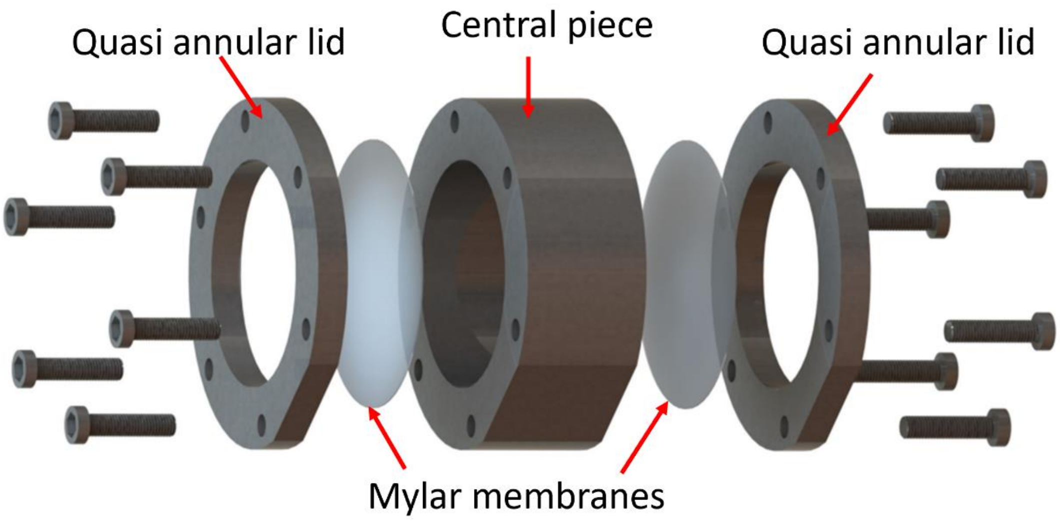

Figure 3-6: Liquid sample holder.

3.3 Measurement of density

The measurement of density was carried out by using Archimedes' principle. The apparent weight of the sample is measured when it is hanging from a balance in air and when it is submerged in water. These must be corrected for the weight of the holding device (a metal cage in our case) in both scenarios. The buoyancy is defined as the difference between the two measurements and the ratio of the apparent weight to the buoyancy gives a resulting density relative to that of the water in which it is submerged. By measuring the temperature of the water, the density of the sample can be calculated as follows:

$$\rho_{sample} = \rho_{water} \frac{(W_{sample} - W_{holder})_{in\ air}}{(W_{sample} - W_{holder})_{in\ air} - (W_{sample} - W_{holder})_{in\ water}}$$

Equation 3.16

Where ρ represents the density of the corresponding materials and W the weight of the corresponding object under the specific circumstances. The apparent weight of the samples is reduced when the samples are submerged due to the buoyancy force of the water, which is equivalent to the weight of the water displaced. This buoyancy force is dependent on the density which itself is dependent on temperature. Therefore, for these measurements to be valid, they should all be performed at the same temperature.

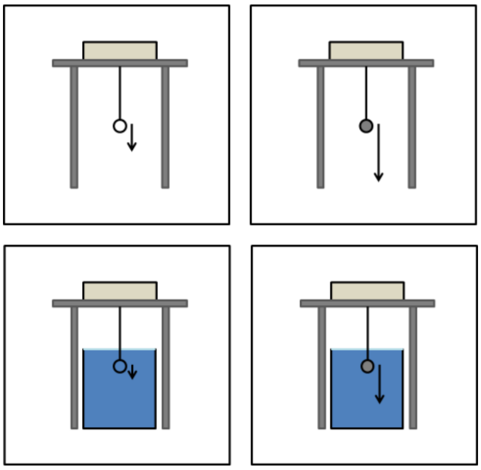

Figure 3-7: Schematic of the application of Archimedes principle. Top left, empty cage in air. Top right, cage, and sample in air. Bottom left, empty cage in water. Bottom right, cage, and sample in water.

3.4 Measurement of thermal properties

Thermal conductivity, diffusivity and volumetric heat capacity were measured using a HOTDISK (TPS 2500 S[84].) analyser. A Kapton-insulated sensor is sandwiched between two samples of the material being characterized. The sensor consists of a thin metallic spiral with multiple arms, through which the current is passed to increase the temperature. The temperature evolution is recorded, and the thermal properties are calculated. The system requires a preliminary estimation of the thermal properties (volumetric heat capacity, thermal diffusivity, thermal conductivity) to decide the power regime provided to the anode. The samples should be at least 15 mm thick. After the measurements, the system provides a minimum thickness for which the measurements are valid. Several iterations may be required until the results converge.

Since the samples are essentially water trapped in a polysaccharide matrix, the effect of diffusion of water within the samples on the measurements was evaluated. After consulting with the manufacturer, it was found that altering the measurement parameters would allow detection of this phenomenon.

The melting point of the gel was a complex process to address. Simply heating a sample and measuring the temperature to determine when it melts is not adequate, since the hydrogel will lose water, drying out and changing its properties in the process. Putting the sample in water and heating it to see when it melts is also a faulty process, since the hydrogel slowly starts to dissolve in the liquid.

It was found that the best way to determine the melting point of these specific samples was to cast some of the gel into a small tube such that a bubble of air would form at the bottom, and to push a thermocouple to the interface between the gel and the air. The tube was then sealed and submerged in a water bath to heat up. Doing it this way means that the gel is not in direct contact with the water, preventing it from dissolving and drying out, since the moisture is trapped within the container. The thermocouple allows temperature measurement close to the interface where the melting is easy to observe, since the gel will start to leak into the bubble when it melts.

3.4.1 Characterization of the dye

In order to create a thermochromic gel, it was decided to incorporate a thermochromic dye (MB-60 NH, Hallcrest) following the work of Ambrogio et al[69]. Thermochromic materials are those that have a temperature dependent transition which results in a change in colour. This is often driven by a chemical reaction in which various compounds react to form a different compound, or by a change in the molecular structure of certain chemicals such as the crystallization of proteins, such as collagen, or bovine albumin serum, which has been used in the past[59].

The MB-60 dye relies on the combination of cholesteric and chiral nematic liquid crystals which are themselves microencapsulated in polymer coatings. These microcapsules contain the thermochromic molecules which give rise to the colour change in the dyes. The microcapsules are suspended in a liquid solution.

The colour change of the samples was assessed by photographing the samples after heating in a water bath with the temperature of the water bath controlled by a thermocouple. The samples were prepared by pouring the gel into a tube and embedding a thermocouple into it. The samples were heated to temperatures from 40°C to 70°C in steps of 5°C. The samples were left for 10 minutes inside the water bath after reaching the desired temperature before capturing the image.

While the technical specifications of the dye indicate that it has irreversible behaviour it was clear that this was not the case when preparing the gels that contain the dye. This behaviour was evaluated by preparing a sample, as for the assessment of the colour change, heating the sample and allowing it to cool down while observing any subsequent colour change.

3.5 Measurement of radiological properties

In order to test the radiation resistance of the gel, it was exposed to a dose of radiation equivalent to the amount we estimated a heavily used gel might be exposed to after a year of use, and then multiplied it by six. This resulted in 3 kGy of dose ($2\,Gy/d \cdot 5\,d/wk \cdot 52\,wk/yr \cdot 6{\sim}3\,kGy$). This values represents 1500 times the typical dose 2Gy per fraction[43,44]. Furthermore, it is not necessary to deliver a full therapeutic dose to perform a QA test.

It was initially expected that the rate of irradiation and fractionation could have different effects for the same total dose as in the case of tissues. As presented in the review by Singh and Singh{85}, there are 3 different stages (Physical, Chemical and Biological) to radiological damage, that occur one after the other on different time-scales. However, in the case of a physical phantom, only the first two stages are present. In the particular case of a hydrogel, the associated time-scale would be that of hydroxyl radicals, free electrons and free hydrogen ions recombining, which have a time scale of $10^{-7} - 10^{-3}$ s[85]. It can be concluded that the difference between a single fraction and multiple fractions would be the heat associated with the irradiation, which could result in greater damage, as the average energy of the molecules would increase, bridging the energy gap for ionization. It was therefore decided to evaluate the effect of the single fraction dose first and that if any effect were found, multiple fractions would be evaluated. If there was no effect found, higher doses would be tested. The heat rise associated with 3 kJ/kg, assuming a heat capacity similar to that of water, would result in a temperature rise of 0.7°C, assumed to be negligible.

The irradiation was carried out at NPL using a cobalt source. A single sample was made and cut in half. After irradiating one of halves, the results from the FAIS method of both samples were compared. Cutting a large sample into two should reduce any influence of inter-sample variation and ageing.

To characterize the samples in terms of absorbed dose under fixed conditions, it was decided to perform a CT scan to obtain the CT number for the materials. CT numbers are measured in Hounsfield Units (HU), and they represent a comparison of the linear attenuation coefficient of a given material relative to water. This parameter is directly proportional to the density of the material, which can be used to quantify the homogeneity of the samples and the processes of preparing the samples. CT scans were performed with a Siemens Confidence (Siemens, Germany) at 120 keV.

The CT data was then inserted into a Raystation treatment planning system (Version 10A, RaySearch Laboratories, Sweden). This would allow production of the expected dose profiles and an estimate the expected dose delivery within the samples. These results can then be compared with a simple absorbed dose measurement within the samples. The exposures were done with an Elekta Synergy linear accelerator at 6MeV, which was the same beam used in the treatment planning simulation.

The absorbed dose measurement was done by delivering 200 Monitor Units (MU) to an inonization chamber under 10 cm of plastic water to calibrate the response of the chamber based on the linac's calibration. An exposure of 200 MU was then delivered to the ionization chamber under the gel samples to obtain a measurement of the absorbed dose.

A good agreement between the predicted and measured values would indicate that the samples are good candidates for radiotherapy phantoms. The main source of discrepancies would be the constituent material of the phantom. However, considering the components and their relative proportions, this was thought to be unlikely.

3.6 Statistical analysis

P values have been calculated and presented were appropriate with the intent to compare two magnitudes and identify whether they are statistically different. The corresponding z value for the null hypothesis being that the two magnitudes are the same is calculated as:

$$z = \frac{|\bar{x}_1 - \bar{x}_2|}{\sqrt{\sigma_1^2 + \sigma_2^2}}$$

Equation 3.17

Where $\bar{x}_1$ and $\bar{x}_2$ represent the magnitudes being compared and σ_1 and σ_2 represent the corresponding uncertainties. The p value is then calculated from the normalized gaussian function. As per standard scientific practise, to magnitudes are considered statistically different for values of $p < 0.05$.

3.7 Uncertainty calculations

A simplified uncertainty budget has been calculated for the measurement of density, acoustic and thermal properties. Random and Systematic uncertainties have been combined in quadrature. Random uncertainty arose from multiple points in the same material (when using the FAIS system) and from averaging multiple samples.

Systematic uncertainty is obtained by the simplified formulation in the previous sections, using the combination for uncorrelated quantities reported in the GUM guide (ref.):

$$(ux)^2 = \Sigma\left(\frac{\partial f(x)}{\partial y} uy\right)^2$$

Relative uncertainties are represented by u and absolute uncertainties are represented by U

The relative uncertainty associated with the attenuation α from Equation 3.12 is:

$$u\alpha^2 = uV^2 + ud^2$$

Equation 3.18

Where $u\alpha$ represents the relative uncertainty in α, $uV$is the relative uncertainty associated with the recording of the electrical pulses and ud is the relative uncertainty in the thickness d.

uV was calculated by taking the beginning of a recorded pulse, before the pulse has and the measurement is only noise, and dividing it over the amplitude of the pulse. This produced a noise to signal ratio which was used as a way to estimate the relative uncertainty of the measurement.

The relative uncertainty associated with the thickness d of a sample from Equation 3.11Equation 3.12 is:

$$ud^2 = ut_{trans}^2 + ut_{ref}^2 + ut_1^2 + ut_2^2 + uc_w^2$$

Equation 3.19

Where ud is the relative uncertainty in d. Each of the ut_y is the relative uncertainty in each of the corresponding times and was calculated as the half period of the pulses divided by the measurement.

The relative uncertainty for the values of the speed of sound in water c_w only take into account the temperature dependence and is calculated as follows:

$$uc_w\,(T) = \frac{1}{c_w}\frac{\partial c_w(T)}{\partial T}\mathrm{U}T$$

Equation 3.20

Where uc_w is the relative uncertainty in c_w, the speed of sound of water, UT is the uncertainty in temperature and $\frac{\partial c_w}{\partial T}(T)$ is the partial derivative with temperature of the polynomial used to calculate c_w.The value of UT was chosen as 0.5°C, since is the standard accepted uncertainty in the most thermometers. These uncertainties will depend on temperature as the factor $\frac{\partial c_w}{\partial T}(T)$ does.

The relative uncertainty for values of the speed of sound in a sample c_s from Equation 3.9

$$uc_s^2 = ut_1^2 + ut_2^2 + ud^2$$

Equation 3.21

Where uc_s is the uncertainty in c_s and ut_1 , ut_2 ud are the relative uncertainties of the corresponding t_1, t_2 and d.

Additionally, for FAIS measurements, the results are the average of the measurements for all the points measured. For a given property p_{sample} the uncertainty will be

$$(\mathrm{U}p_{sample}) = (\mathrm{U}p_{prop})^2 + (\sigma p_{points})^2$$

Equation 3.22

Where Up_{sample} is the absolute uncertainty of p_{sample}, Up_{prop} is the absolute systematic uncertainty associated with the measurement of the property p and σp_{points} is the standard deviation of the property p, .

The uncertainty for the density ρ_{sample} from Equation 3.16

$$u\rho_{sample}^2 = u\rho_w^2 + 2u(W_{sample})_{air}^2 + 2u(W_{holder})_{air}^2 + u(W_{sample})_{water}^2 + u(W_{holder})_{water}^2$$

Equation 3.23

Where $u\rho_w$ is the uncertainty in the density of water, and uW are the relative uncertainties in the corresponding measurements of weight. These uncertainties in weight were calculated as 0.1 mg divided by the measurement.

$u\rho_w$ was calculated as:

$$u\rho_w(T) = \frac{1}{\rho_w}\frac{\partial\rho_w(T)}{\partial T}\mathrm{U}T$$

Equation 3.24

Where $u\rho_w\,(T)$ is the relative uncertainty in ρ_w, the density of water, $\mathrm{U}T$ is the uncertainty in temperature and $\frac{\partial\rho_w}{\partial T}(T)$ is the partial derivative with temperature of the polynomial used to calculate ρ_w.The value of $\mathrm{U}T$ was chosen, again, as 0.5°C. These uncertainties will depend on temperature as the factor $\frac{\partial\rho_w}{\partial T}(T)$ does.

For all measurements provided where the result is the average of various samples, the absolute uncertainties for the property p are:

$$\left(\mathrm{U}p_{average}\right)^2 = \left(\sigma p_{samples}\right)^2 + \sum_n \left(\frac{\mathrm{U}p_{sample}}{n}\right)^2$$

Equation 3.25

Were $\mathrm{U}p_{average}$ is the uncertainty of the average, $\sigma p_{samples}$ is the standard deviation for the value of p of the n samples and $\mathrm{U}p_{sample}$ is the uncertainty of each of the samples. Thermal properties lacked an uncertainty, as the measuring device did not provide one, and the uncertainty as taken directly as the standard deviation of the measurements between the samples,

The calculation of uncertainties for values derived from data fits was done using SciDavis 2.3.0 an open-source code developed by Russell Standish available at http://scidavis.sourceforge.net/. SciDavis enables the propagation of uncertainties from the datasets into the fits and uses a Scaled Levenberg-Marquardt algorithm with tolerance of 0.0001.

4 Results

This chapter presents the measured properties of different samples, and the effects of addition of different components on the acoustic, thermal, and radiological properties of the samples.

It also shows the effects of ionizing radiation on the acoustic properties of the samples.

4.1 Acoustic properties

4.1.1 Gellan gum concentration

Samples with gellan gum of 1, 2 and 4% by weight were prepared. Although it was possible to prepare 1% samples, these were too soft and could be damaged by simple handling. They were therefore discarded after attenuation measurement were done. In general, lower concentrations resulted in easily damaged, softer samples, whereas the higher concentrations gave more rigid and solid samples. Concentrations of 5% and higher were also tested. However, since the results from acoustic characterization were inconsistent (the difference between them being bigger than 3 times the combined standard deviation) it was decided not to use these higher concentrations. Furthermore, their manufacturing process was more complicated as they required gradual addition of the gellan gum to the mixture while the samples were being prepared, as a concentration of 5% in weight appeared to be above the saturation point for mixtures below 50 °C. The origin of these inconsistencies could be the difficulty in consistently adding the gellan gum as the sample heats up, as differences in the rate of addition of the power could have led to the formation of clumps that were not dissolved in the process or could be related to the cooling process, since the sample will be cooling down and reaching temperatures at which the concentration of gellan gum raises above the saturation point. It is conceivable that this could result in inhomogeneities that would be dependent on the rate of cooling, which is a parameter that is hard to control.

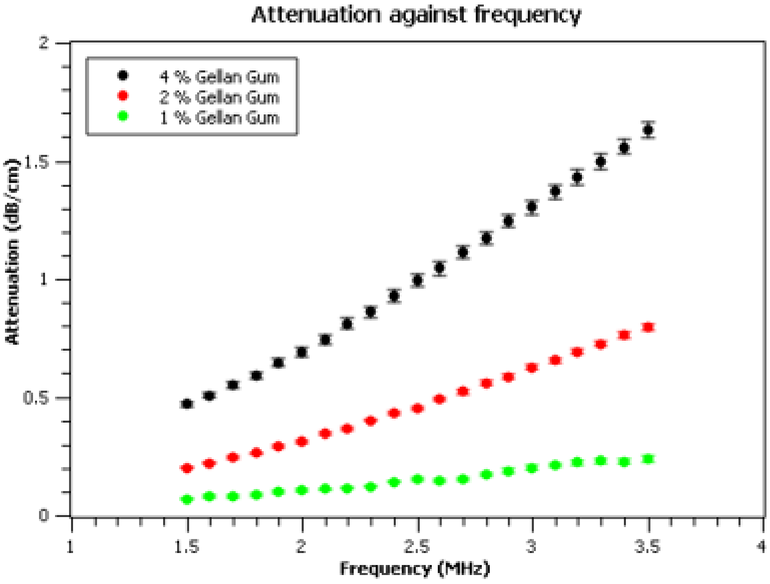

Figure 4-1: Attenuation of gellan gum samples of 1,2 and 4% wt. concentrations at 20°C

Figure 4-1 shows the attenuation of samples with concentrations of 1%, 2% and 4%. Values are obtained from the average of two samples, each measured twice in 21x21 1mm spacing square grids. Error bars show one standard deviation. As can be seen, the attenuation of the samples increases with increasing gellan gum concentration.

Fitting the data to the curve $\alpha = \alpha_0 \cdot f^n$ gives the following parameters:

	1 %	2 %	4 %
$\alpha_0 \left(\frac{\text{dB}}{\text{cm}}\right)$	0.035 ± 0.004	0.112 ± 0.011	0.246 ± 0.025
n	1.6 ± 0.1	1.7 ± 0.1	1.5 ± 0.1

Table 4-1: Fit parameters for concentrations of 1,2 and 4% in wt.

Sample attenuation (n=3) was measured for a range of temperatures from 20 to 45°C. As can be seen in figures Figure 4-2 their attenuation reduced with increasing temperature. The changes in α_0 and n is shown in Table 4-2:

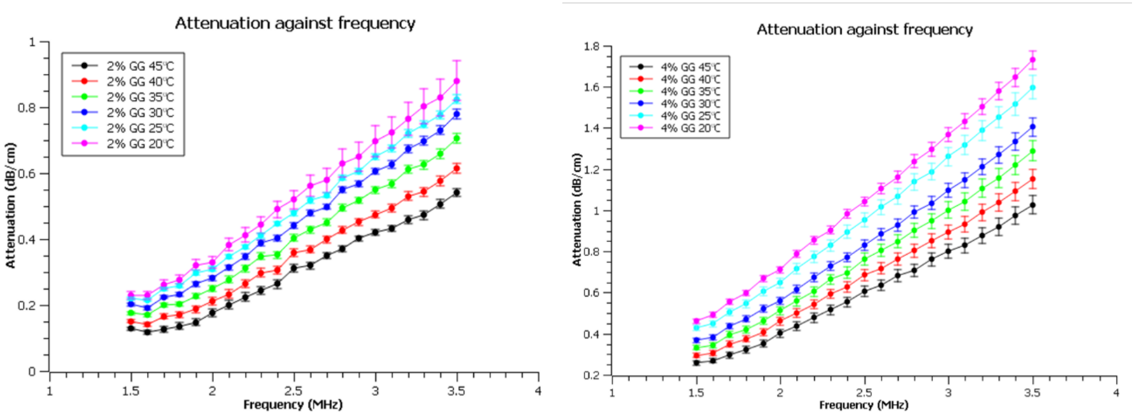

Figure 4-2: Attenuation of 2 and 4% gellan gum (GG) samples with temperature.

2% Gellan gum						
T (°C)	20	25	30	35	40	45
α_0	0.112 ± 0.011	0.101 ± 0.010	0.088 ± 0.009	0.076 ± 0.008	0.063 ± 0.006	0.050 ± 0.005
n	1.7 ± 0.1	1.7 ± 0.1	1.7 ± 0.1	1.8 ± 0.1	1.8 ± 0.1	1.9 ± 0.1
4% Gellan gum						
T (°C)	20	25	30	35	40	45
α_0	0.246 ± 0.025	0.222 ± 0.022	0.189 ± 0.019	0.168 ± 0.017	0.149 ± 0.015	0.127 ± 0.012
n	1.5 ± 0.1	1.6 ± 0.1	1.6 ± 0.1	1.6 ± 0.1	1.6 ± 0.1	1.7 ± 0.1

Table 4-2: Fit parameters for 2 and 4% gellan gum samples at temperatures from 20 to 45℃.

For each concentration it can be seen that the attenuation decreases with increasing temperature.

Speed of sound measurements indicate a small, indistinguishable (p$\in$ (0.08,0.65) average $p = 0.27$) difference in speed of sound values for 2 and 4% gellan gum samples.

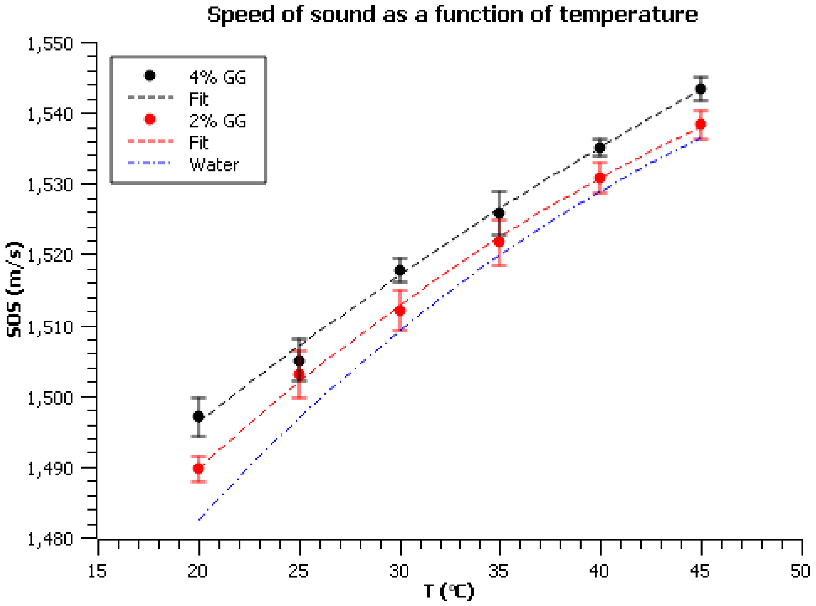

Figure 4-3. Speed of sound for 2 and 4% samples compared to water. Fits have been made to a second order polynomial.

The value for water measurements has been obtained from a 5th polynomial fit as described by Bilaniuk and Wong[86]. As can be seen, there is a small but steady increase in the speed of sound with increasing gellan gum concentrations, although small overlaps can be seen at certain temperature points.

The fits of the data here have been made to a second order polynomial of the type $a + bx + cx^2$. While this is significantly lower order than the 5th polynomial fit for which the reference dataset covered points from 0 to 100°C at intervals of 0.1°C. As our dataset has only 6 points, using polynomials of a higher order than 2nd is unlikely to produce valuable information, and is more likely to be subject to mathematical aberrations.

Gellan gum	a	b	c	R^2
2%	1432±15	3.30±0.99	-0.021±0.015	0.9995
4%	1448±15	2.67±0.94	-0.012±0.014	0.9978

Table 4-3: second order fit parameters for 2% and 4% gellan gum samples.

Given the R^2 for these fits, it is unlikely that the use of higher polynomials would produce valuable information. A 5th order polynomial would artificially produce a perfect fit since 6 points describe a unique 5th order polynomial.

4.1.2 Zinc Acetate as a doping agent

The addition of zinc acetate was studied. Data is reported in terms of the molarity of the concentration (mol/L). This would technically mean that a gellan gum sample should be reported as a different concentration, since the concentrations were characterized as concentrations in weight and the weight of the sample is susceptible to change, since the water trapped in the polysaccharide matrix was replaced with a zinc acetate solution which would not necessarily have the same density. However, the data is not reported in this way since we wanted to be able to compare the change in attenuation in the original sample resulting from the addition of the salt.

In order to measure the attenuation of liquid solutions, they were contained in holders sealed with optically transparent mylar membranes. As discussed in section 3.2, the effect of membranes can be removed by performing the measurement in samples of different thicknesses. Samples of 5, 10 and 20mm thickness were used. Each was measured twice across a grid of 441 points, and the average was used to characterize the sample:

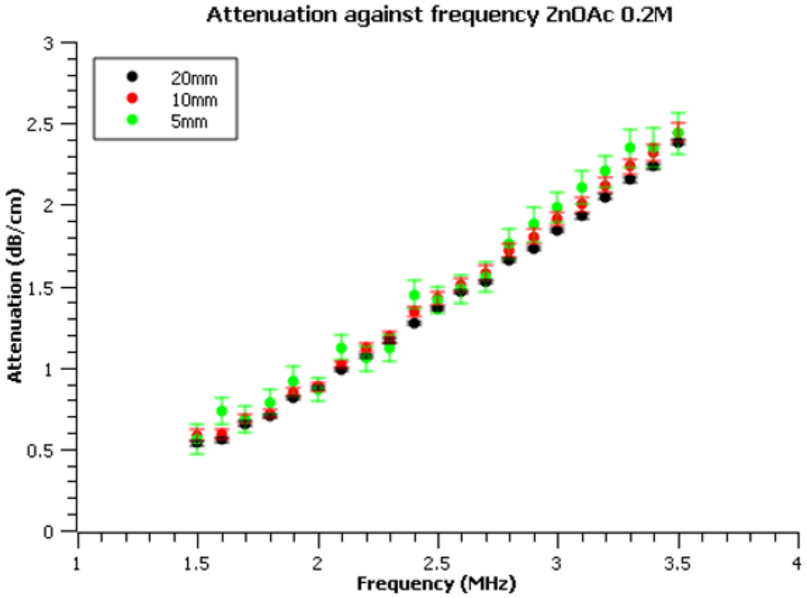

Figure 4-4. Attenuation as a function of frequency of three different thicknesses (5,10,20 mm) of solutions of ZnOAc at 0.2M at 20°C.

Figure 4-4 shows an example of such a measurement for the zinc acetate. In this case, it can be seen that there is good agreement in attenuation for the three different thicknesses. This indicates that the attenuation of the solution dominates over the effect of the membrane. It can also be seen that thinner samples are more susceptible to noise and thus present bigger uncertainties.

As described in section 3.2, these values can be combined in pairs to produce corrected values of attenuation.

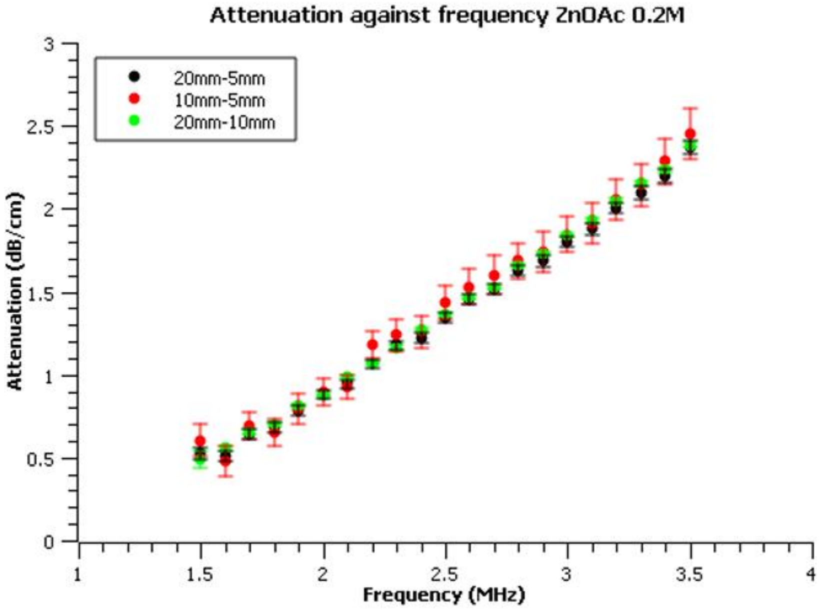

Figure 4-5. Example of the corrected values obtained from measurements for 0.2 M ZnOAc solutions at 20°C

Figure 4-5 show the corrections resulting from the three possible combinations in pairs of the 20, 10 and 5 mm measurements. In this case the 10 and 5 mm datasets are noisiest, since these are the thinnest samples. These three sets of values were then averaged to produce a final result for the attenuation of the 0.2M sample at 20°C. This process was repeated for each temperature and for the 0.3 and 0.4 concentrations of ZnOAc.

For 0.2M samples in the temperature range from 20 to 45 °C:

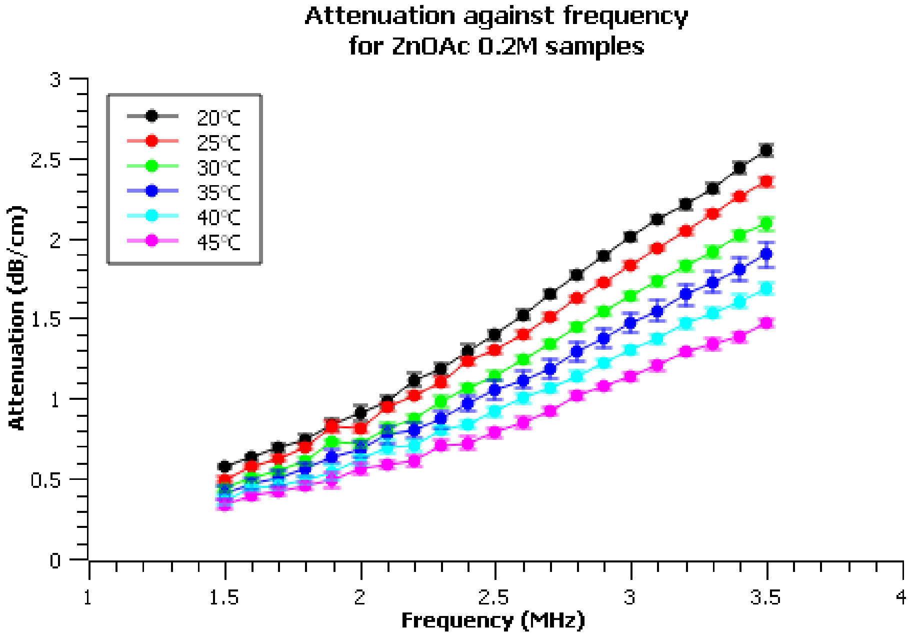

Figure 4-6. Attenuation for 0.2M ZnOAc samples across the 20 to 45°C temperature range as a function of frequency.

T (°C)	20	25	30	35	40	45
α_0	0.264±0.052	0.245±0.050	0.207±0.046	0.195±0.045	0.174±0.042	0.159±0.040
n	1.8±0.1	1.8±0.1	1.9±0.1	1.8±0.1	1.8±0.1	1.8±0.1

Table 4-4. Attenuation parameters for 0.2 ZnOAc solutions for 20 to 45°C.

For 0.3M samples in the temperature range from 20 to 45 degrees Celsius:

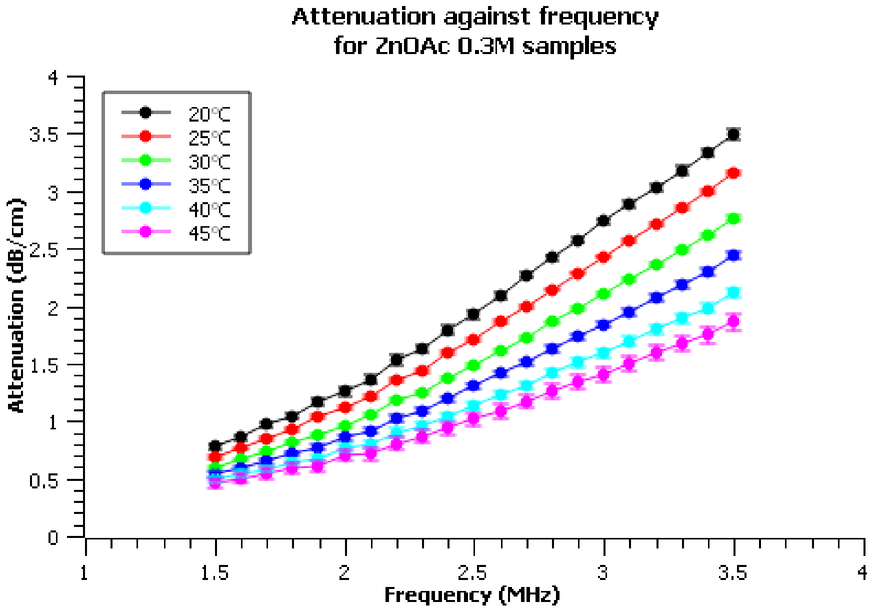

Figure 4-7. Attenuation for 0.3M ZnOAc samples across the 20 to 45℃ temperature range as a function of frequency.

T (°C)	20	25	30	35	40	45
α_0	0.368±0.61	0.319±0.057	0.269±0.052	0.239±0.049	0.219±0.047	0.207±0.046
n	1.8±0.1	1.8±0.1	1.9±0.1	1.9±0.1	1.8±0.1	1.7±0.1

Table 4-5. Attenuation parameters for 0.3 ZnOAc solutions across the 20 to 45℃ range

For 0.4M samples of for the temperature range 20 to 45°C:

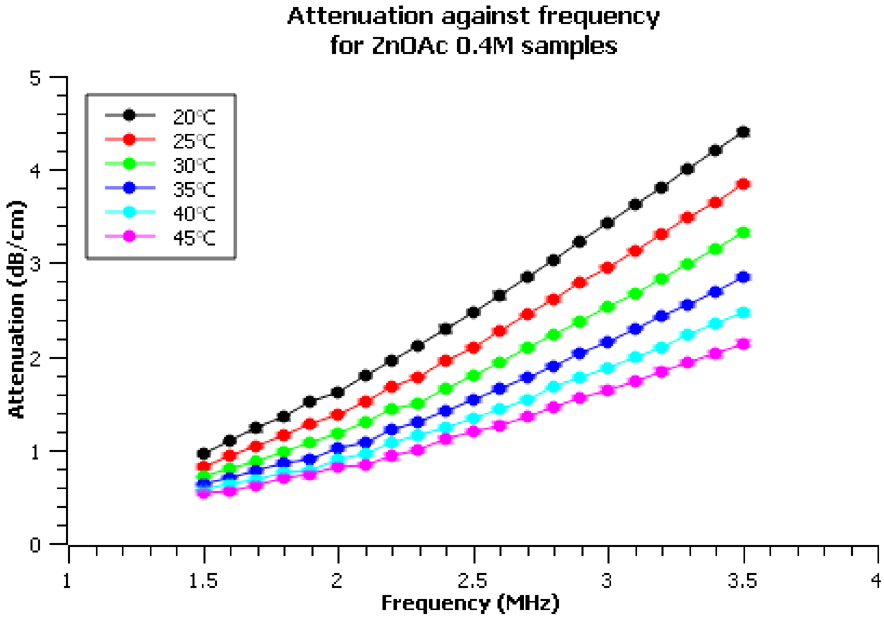

Figure 4-8. Attenuation for 0.3M ZnOAc samples across the 20 to 45℃ temperature range.

T (°C)	20	25	30	35	40	45
α_0	0.481±0.69	0.397±0.063	0.331±0.058	0.289±0.054	0.260±0.051	0.244±0.050
n	1.8±0.1	1.8±0.1	1.8±0.1	1.8±0.1	1.8±0.1	1.7±0.1

Table 4-6. Attenuation parameters for 0.4 ZnOAc solutions across the 20 to 45℃ range

To examine the validity and viability of the infusion process, a 2% gellan gum sample was infused with 0.4M ZnOAc, characterized, cut in half and remeasured. Since the salt diffuses through the sample surfaces and concentration equilibration is gradual, differences for different sample sizes would indicate an incomplete process.

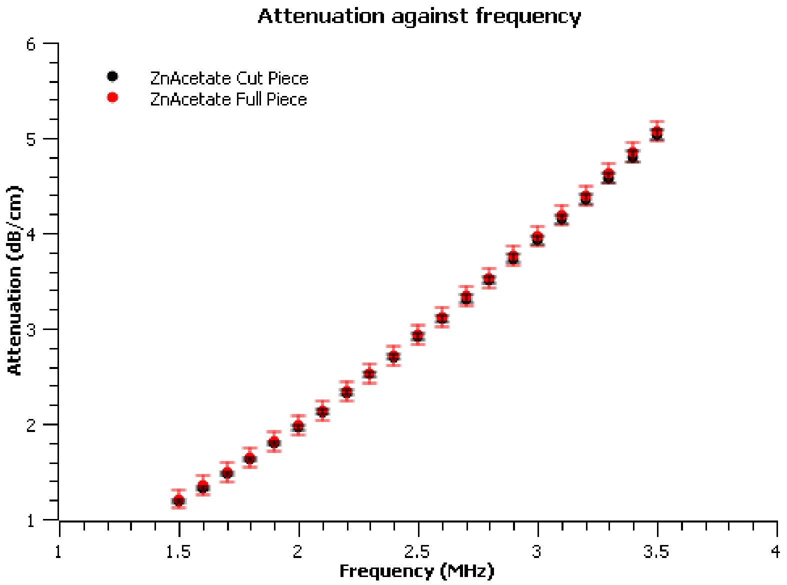

Figure 4-9.Comparison of the attenuation at 20°C of the full piece and one of its halves as a function of frequency.

Figure 4-9 and the associated data shows that the infusion process was successful and that no more time was needed for the samples to reach equilibrium ($p = 0.82$).

In order to examine the effect of the different concentrations of the salt on 2% gellan gum samples, we tried to isolate the effect of ZnOAc. Since all measurements are referenced to water, the attenuation of a ZnOAc solution represents the increase in attenuation due, solely, to the addition of the salt. Then, to evaluate the effect of infusing a sample with the salt, the attenuation of gellan gum samples was subtracted from the attenuation of the corresponding infused samples, the resulting value should be comparable to the attenuation of the ZnOAc solution.

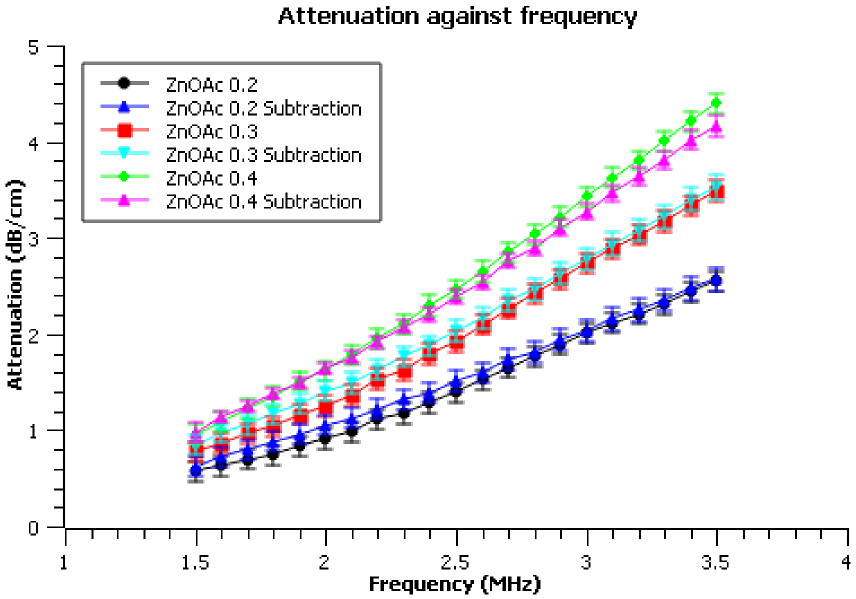

Figure 4-10. Comparison of the attenuation of 0.2, 0.3 and 0.4 M ZnOAc solutions 20°C with their corresponding increase in attenuation caused in gellan gum samples.

As Figure 4-10 shows, there is good agreement between the measured increase in attenuation due to the ZnOAc solutions and the attenuation of the solutions themselves. To further test the applicability of this result, an additional measurement was made using the same ZnOAc concentration on samples with different gellan gum concentrations.

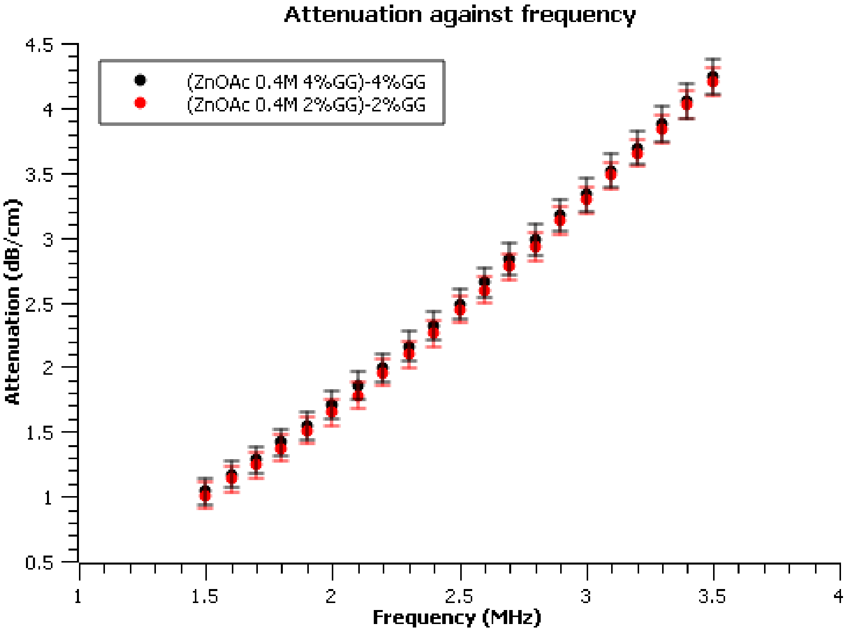

Figure 4-11. Comparison of the increase in attenuation at 20°C due to a 0.4 M ZnOAc infusion in a 2 and 4 % gellan gum sample.

As can be seen in Figure 4-11, the increase due to the 0.4 M ZnOAc infusion was the same for both the 2 and 4% gellan gum samples ($p = 0.77$).

Returning to the original idea presented in Equation 3.4, that the attenuation of the samples could be expressed as the sum of the independent effects of the gellan gum and the ZnOAc, plus an additional term representing their interaction, the data presented in figures Figure 4-10 and Figure 4-11 indicates that given a fixed concentration of either component, changing the other shows no additional effects. In a way, these are the partial derivatives of the Equation 3.4 with respect to the variables “GG” and “ZnOAc” and we find that their cross-interaction term is either zero or negligible.

The same analysis was performed for the speed of sound increase associated with gellan gum 2% samples infused with zinc acetate and their corresponding solutions in water.

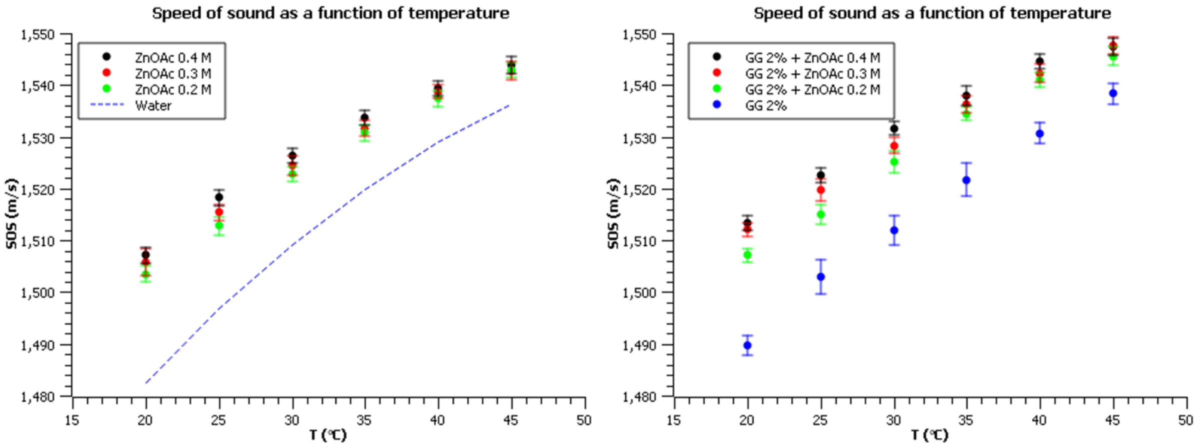

Figure 4-12. Left, comparison of the SoS of different ZnOAc concentrations and water. Right, comparison of the ZnOAc infused samples and the uninfused gellan gum sample.

The corresponding second order fits ($a + bx + cx^2$) can be found in Table 4-7.

ZnOAc Solution	a	b	c
0.2 M	1450±10	3.12±0.63	-0.023±0.010
0.3 M	1452±14	3.21±0.86	-0.026±0.013
0.4 M	1451±10	3.45±0.65	-0.030±0.010
Gellan gum infused sample			
0.2 M	1454±10	3.08±0.67	-0.023±0.010
0.3 M	1469±10	2.47±0.65	-0.016±0.010
0.4 M	1458±10	3.35±0.66	-0.030±0.010

Table 4-7: Polynomial fits for the SoS of ZnOAc solutions and 2% GG samples.

In order to evaluate the effect, the increase in speed of sound from the infusion was calculated, and the measured speed of sound increase in the corresponding solution subtracted

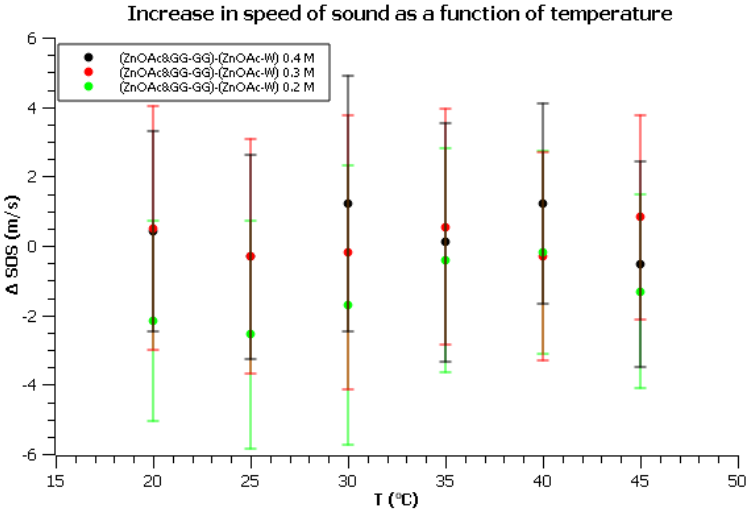

Figure 4-13. Subtraction of the increase in SoS at 20°C due to infusion and the increase in SoS to its corresponding ZnOAc solution.

Figure 4-13 shows that the difference in the increase in SoS for both methods is statistically negligible, $p = 0.81$ for the for the hypothesis of these values being 0. Additionally, the associated uncertainties are of the order 2 m/s in 1500 m/s, an uncertainty of 0.13%.

To get a better perspective of the overall effect we can plot the SoS of the ZnOAc samples and compute the increase in SoS:

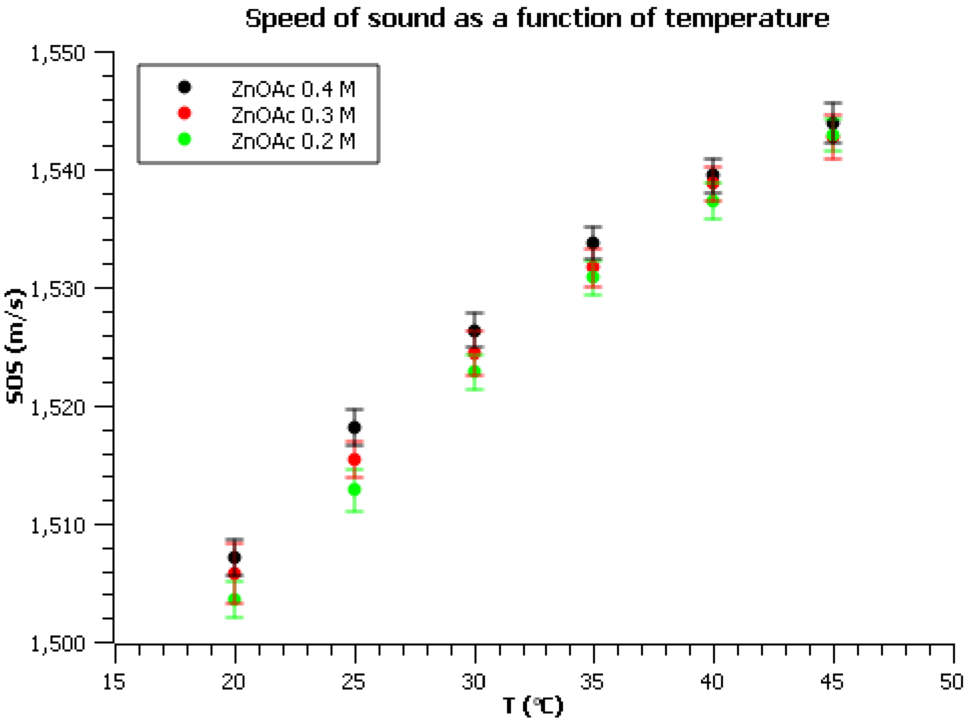

Figure 4-14: SoS of ZnOAc samples at concentrations of 0.4, 0.3 and 0.2 M, as Figure 4-12 without the values of water.

	20°C	25°C	30°C	35°C	40°C	45°C
0.2 M	21.1±1.5	16.1±1.7	13.6±1.5	11.0±1.5	8.5±1.5	6.5±1.4
0.3 M	23.4±2.5	18.7±1.5	15.3±1.9	11.9±1.6	9.8±1.4	6.3±1.8
0.4 M	24.7±1.5	21.5±1.5	17.1±1.5	13.9±1.4	10.6±1.4	7.5±1.7

Table 4-8. SoS increases for the ZnOAc solutions for the 20 to 45℃ temperature range

Figure 4.14 and Table 4-8 show that there is a slight, but often overlapping increase in SoS with increasing ZnOAc concentrations. The effects also change with temperature, being more notable at low temperatures. This effect is expected to be the same, regardless of gellan gum concentration and due to its magnitude, and should be taken into account when designing a TMM using these materials

These findings do not indicate that the cross interaction terms for attenuation or SoS are zero, since the solubility of ZnOAc is 1.82 M[87] and we only tested up to 0.4 M. Studying beyond this point could have academic relevance, but is unlikely to find applicability since 0.4 M already gives high values of absorption and is unlikely to be needed to produce TMMs. With regards to the gellan gum concentration, 4% is the highest concentration that can feasibly be tested since, as explained in section 4.1.1, 5% gellan gum concentrations are hard to produce and do not produce reproducible samples.

As it was known that zinc acetate could diffuse into the samples it was decided to analyse the rate at which the zinc would diffuse out of the samples. For this, a sample was measured at 30-minute intervals over 2 hours, between which the sample was stored in a 1l container. During measurements, the container water was replaced with clean water. This time frame was chosen as it is representative of the maximum measurement times.

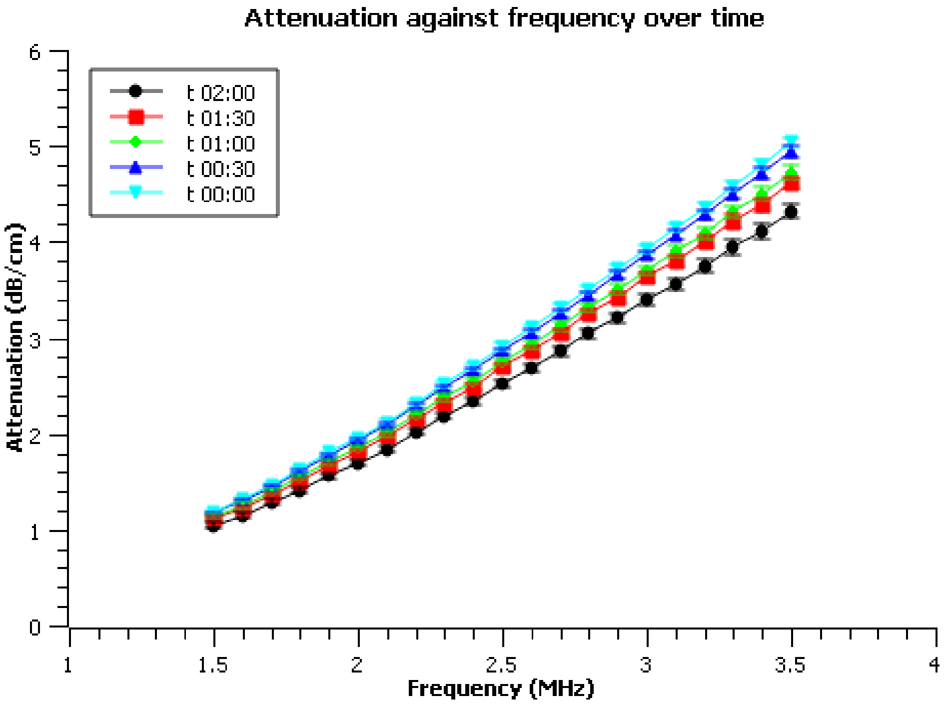

Figure 4-15. Measurement of the ZnOAc salt diffusing out of the sample. The measurements correspond to a single sample measured at the different times t covering 0 to 2 hours at 30-minute intervals. Measurements were done at 20°C.

As Figure 4-15 shows, there was a slight decrease in the attenuation of the sample due to the diffusion of ZnOAc out of the sample to the container (for t=0 and t=2h, $p = 1.57 \cdot 10^{-7}$).

It was then decided to leave a sample in a container with pure water overnight and it was found that ZnOAc crystals formed beneath the surface of the gel.

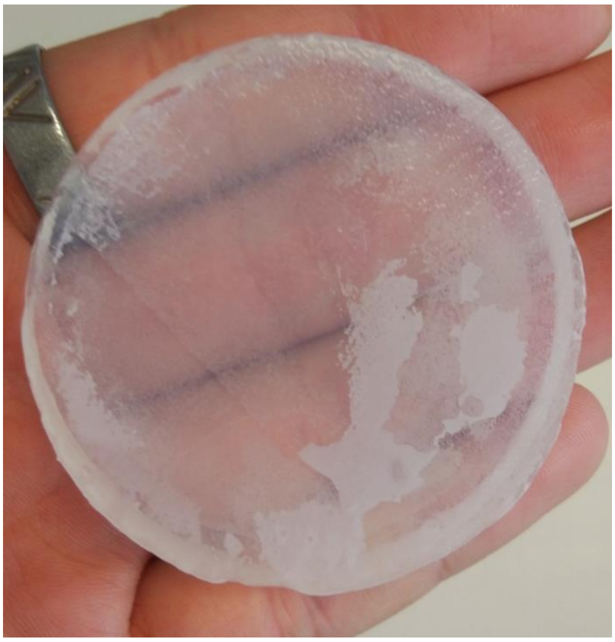

Figure 4-16. Example of the crystals growing under the surface, within the gel.

The crystals, pictured in Figure 4-16, appeared within a millimetre below the surface and formed crusts.

This effect limited the applicability of ZnOAc as a doping agent as it means that extended exposure to a medium with a lower zinc acetate concentration will cause the formation of crystals, which can then obstruct the acoustic beam. Additionally, producing measurements or characterizations within solutions of ZnOAc would mean that numerous corrections should be applied to account for the change in attenuation, since the attenuation of water is negligible in any lab measurement, and would also pose a risk to any piece of equipment submerged in the solution due to the presence of the salt's ions which could corrode metallic elements and cause salt deposits on any exposed surfaces.

A solution would be to make use of zinc acetate in sealed phantoms, such as the CIRS phantoms, which are encased in closed containers and to use plastic membranes to isolate the contents of the phantom from their environments.

For these reasons it was decided to abandon the use of zinc acetate for the rest of the project.

4.1.3 Silicon oxide as a doping agent

Gellan gum-based materials with different concentrations of silicon oxide were also characterised.

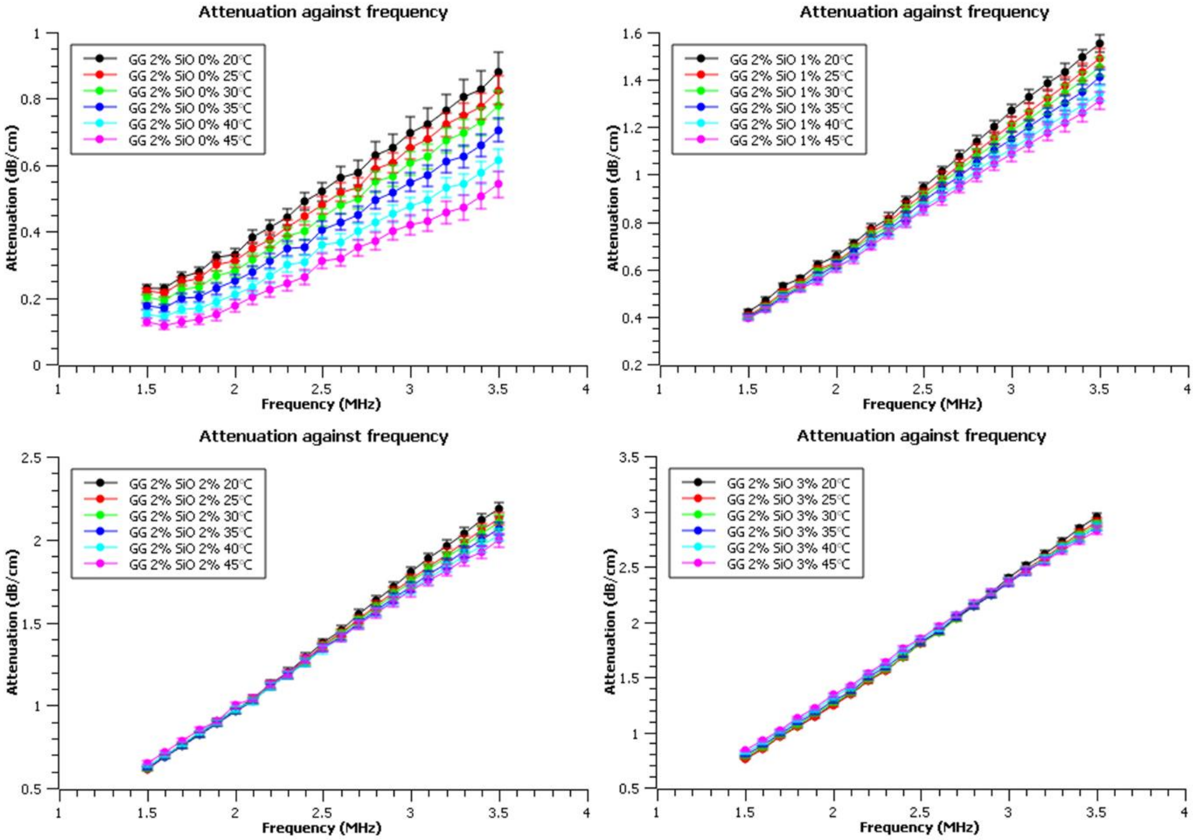

Figure 4-17: Attenuation of 2% gellan gum samples with different SiO concentrations as a function of frequency at different temperatures (20 to 45 at 5 intervals). Top left, 0%. Top Right,1%. Bottom left, 2%. Bottom right, 3%.

Fit parameters for attenuation at 20°C for 2% gellan gum and variable SiO				
SiO %	0	1	2	3
α_0	0.112±0.011	0.228±0.023	0.342±0.034	0.410±0.041
n	1.65±0.03	1.55±0.02	1.50±0.02	1.60±0.01

Table 4-9: Fit parameters for 2% gellan gum samples with different SiO concentrations at 20°C.

For 2% gellan gum samples containing SiO it can be seen in Table 4-9 that the presence of the scatterer increases attenuation and reduces the attenuation change with temperature. At 3% the attenuation varies little with temperature.

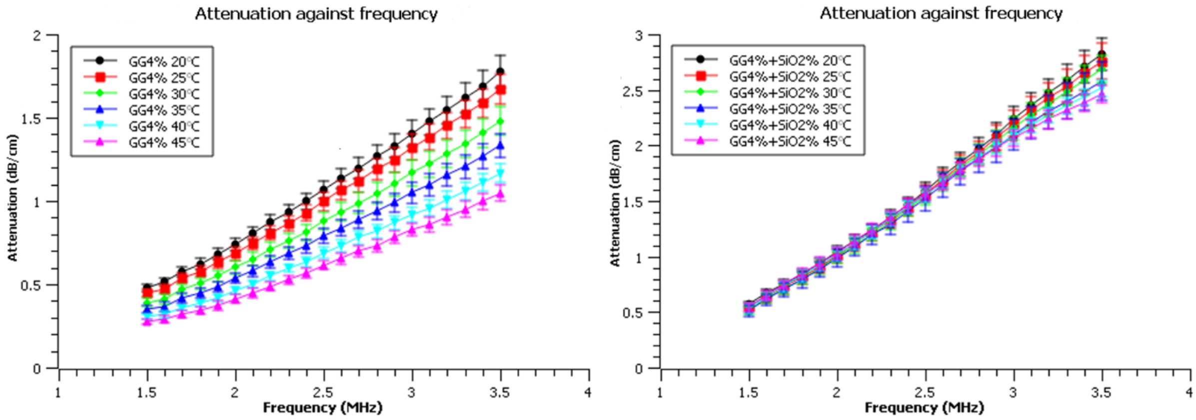

Figure 4-18:Comparison of the attenuation of 4% gellan gum samples without SiO (left) and with 2% SiO (right).

Fit parameters for attenuation at 20°C for 4% gellan gum and variable SiO		
SiO %	0	2
α_0	0.255±0.026	0.298±0.030
n	1.55±0.02	1.81+-0.02

Table 4-10: Fit parameters for 4% gellan gum with and without 2% SiO at 20°C.

As Figure 4-18 shows, 4% gellan gum concentration exhibits the same behaviour. Here, the addition of 2% SiO produces a similar effect for both 2% and 4% concentrations, where the variation of attenuation with temperature between 20 and 45°C becomes indistinguishable within uncertainties, up to a frequency of approximately 2.7MHz. The comparison between the 20 and the 45°C datasets scores higher than 0.9 up to 2.5 MHz, where the relative difference is less than 1%. The p value starts decreasing, reaching 0.53 at 2.7 MHz, where the relative difference becomes 4%. The p value reaches below 0.05 at 3.5 MHz where it becomes 0.03 and the relative difference becomes 13%.

Under a first order assumption, the attenuation of the gellan gum and silicon oxide mixtures would be the simple addition of their respective contributions. This would mean that the attenuation produced by silicon oxide increases with temperature. This is further confirmed with the increased echogenicity that thermal lesions show under ultrasound imaging of these phantoms.

The addition of SiO also results in an increased stiffness of the samples.

Speed of sound for the samples with and without SiO was also measured. As can be seen in Figure 4-19 the addition of silicon oxide has little to no effect on the SoS of gellan gum samples.

It would be expected that the addition of silicon oxide to gellan gum samples would only affect its attenuation and scatter, but not the speed of sound of the material, despite a change in the perceived firmness of the material when being handled (for GG2% and GG2%+SiO3% $p = 0.67$).

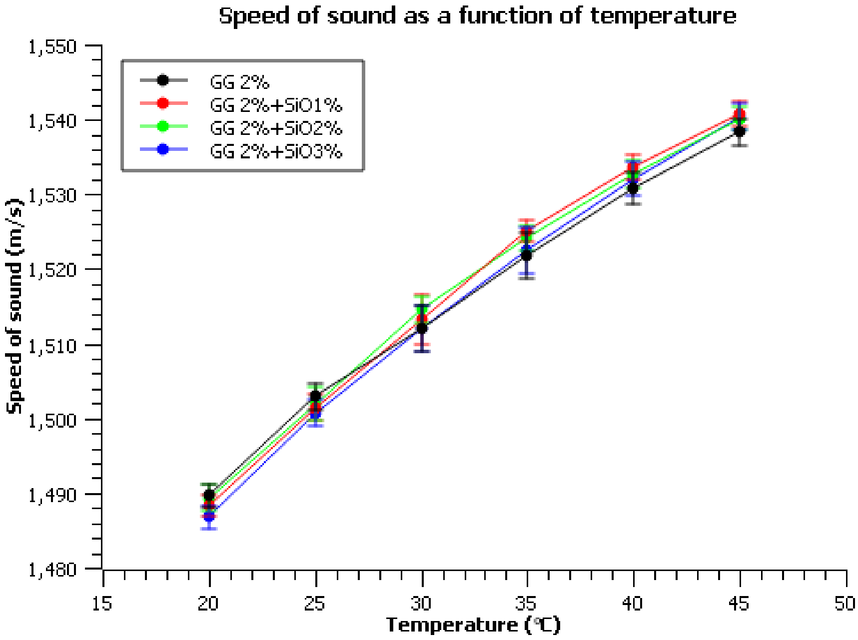

Figure 4-19: Speed of sound of 2% gellan gum samples with increasing SiO concentrations as a function of temperature.

4.1.4 M-60-NB dye as a doping agent

The addition of 5% in weight M-60-NB dye to 2% gellan gum samples was found to decrease their robustness, making them harder to handle. In order to compensate for this effect, 4% +2% SiO samples were used.

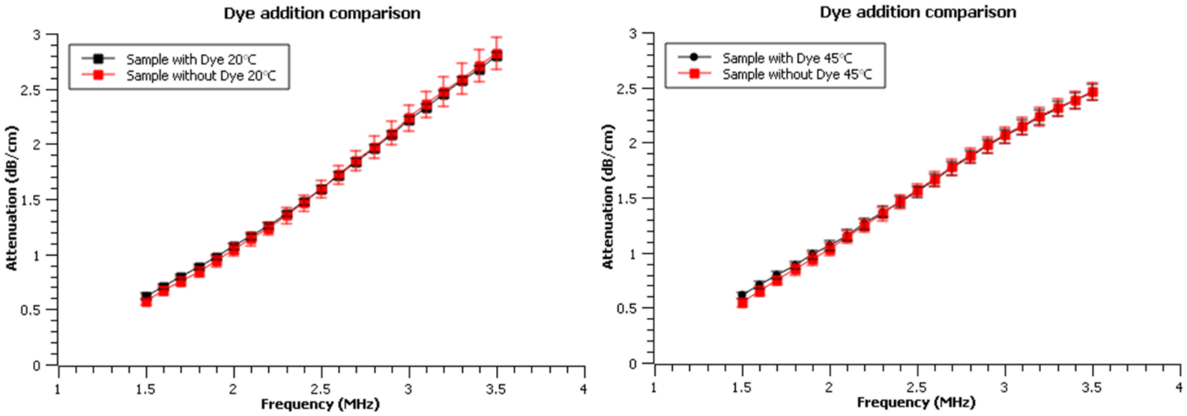

Figure 4-20: Comparison of the attenuation of 4% gellan gum 2% SiO samples with and without the dye. Left, at 20℃. Right, at 45℃.

As can be seen in Figure 4-20, the addition of the dye resulted in a statistically insignificant change in attenuation in the samples ($p_{20} = 0.87, p_{45} = 0.76$).

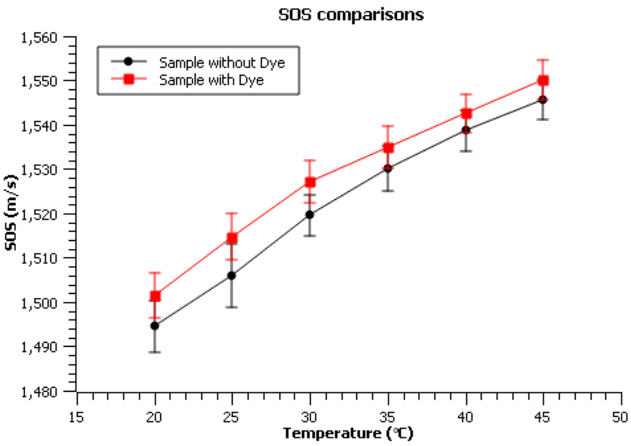

Figure 4-21: Comparison of the SoS of 4% gellan gum 2% SiO samples with and without the dye for the 20 to 45°C range.

While the addition of the dye can be seen to result in a net increase in the SOS of the samples, the difference is negligible ranging from 0.4% at 20 °C to 0.3% at 45 °C ($p = 0.41$).

4.2 Characterization of the dye

Samples were photographed at increasing temperatures in order to identify the temperature at which colour change occurs.

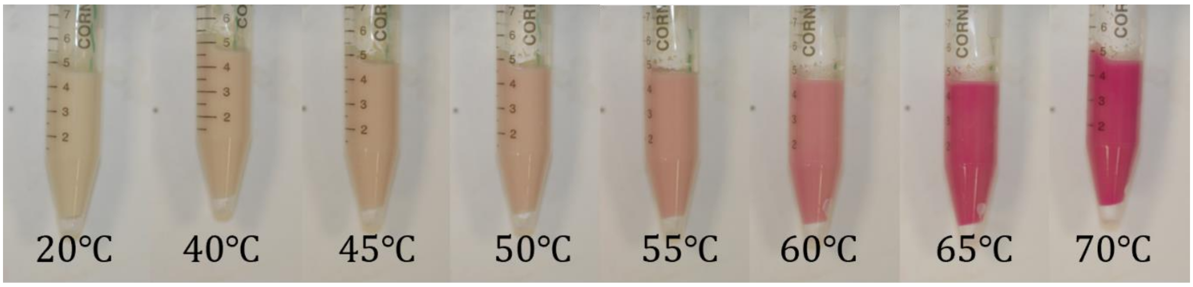

Figure 4-22: Colour gradient obtained from samples with the MB-60 dye at temperatures in the range 20-70ºC.

The colour of the samples was then analysed from the photographs to obtain the values of the RGB channels to characterize the colour change. In order to do so, samples were photographed under controlled lighting in a fixed position. The images obtained were then loaded into MATLAB and the colour of the gel was analysed. As can be seen in Figure 4-23 the change in colour manifests itself as a drop in the average values of the blue and green channels while the red channel barely changes.

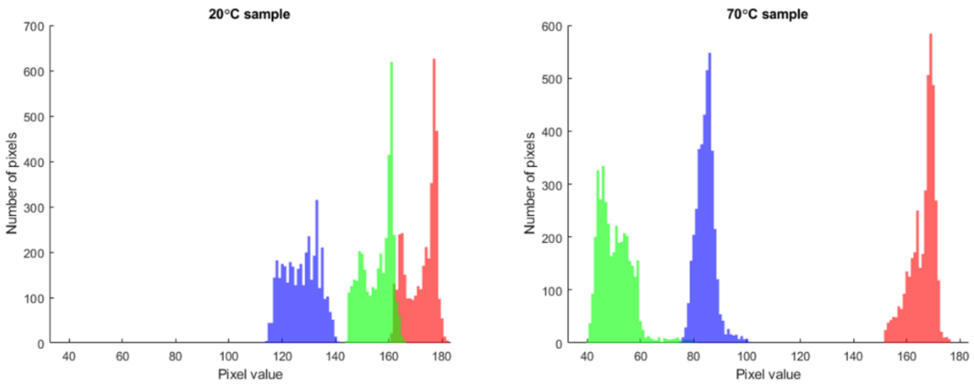

Figure 4-23: Histograms of the pixel values of the samples separated into their corresponding colours for 20 and 70°C.

Calculating the average and standard deviation of the values produces Table 4-11, in which it becomes much clearer that the average red intensity presents the smallest change and that the green channel experienced the biggest change in intensity.

	Red channel	Green channel	Blue channel
Cold sample (Room Temperature)	172±6	156±6	127±6
Heated sample (70°C)	166±5	51±6	85±4

Table 4-11: Average pixel values for the RGB channels of the sample pre and post heating.

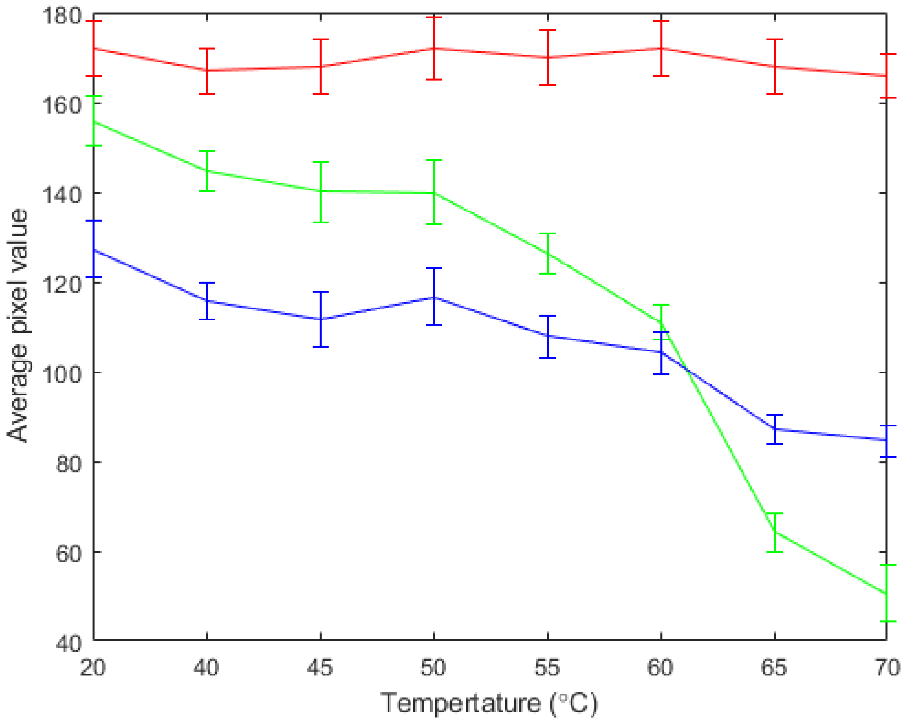

Figure 4-24: Evolution of the average values of the RGB channels with temperature.

Figure 4-24 shows the mean and standard deviations of the channels with temperature. The error bars represent one standard deviation. The red channel is unchanging. The biggest change in colour occurs in the green channel in the 60 to 65°C temperature range.

Since these samples were photographed under very controlled conditions, the results from the characterization cannot easily be extrapolated into quantitative calibration of the temperature based on the colour of the images, as lighting conditions are bound to alter the results. That kind of quantitative analysis could only be achieved if the images of the samples were to be acquired with the use of a scanner or a system that removes variability between aquisitions. However, the results of this analysis show that within a single photograph, the colour change should be able to indicate the regions where heating was maximum. It also indicates that the colour change may be detectable at temperatures as low as 50°C and that the biggest rate of colour change is reached at the 60-65°C interval.

4.3 Effects of irradiation

Different samples were compared post and pre irradiation in order to assess the effect of irradiation on the integrity of the gels. While the effect of irradiation on PVA gels has been studied in the past to assess the effects on gelation and some mechanical properties[67,78,88], the effect on acoustic properties has never been investigated.

Initially, the effect of irradiation on a 2% Gellan gum sample was evaluated. As can be seen, in Figure 4-25 the exposure to irradiation of the samples up to 3kGy causes little to no effect ($p = 0.53$). Considering that the changes in mechanical properties that had been observed at doses several orders of magnitude higher (50, 100 and 150 kGy)[78], the apparent lack of an effect could be due to the difference in dose. The results are satisfactory since the dose that was tested is significantly greater than that which a phantom would receive during its expected usable life.

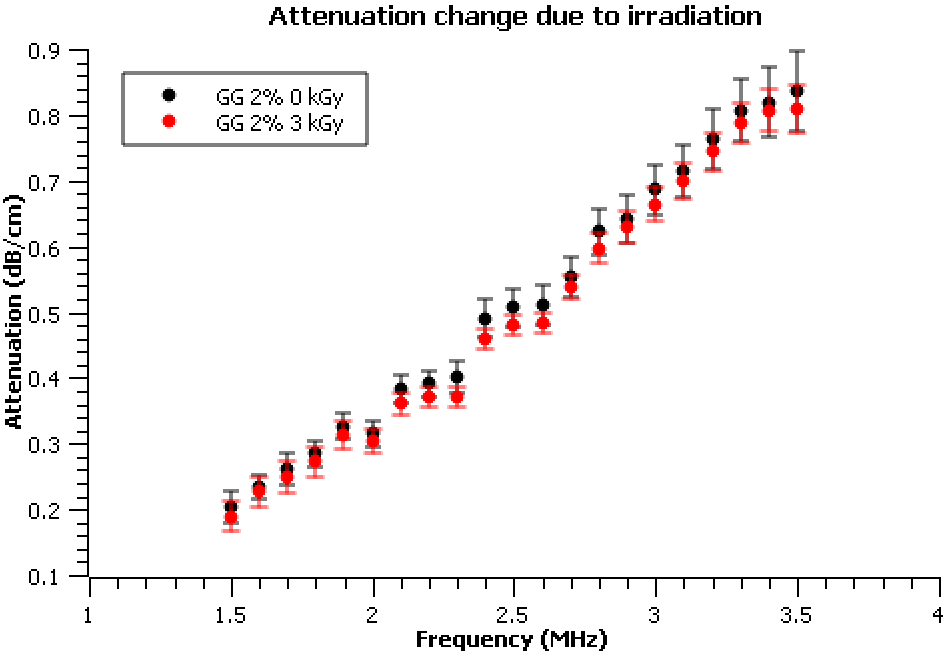

Figure 4-25. Comparison of the attenuation of 2% gellan gum of samples pre and post 3kGy irradiation.

The effect of irradiation on 4% gellan gum, 2% SiO, and 5% MB-60 samples was also analysed, as this information is not available in literature.

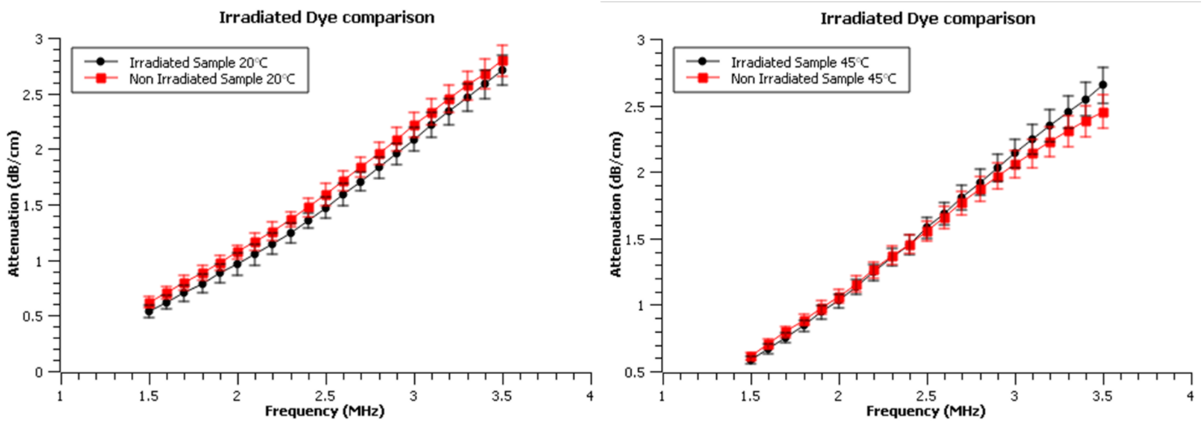

Figure 4-26: Comparison of the attenuation of thermochromic samples pre and post irradiation.

As can be seen in Figure 4-26, there is a consistent overlap in the attenuation of the thermochromic samples pre and post irradiation indicating that there is a minimum effect of the ionizing radiation on samples which include the dye ($p_{20} = 0.39, p_{45} = 0.57$).

The colour change of samples under ionizing radiation was also evaluated. Figure 4-27 shows a sample after 3kGy exposure next to an unexposed sample. The sample was exposed over a period of 48 hours at a low rate. Samples were collected and examined several hours after exposure and thus, any transient effects would not have been identified.

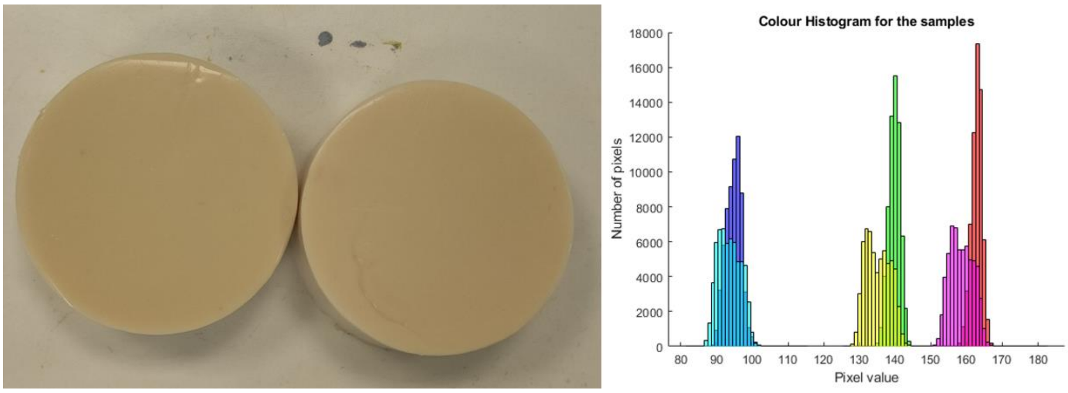

Figure 4-27: Left, picture of an irradiated (3kGy, left) and an unirradiated (0kGy, right) sample. No colour change is apparent. Right, corresponding histograms for the pixel values of the irradiated sample (red, green, and blue) and the unirradiated sample (magenta, yellow and cyan matching the RGB pattern).

There is no apparent difference in colour and the corresponding histograms reveal a wide overlap with slight differences in the colour distributions ($p = 0.40$).

In order to test for the presence of transient effects, a single sample was cut in half and exposed at a rate of 10Gy/min for a minute. The sample showed no apparent colour change due to this intense exposure. The corresponding histograms overlap at every channel and show a slight drift which seems to be mostly due a gradient in lighting across the sample, the top half being slightly brighter ($p = 0.10$).

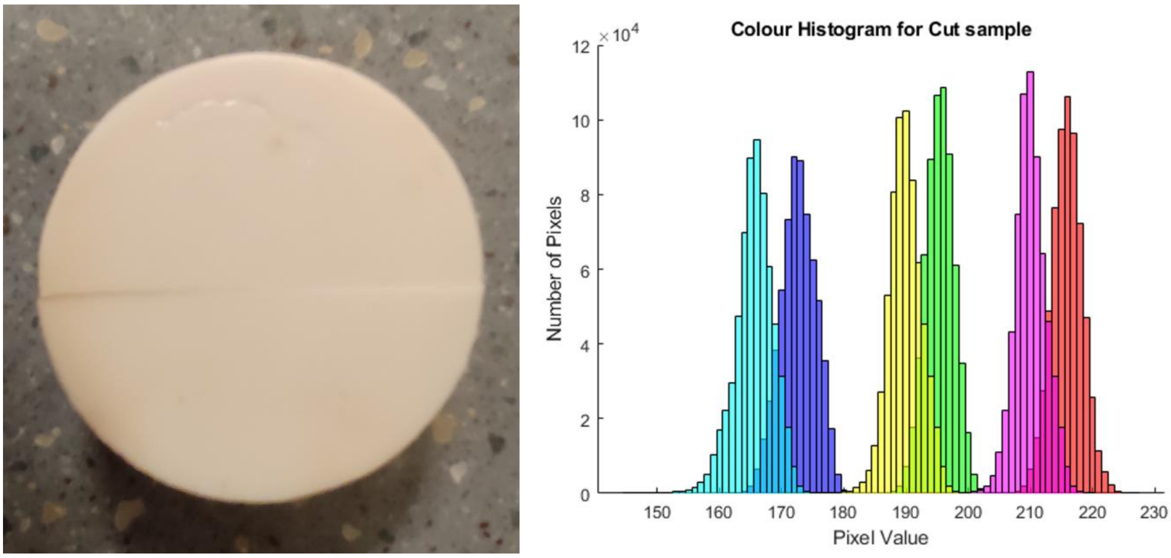

Figure 4-28: Left, single sample for the test of transient effects. The top half was exposed to a total of 10 Gy and the bottom half was unexposed. Right, the corresponding colour histograms in RGB for the irradiated half and in cyan yellow and magenta (matching the RGB pattern) for the unexposed half.

4.4 Results of density measurements

The density of samples was measured (n=3).

Sample	Density (kg/m^3)
2% Gellan gum	1000.6 ± 1.1
4% Gellan gum	1009.3 ± 0.9
4% GG+2% SiO	1043.5 ± 1.8
4% GG+2% SiO + 5% MB-60 Dye	1051.3 ± 3.7

Table 4-12. Density of different gellan gum based samples.

As expected, the density of the samples rose with increasing gellan gum concentration. The addition of SiO further increased the density. The value of the density is comparable to that given by the ICRU-44{89} for soft tissues and blood (1060 kg/m3), ovaries and skeletal muscle (1050kg/m3) and for testicles (1040 kg/m3).

4.5 Thermal properties

Thermal properties were measured for various samples. Three samples at each concentration were measured.

Sample	Thermal Conductivity (W/mK)	Thermal Diffusivity (mm^2/s)	Volumetric heat capacity (MJ/m^{3}K)
2% Gellan gum	0.610 ± 0.004	0.176 ± 0.003	3.46 ± 0.04
4% Gellan gum	0.616 ± 0.008	0.158 ± 0.007	3.86 ± 0.13
4% GG+2% SiO	0.668 ± 0.201	0.179 ± 0.055	3.74 ± 1.13
4% GG+2% SiO + 5% MB-60 Dye	0.650 ± 0.012	0.172 ± 0.006	3.79 ± 0.09

Table 4-13: Thermal properties of 2 and 4% gellan gum samples.

The melting point for 4% gellan gum 2% SiO with and without dye was also measured.

Sample	Melting Point (°C)

4% GG+2% SiO	100 ± 1
4% GG+2% SiO + 5% MB-60 Dye	86 ± 1

Table 4-14: Melting points of 4% gellan gum 2% SiO samples with and without the MB-60 dye.

The addition of SiO produced an increase in the thermal conductivity and diffusivity as well as a slight reduction in the volumetric heat capacity. More notably, the addition of the dye does not produce significant changes in the thermal properties ($p_{TC} = 0.93, p_{TD} = 0.90$ and $p_{HC} = 0.96$), except for the melting point.

Considering that the melting point of the gel without the dye is the same as the boiling point of water, which is the liquid entrapped in the polysaccharide matrix, it suggests that water-dye mixture has a lower boiling point that induces the melting. This could be by the sudden expansion of the liquid, breaking the hydrogen bonds withing the polysaccharide structure. Additionally, it should be noted that the melting of the mixture without the dye was mixture of melting and boiling of the material contrasted by a more regular melting in the samples with the dye. This could be related to the first attempts at adding the dye, which resulted in a softening of the samples, which was then compensated by adding the SiO for consistency. The presence of the dye may affect the quality or quantity of hydrogen bonds, therefore facilitating their rupture at lower temperatures. Additionally, this could be driven by the water-dye mixture having a lower boiling point, although this was not measured.

The melting point of other samples was not measured, as they were never used in the construction of the phantoms and so it was not of interest.

4.6 Radiological properties

CT scans of the samples returned the Hounsfield unit values for 4% gellan gum, 2% SiO samples with and without the thermochromic dye.

Sample	CT number (HU)
4% GG+2% SiO	62 ± 11
4% GG+2% SiO + 5% MB-60 Dye	65 ± 12

Table 4-15: Hounsfield units of the 4% gellan gum 2% SiO samples with and without the MB-60 dye.

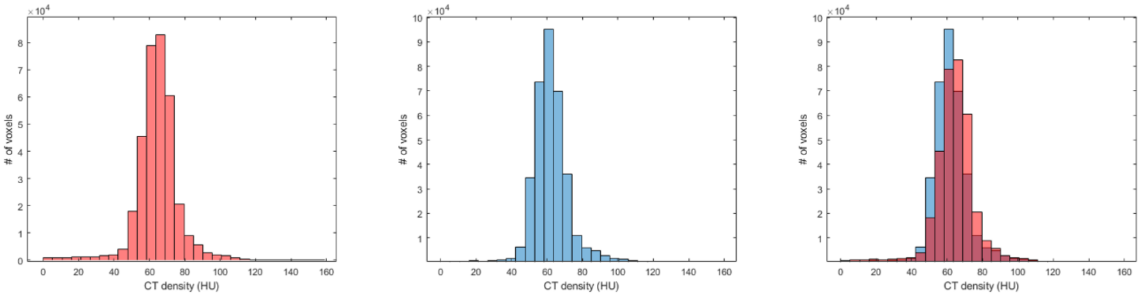

Figure 4-29: Histograms of the HU values derived from CT scans of the 4% gellan gum 2% SiO samples. Left, with the thermochromic dye. Centre, without the thermochromic dye. Right, both histograms superimposed.

As can be seen, the histograms for both HU distributions overlap. While the thermochromic mixture gives slightly higher values of CT density, which might be attributable to the presence of the dye, this difference is not statistically significant ($p = 0.85$).

Calculations of the absorbed dose gave values of 0.780 cGy/MU for the gel with the thermochromic dye and 0.777 cGy/MU for the gel without the dye.

Measurements of the attenuation with the ionisation chamber recorded 35.31 and 35.24 nC for the measurement in 10 cm of solid water after receiving 200 MU (Monitor Units). Along with the Linac calibration of 0.812 cGY/MU this results in a calibration factor of 4.604 cGy/nC for the ionization chamber.

Measurements of the attenuation for the gel doped with thermochromic dye returned 34.15 nC twice and measurement for the gel without the dye returned 34.16 and 34.17. Multiplying these values by the ionisation chamber calibration and dividing by the 200 MUthe resulting absorbed doseis 0.786 cGy/MU.

Sample	Simulated absorbed dose (cGY/MU)	Measured absorbed dose (cGY/MU)
4% GG+2% SiO	0.777	0.786
4% GG+2% SiO + 5% MB-60 Dye	0.780	0.786

Table 4-16: Comparison of attenuation measurements and calculations for 4% gellan gum 2% SiO samples with and without the MB-60 dye.

The agreement in the values obtained from the simulation and the measurements, indicate that the effective atomic number of the material is similar to that of human tissues. As explained in section 3.5, the energy for the CT scan were 120keV, whereas the energies for measurement and simulation of absorbed dose were 6MeV. As explained in section 2.2.1 the difference in energies could result in a different prevalence of the physical phenomena involved in the radiation-matter interactions occurring in the gel. Treatment planning systems are designed accurately simulate the results of treatments using MeV energies from the information obtained from CT scans acquired at hundreds of keV. The agreement between the simulated and measured absorbed doses indicates that our gels are presenting the same behaviour as human tissues would have. This is only possible if the effective atomic number for the gels is similar to the effective atomic number of tissues, as differences in Z would result in a different prevalence of the photoelectric, Compton and pair production effects. This means that profiles produced from the treatment planning system can thus be considered predictive of the usability of the phantom and that it is a good TMM for radiation applications.

PDD profiles and transversal profiles were also produced using the treatment planning system. While these profiles are not themselves relevant, since most of the information that can be extracted from them is information about the specific beam being used, it is still good that they can be produced and that they show the normal features of these types of beams on the phantoms shown in Figure 2-2.

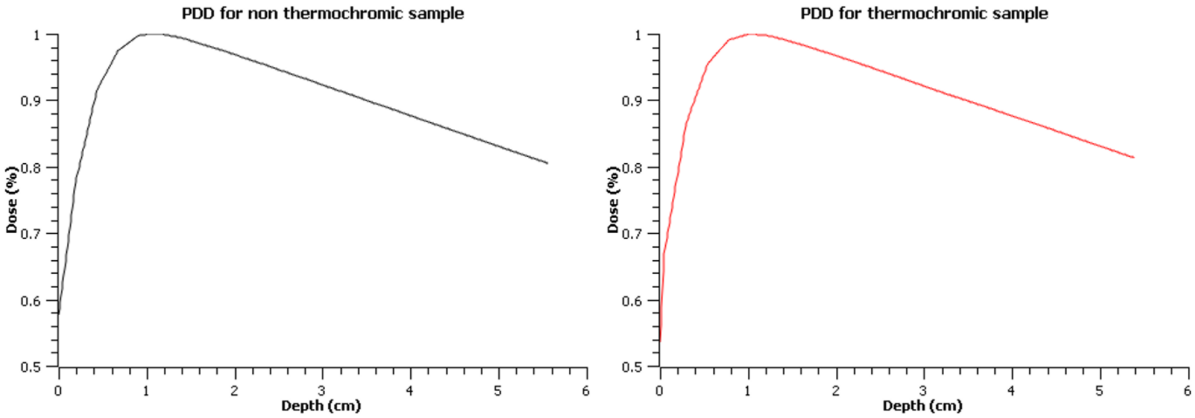

Figure 4-30: Percentage Depth Dose for the non-thermochromic (Left) and thermochromic (right) samples

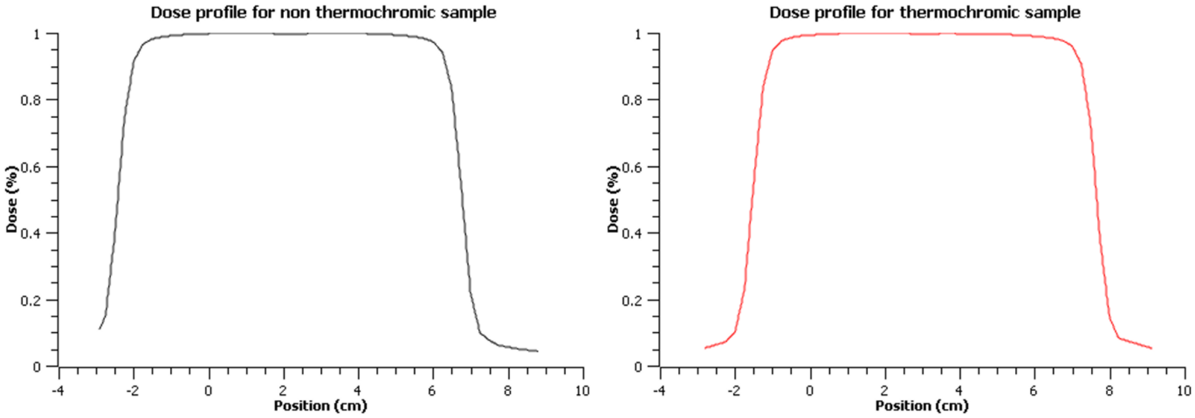

Figure 4-31:Dose profiles for the non-thermochromic (Left) and thermochromic (right) samples

Figure 4-30 and Figure 4-31 show the corresponding profiles obtained from the samples. For both samples there is an observable surface dose, which steadily increases over the build-up region until the 1 cm of depth decrease afterwards. The dose profiles show a flat beam with a narrow penumbra at the side where the dose drops off.

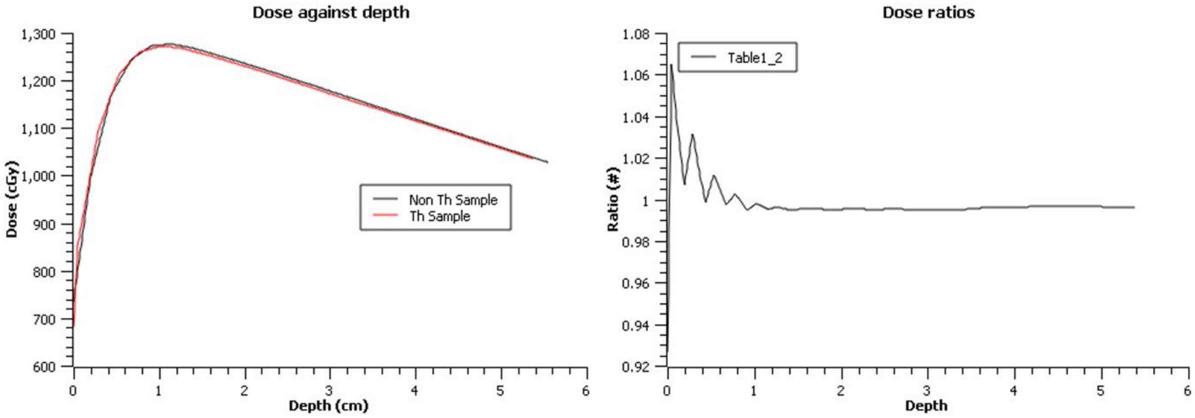

Figure 4-32: Left, the depth dose profiles for both samples superimposed. Right, the ratio of the dose values at each point.

The comparison of the dose values (Figure 4-32) shows good agreement and when comparing the ratios of their values we see a maximum difference of 7% in the region where the lines present the biggest gradient, and where a small offset can cause big differences in the ratios. The fact that the beams used were identical and that the resulting dose profiles agree to such an extent is a consequence of the close similarity in HU previously shown, which makes the materials indistinguishable for radiation applications.

4.7 Summary

The materials selected for the phantoms described in the following section are 4% gellan gum, 2% SiO samples. There is a non-thermochromic variation with 96% water and a thermochromic variation with 91% water 5% MB-60.

Typical values for soft tissues are:

Tissue	Thermal Conductivity (W/mK)	Thermal Diffusivity (mm^2/s)	Volumetric heat capacity (MJ/m^3K)
Skin	0.37±0.06	0.04–0.16	3.32±0.23
Muscle	0.49±0.04	0.16	3.26±0.44
Brain	0.51±0.02	0.13–0.14	3.49±0.07
Breast	0.21	0.14	2.30±0.36
Liver	0.52±0.03	0.14	3.34±0.11

Table 4-17. Typical thermal values for soft tissues[90].

Phantom material	Thermal Conductivity (W/mk)	Thermal Diffusivity (mm^2/s)	Volumetric heat capacity (MJ/m^3K)
Non-thermochromic	0.668 ± 0.201	0.179 ± 0.055	3.74 ± 1.13
Thermochromic	0.650 ± 0.012	0.172 ± 0.006	3.79 ± 0.09

Table 4-18: Thermal values for the proposed phantom materials.

It can be seen that the thermal properties of the proposed materials are comparable to the typical values of those of soft tissues.

Tissue	Speed of Sound	Attenuation coefficient (dB/cmMHz)	Acoustic impedance (MRayl)	Density (kg/m^3)
Soft tissue	1575	0.6-2.24	1.66	1055
Soft tissue fatty	1465	0.4	1.44	985
Muscle	1547	1.09	1.62	1920
Brain	1560	0.6	1.62	1050
Breast	1510	0.75	1.54	1040
Liver	1595	0.5	1.69	1020
Kidney	1560	1	1.64	1060
Prostate	1614	1.86	1.68	1050

Table 4-19: Typical acoustic parameters for soft tissues[90]

Phantom material	Speed of Sound (At 37°C)	Attenuation coefficient		Acoustic impedance (MRayl)	Density (kg/m^3)
		α_0(db/cmMHz^n)	n		
Non-thermochromic	1533.5±6.9	0.298±0.030	1.81+-0.02	1.6002±0.007	1043.5 ± 1.8
Thermochromic	1538.0±6.6			1.6168±0.009	1051.3 ± 3.7

Table 4-20: Acoustic parameters for the proposed phantom materials.

Since the literature data often does not indicate the temperature for these values, a temperature of 37°C is assumed, as it is a typical body temperature value.

The proposed materials are well matched to the SoS, density and consequently the acoustic impedance of the potential target tissues. This is desirable, as US equipment is designed to operate on human tissues. If there was a significant difference between the acoustic impedance TMM and that of tissues, this would result in large reflections that could prevent the US from propagating into the material which would make it useless. Additionally, having a SoS that matches tissues is beneficial, as most imaging modalities rely on an assumed SoS to perform measurements of length. This means that the phantom is suited for applications relying on or testing targeting, positioning and measurements of length along the path of the acoustic beam.

. It should be noted that the way that the data is reported suggests that the attenuation scales linearly with frequency although that is not always true[3]. Without information about the frequency scaling of the attenuation it is hard to draw comparisons. However, the values reported tend to be those for attenuation at 1MHz. The attenuation at this frequency would be slightly lower for the phantom materials. Considering that most HIFU treatments are performed in the frequency range from 1 to 2.5 MHz, the proposed materials are likely to attenuate less than soft tissues. However, the current attenuation was reached solely through the addition of SiO. The amount added was determined by the need to compensate for the effect of the addition of the thermochromic dye and it could further be increased if higher attenuation values were desired or needed. This increase in attenuation would be mostly due to an increase in scatter and while the addition of scatterers can make slight contributions to absorption it is not the main effect. It was later found that the current attenuation levels allowed us to test our equipment at power conditions that would not risk damaging the systems. The combined effect of the reduced attenuation and increased heat capacity suggests that the power needed to produce a given temperature increase in the phantom will be higher than the power required to produce the same effect in soft tissues. The increased diffusivity and conductivity are likely to further compound this effect. On the other hand, the comparatively low value of attenuation would be advantageous in applications that need to evaluate imaging, as this will enable the imaging to reach further into the material before being attenuated and no longer returning information.

The attenuation of pure gellan gum samples was found to decrease with increasing temperatures and it was found that the addition of SiO reduced the magnitude of this effect. This is similar to the findings of Bamber and Hill[91], who found that the attenuation of human liver samples decreased with temperature for frequencies from 2 to 7 MHz, and the work of Gamell Croissette and Heyser[92], who found similar effects for frequencies from 1.5 to 10 MHz. Similarly, the speed of sound of our samples increases with temperature, as Bamber and Hill found for human liver[91].

The effect of SiO on the temperature dependence of attenuation could be very valuable in applications where no change is desired. Some of the more simplistic computer simulations are not able to implement such changes in their processes and having a phantom that does not change its attenuation would allow for a direct comparison of such simulations to experimental data. While the selected TMM samples still present some variability with temperature, these include 2% SiO, but more could be included to further remove these effects as it was found with 2% gellan gum samples.

Tissue	CT number (HU)
Adipose	-95 to -55, -95 ± 10
Breast	-61 ± 47
Heart	25 ± 25
Brain	20 to 40, 28 ± 19
Spleen	54
Liver	58 ± 9.63
Prostate	34, 45 ± 4
Kidney	35 ± 14, 43
Muscle	$40\ to\ 44$, 60 ± 30, 54 ± 7

Fat	−80 ± 20, 90

Table 4-21: Reported CT numbers for soft tissues[90].

Phantom material	CT number (HU)
Non-thermochromic	62 ± 11
Thermochromic	65 ± 12

Table 4-22: CT numbers for the proposed phantom materials.

The reported CT numbers shown in Table 4-21 highlight the variability of the measured Hounsfield Units with the energy of the beam. While the values of the measured CT numbers in the phantom will depend on the energy of the beam[90], the measured values are slightly above most tissues, closer to some reported values of muscle and liver.

The phantom material should also be usable for radiotherapy applications, as demonstrated by the agreement between measured and calculated dose reported in section 4.6. The CT numbers suggest that it should be applicable too for some measurements. More importantly, the relative uncertainty measured is at the lower end of the available spectrum of the reported values, and so results obtained when using this phantom material should be reproducible. The resistance of the materials to radiation doses also further validates this assessment.

5 Chapter 5 QA Phantom design and testing

5.1 TTTS and the TTTS-HIFU system

Twin-to-twin transfusion syndrome (TTTS) is a condition that occurs in monochorionic twin pregnancies, in which placental vascular anastomoses (blood vessels) that connect the blood supplies of the twins, form and produce a blood flow imbalance. TTTS can lead to an insufficient blood supply in the donor foetus, often resulting in death which subsequently puts the other foetus and the parent at risk of many complications and even death.

The ICR has designed a TTTS-HIFU system to treat this syndrome with thermal ablation. After a prior scan which identifies the number of anastomoses which need to be treated, the system locates the interconnecting blood vessels, and delivers HIFU in order to produce vascular occlusion, stopping the unwanted blood flow.

The TTTS-HIFU system provides HIFU therapy guided by B-mode ultrasound imaging, with doppler imaging capabilities. It consists of a H-175 annular transducer (Sonic Concepts, Inc. Washington, USA). The outer diameter is 99.40 mm, and the inner diameter 44.23 mm. It has a radius of curvature of 89 mm and a resonance frequency of 1.66 MHz. The transducer is composed of four elements, where all elements are annular rings of equal surface area. Each element is connected to its own impedance matching box and a 22B wattmeter (Sonic Concepts). The wattmeters are monitored and logged using a Raspberry Pi 4 (Raspberry Pi Foundation, Cambridge, United Kingdom). The transducer is driven by a TPO102 (Sonic Concepts) 4-channel signal generator and amplifier. The transducer is mounted on a UR5e robot arm (Universal Robots, Denmark). Images are acquired in real time using a Canon Aplio i900 ultrasound system (Canon Medical Systems USA, Inc. California, USA), equipped with a PVT382BT probe. The imaging probe is coaxially aligned to the therapy transducer and is inserted in the 44.23 mm hole at its centre. The system uses a MATLAB (Math-Works, Natick, Massachusetts, USA) program that controls the US imaging, the control of the robotic arm and the TPO signal generator in order to produce the exposures that target the blood vessels.

The MATLAB function unifies all the different elements into a single tool. It extracts the image from the Aplio system, obtaining all the relevant variables of the scale and depth, and controls the robot arm, controlling its movement using up to three different reference systems that can be both redefined and swapped at any point. It also controls the TPO102 for the exposures and reads the wattmeter measurements which are saved for inspection. The system offers the possibility of placing exposures in a line, selecting the number of exposures and the spacing between them. The duration of the exposures and the cool down period between them can also be controlled. The power can be manually selected, and the system calculates the focal intensity based on user input that provides thicknesses of different tissues, assuming their attenuation. The program includes a series of overlays that show the path of the therapeutic beam as well as intensity profiles from the combination of the exposures. Additionally, the program allows the screen to be recorded while all the operations take place. The recorded images can then be used to review the process.

The robot arm offers 6 degrees of freedom, 3 for movement in space and rotations along 3 perpendicular axes. The movement can be in steps as small as 0.1 mm and the rotations in steps of 0.1 degrees. As a safety measure the system is limited to movement steps of 10 mm with any move larger than providing a warning and requiring the user authorisation. The system can also allow free-hand movement, where an operator manually moves the robot arm without the use of the UI (User Interface), and free-hand rotation, in which the position of the transducer head is fixed, but manual rotation along the axis of the focus is enabled. The imaging system provides planar B-mode imaging as well as doppler or colour imaging.

5.2 The applicability of the thermochromic TMM to QA

The main aim in the design of the QA system was to apply the thermochromic material to the assessment of the power output of the TTTS-HIFU system in order to identify variations in power output under fixed exposure conditions. This evaluation should be able to allow operators to correct by variating the exposure settings according to detected variations of power through the QA evaluation. Furthermore, the implementation of these types of QA assessments can allow to track the evolution of the behaviour of the system over time and establishing the point at which certain elements may need replacement or repairs based on quantifiable data.

It is a well-known fact that the size of a lesion should increase with increasing power[57] and it was expected that the thermochromic material would be able to reflect these changes. An initial test was performed were a single thermochromic slice was exposed at increasing powers to make a qualitative assessment of the validity of this assumption.

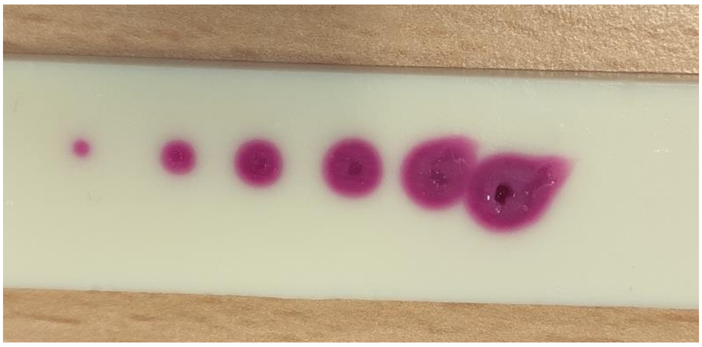

Figure 5-1. Qualitative test of the relationship between power and size of lesions under fixed exposure conditions.

As Figure 5-1 shows, the assumption that under fixed exposure conditions there was a relationship between size and power was verified. It was then decided to repeat these qualitative tests at fixed exposure conditions as a first assessment of the reproducibility of the lesions.

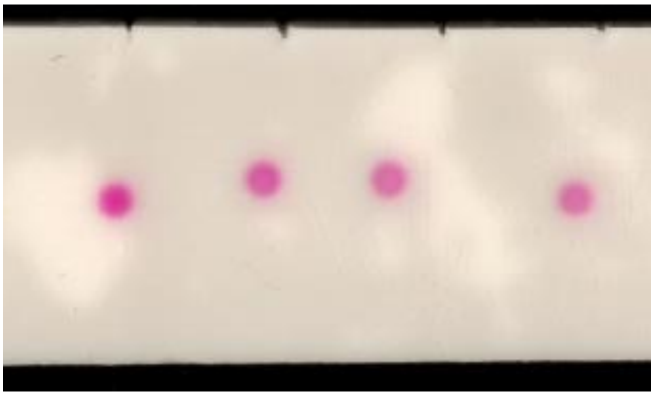

Figure 5-2. Qualitative test of the reproducibility of the lesions under fixed exposure conditions.

Figure 5-2 shows how the produced lesions were similar in size over the 4 repeated exposures.

As these tests had been a qualitative evaluation of the applicability of the phantom, these same principles had to be translated to the examination ad use of the TTTS-System, incorporating the samples into a phantom design

5.3 Phantom design

The phantom was designed with the intent of allowing QA measurements for assessment of the power output of the TTTS-HIFU system and of its targeting capabilities. Its design drew on that of radiotherapy phantoms, which often include a cavity that allows to slot an ionization chamber into the body of the phantom, which does not perform the measurement, and film dosimetry procedures using plastic water slabs. The resulting phantom was then designed to present separate measuring and non-measuring sections that could be stacked on top of each other to adapt to the needs of the measurement. An additional benefit of this modular design is the possibility of future expansion, the replacement of the measuring sections with different materials and or components and the alteration the thickness of the different sections to suit different exposure conditions.

The phantom (Figure 5-3) consists of four layers of gel in a stack. Each layer is a prism of square base with variable thicknesses along the path of the acoustic beam. The top and bottom layers are made of the non-thermochromic TMM described in section 4.7and have a thickness of 17 mm. The middle layers are composed of the thermochromic TMM (section 4.7). These each have a thickness of 6 mm. This was found to be sufficient to contain the cylindrical lesions (2mm in diameter 10 mm in height) produced under our test exposures with the TTTS-HIFU system

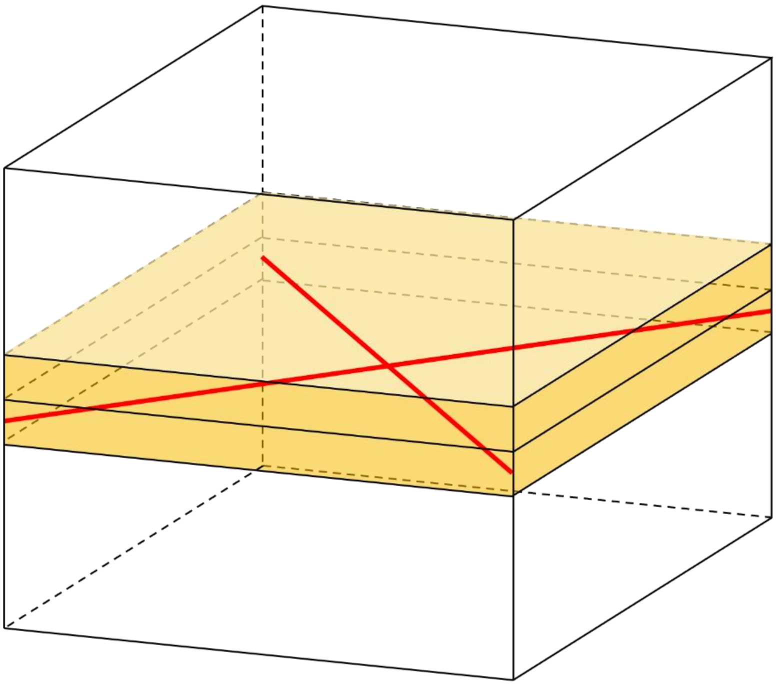

Figure 5-3. Schematic of the phantom. The top and bottom white layers are made of the non-thermochromic material, The middle yellow layers are made of the thermochromic material. The red lines represent two 25 μm wires used for alignment. These are embedded in the bottom thermochromic layer.

The two thermochromic layers are the targets for the purpose of the QA procedure. It was found advantageous to have two layers rather than one thicker one so that the inspection of the lesions could be direct, without involving cutting the phantom. The appearance of lesion at the interface between the layers is circular in each.

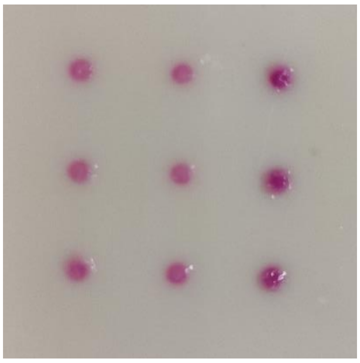

Figure 5-4: Appearance of the lesions on the thermochromic samples

Each of the layers is encased in a 3D-printed case in which it is cast. The size of the square, 74x74 mm^2, was chosen so that when performing QA, 9 different exposures could be made in a 3x3 grid with a 10 mm separation between each of the points. Due to the geometry of the therapeutic beam, the edges of the phantom had to be extended to prevent the casing from obstructing the beam. During casting, removable methacrylate windows seal the case.

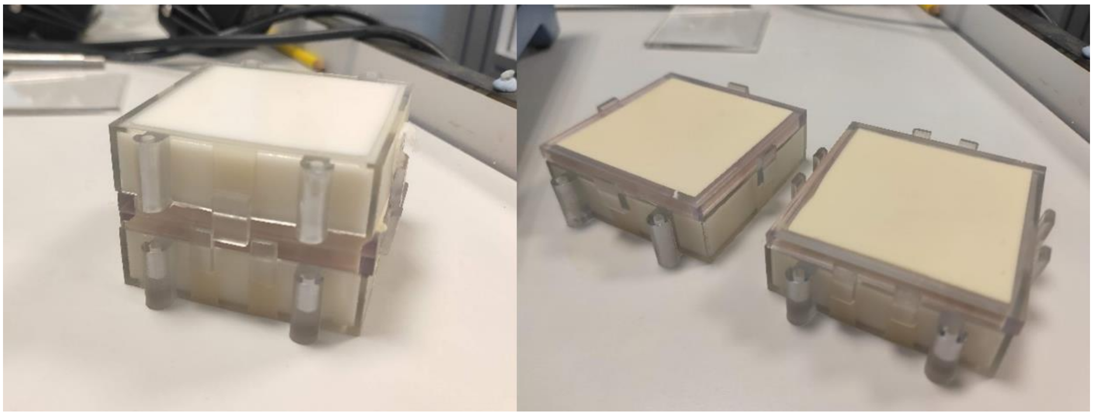

Figure 5-5. The 4-layered phantom. Left, the four layers stacked onto each other. Right, the phantom split in half, showing the central surfaces of the phantom.

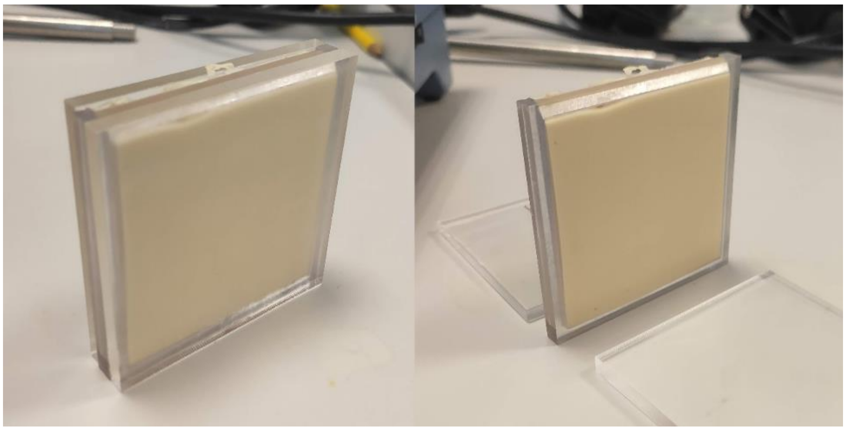

Figure 5-6. The thermochromic layer. Left, the layer in its mould after casting. Right, removal of the methacrylate sheets leaves the sample ready inside its casing.

The two outer layers provide a clinically relevant configuration, allow fixation and stabilisation of the position of the thermochromic layers, and allow the accumulation of heat, which might otherwise be diffused in coupling water through acoustic streaming. They also attenuate the ultrasound at the bottom of the phantom, reducing any possible reflections that could interfere with the measurement. These external layers are reusable and reduce the overall cost by minimising the amount of thermochromic dye needed to fill such a volume. In addition, the thermochromic samples, when stored immersed in water, tend to absorb water. This may be an effect of the presence of the thermochromic dye, which may produce an osmotic pressure by virtue of the chemical gradient of the dye within the sample and its environment. This absorption of water results in the gradual degradation of the gels, reducing their integrity and rigidity from that of rubber to the consistency of yoghurt. Sandwiching the thermochromic gels in their cases and the neighbouring non-thermochromic layers, minimizes their contact with water, preventing the loss of integrity of the samples.

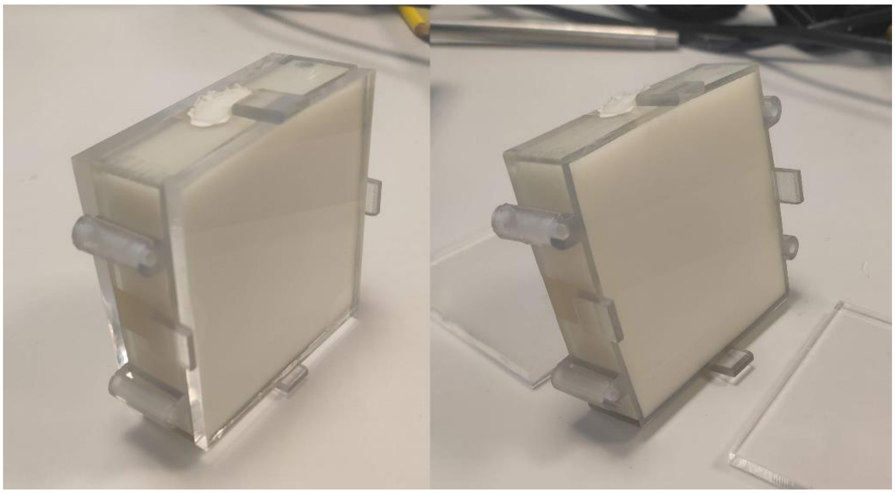

Figure 5-7: The non-thermochromic layer. Left, the layer in its mould after casting. Right, removal of the methacrylate sheets leaves the sample ready inside its casing.

Since the TTTS-system was guided by ultrasound, it was necessary to insert elements that could identify the centre of the phantom so that it could be used as a reference system. It was decided to use fine wires that would be visible under US imaging as insertions. The wires were embedded into the middle thermochromic samples so that they would be at a known fixed position within the phantom.

The imaging probe generates a 2D image in the direction of the beam propagation. A wire oriented perpendicular to the imaging plane would be seen as a point. When the wire is contained within the plane it will be seen as a line. No echoes will be visible if the wire and the imaging plane do not intersect. Schematics of these situations can be seen in Figure 5-8.

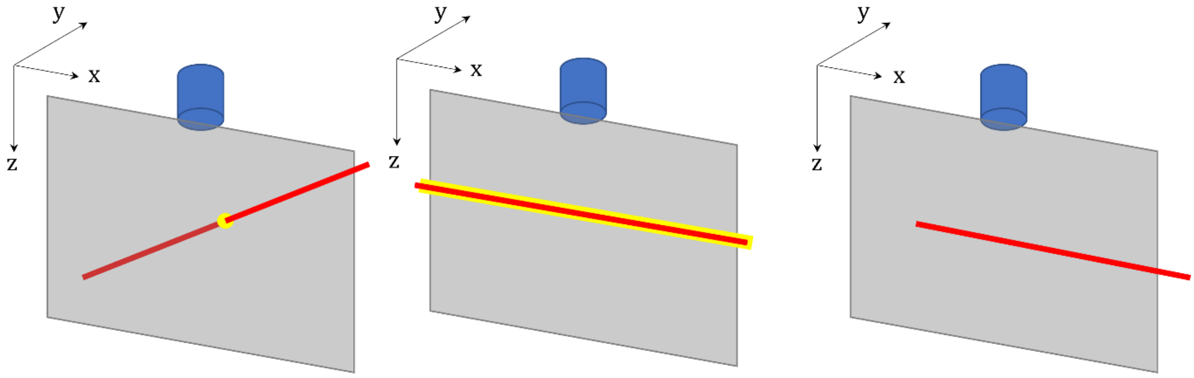

Figure 5-8. Schematics of the possible interaction of a line (in red) intersecting the imaging plane (in grey) from the imaging transducer (a blue cylinder for simplicity). Intersections are marked in yellow. The line can cut the plane at a specific point (Left), be contained within the plane (centre) or be parallel to it (right). The direction z is aligned with the direction of propagation of the imaging beam, x is contained within the plane and y is perpendicular to the plane.

25 µm manganin wires were used. This was the thinnest available that was visible under the ultrasound guiding system. Nylon wires were tested, but they were much thicker (0.7 mm), and their visibility was worse. The wires were placed in the post-focal region to avoid interference with the HIFU exposure.

5.3.1 Alignment setup and procedure

In the first design (Figure 5-9) the setup of the wires was a cross-like structure where a single thread along one direction intersected with three perpendicular wires to produce three points that were the intended target. This arrangement minimized the number of wires necessary to produce the intersections to identify the different points. However, it meant that at least one wire is parallel to the imaging plane, reducing its visibility almost to zero. To compensate for this, the imaging probe could have been used at an angle, but the robot arm defines its movement relative to the imaging plane (one direction being the perpendicular to the plane, another the axial direction of the imaging probe and the last as perpendicular to the other two, parallel to the plan), which made this alignment impractical.

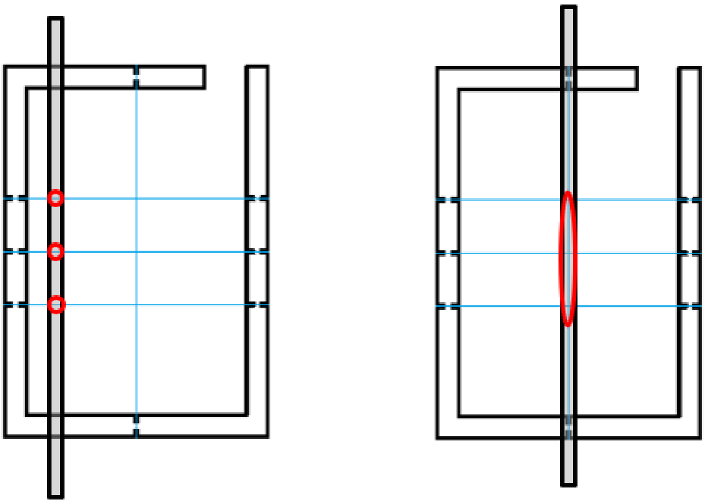

Figure 5-9: Diagram of the initial setup of wires. This arrangement uses 4 different wires to produce 3 intersections that are the targets for the exposures. The grey rectangles represent the US imaging plane, and the red circles highlight the intersections of the manganin wires and the imaging plane. As can be seen on the right, the movement of the imaging plane along the cardinal direction would not allow identification of the coplanar wire.

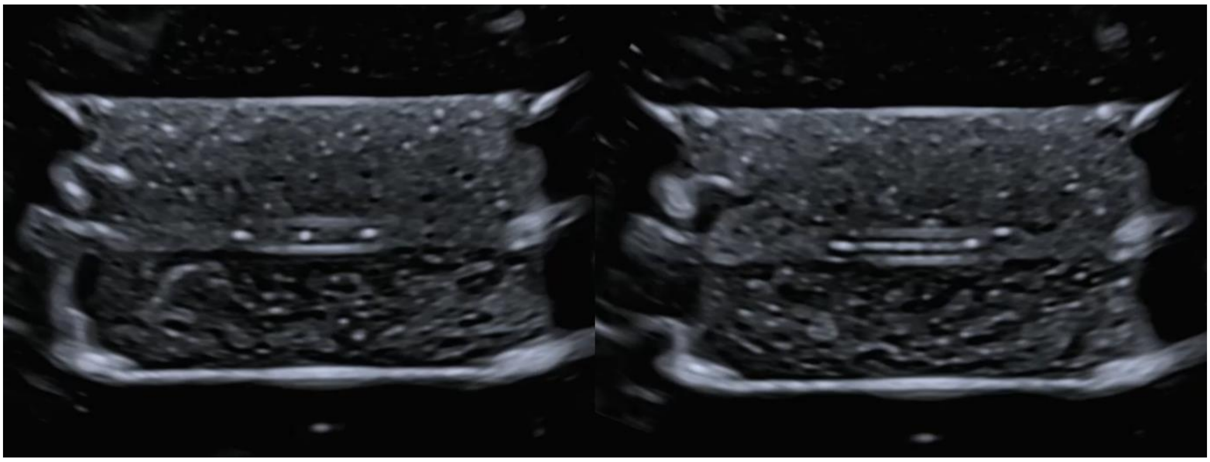

Figure 5-10: Ultrasound image of the first arrangement of wires. Left, the individual wires can be seen as 3 bright dots when the imaging plane intersects them. Right, the perpendicular wire shows as a bright line as it intersects the imaging plane.

The next arrangement (Figure 5-11) was a series of crosses, produced by wires strung diagonally to the sides of the phantom. This configuration required more wires for the same number of intersections but made the imaging and alignment easier, since the wires produced two intersections for a given plane. This meant that once two points were found, moving along a given direction brought them closer or separated them. When the two points coalesced into one, the intersection had been found.

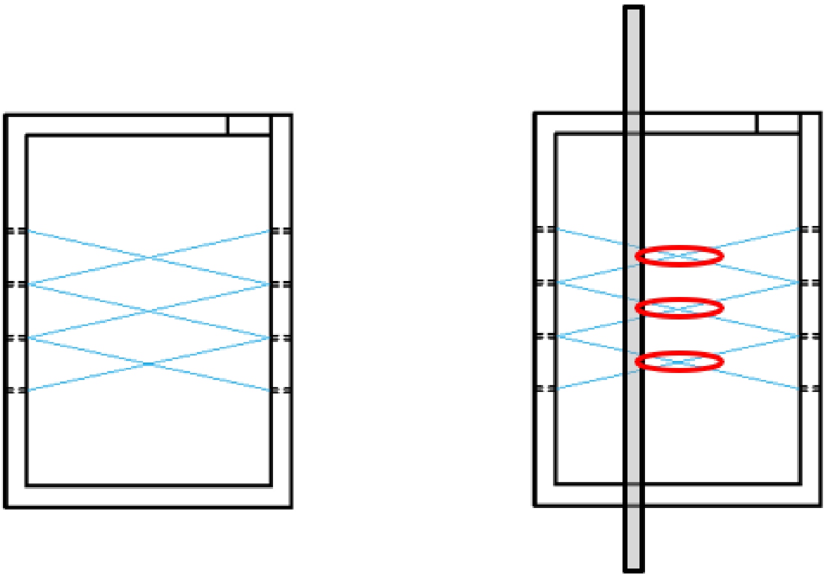

Figure 5-11:Diagram of the second arrangement. Diagonal wires were placed to produce 3 different intersections and reuse the holes for the threading of the wires. While this arrangement allowed the imaging plane to be moved along cardinal directions, the angle of the wires would produce coalescence along a longer region than 90° intersections (Right diagram).

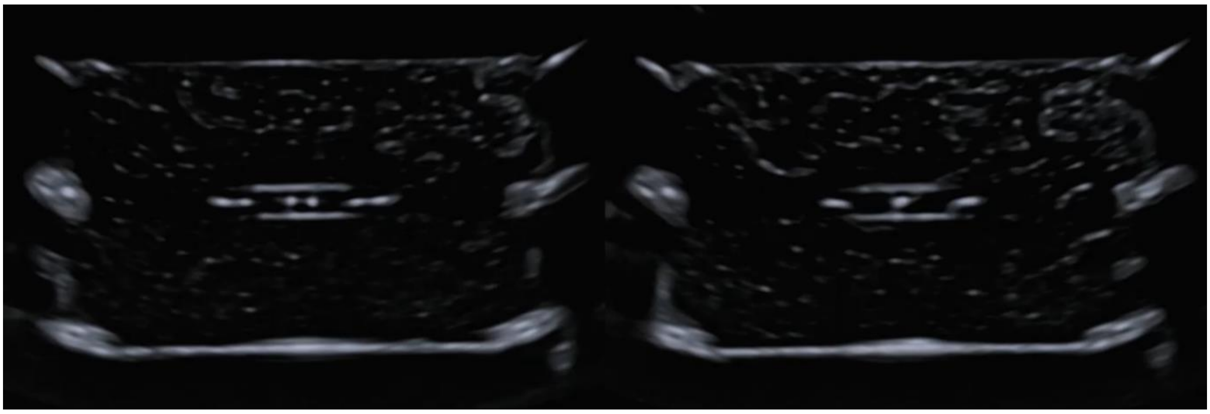

Figure 5-12: Ultrasound image of the second arrangement of wires. Left, the individual wires can be seen as 6 bright dots when the imaging plane intersects them. Right, the 3 pairs of wires coalesce into 3 dots as the imaging plane moves to the central position where the wires intersect.

This arrangement also allowed us to test the effect of different wire intersection angles on the imaging. Although the wires crossing at a sharper angle could, theoretically, produce a sharper point, no benefit was found, additionally, the point of the intersection becomes harder to identify, since there is a longer region across which the wires are close enough to coalesce into one point in the ultrasound image.

It was then decided to place the wires so that they crossed at 90° angles. This arrangement (Figure 5-13) unfortunately, produced a series of unnecessary intersections that could be misleading when attempting to identify the points that had been selected for the exposures.

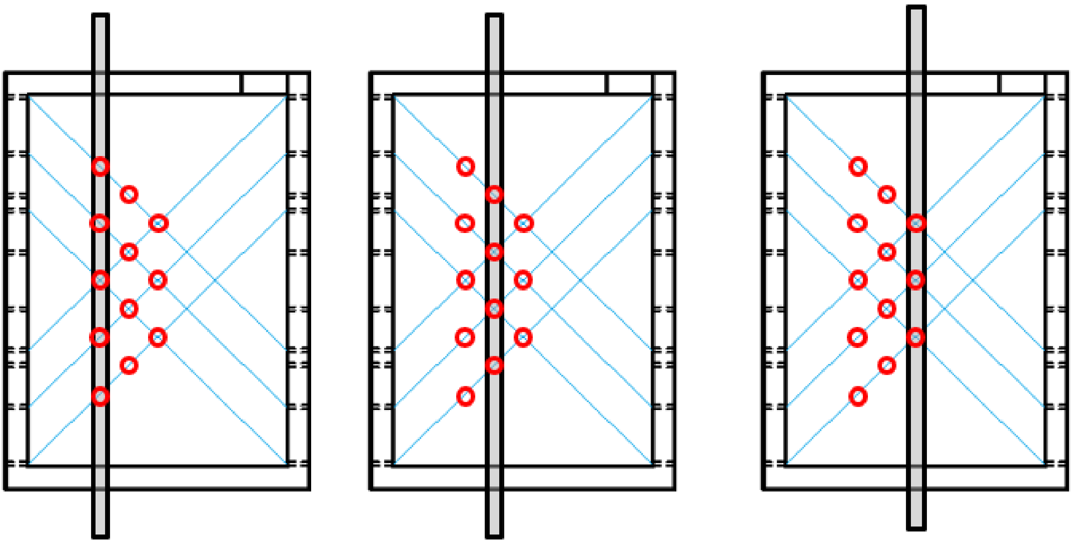

Figure 5-13: Third arrangement. The 90° intersections produce sharp and distinct coalescences. However, the numerous wires produce intersections at locations other than the centre, which can be misconstrued for the actual target of the QA process.

This problem is further exacerbated by the fact that the imaging probe does not offer homogeneous imaging quality over the plane. The visibility of insertions is maximal at the centre of the plane while it falls off at the edges. This could cause the imaging plane to be in the positions of the left and centre diagrams, where 5 and four intersections should be visible rather than the appearance of the rightmost schematic, where there are only 3. This results in misidentification of the position of the transducer relative to the sample. Furthermore, since the wires are all threaded manually, the increased number of intersections complicated manufacture of the samples.

While at first it was thought that having as many intersections as points to be targeted would represent an advantage, as each target would correspond to a single identifiable point, it was then decided to simply use two wires to form a single point that would serve as a reference and position the exposures relative to it (Figure 5-14). This would rely on the system's own movement control but also open the possibility of testing it, by measuring the distance between the lesions produced during the exposures, but also shorten the QA procedure, as it required fewer alignment steps. Additionally, the position of the intersections is also susceptible to error, and so aiming at several does not guarantee the desired results. The phantom was also redesigned to allow 9 exposures in a 3x3 grid rather than 3 exposures along a line.

Due to the size of the wires, the size of the intersection is a small 25x25x50μm^3 region, as they cross with one another. The size of this object for the purposes of alignment will be entirely determined by the resolution of the imaging mode, rather than by the object itself.

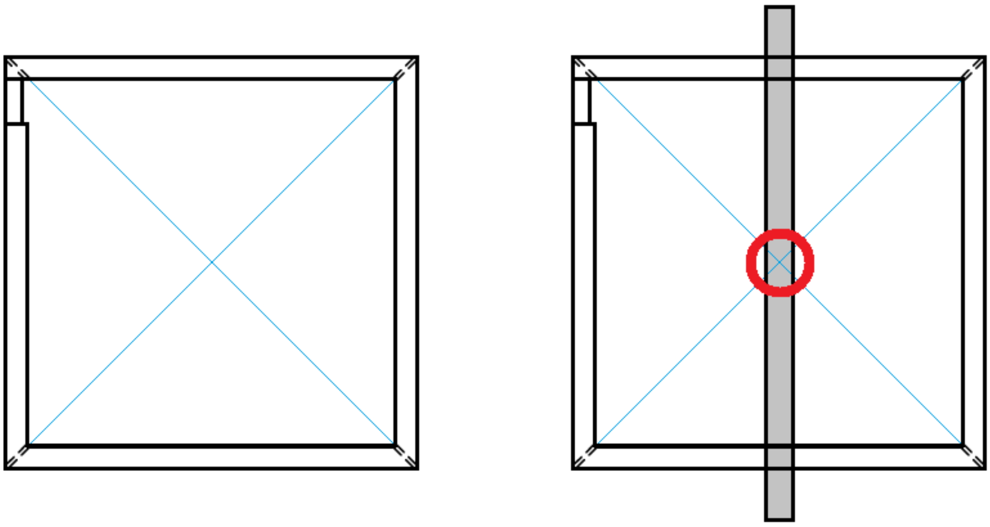

Figure 5-14: Final design. This arrangement produces a unique intersection from two wires at 90°. This simplifies the threading procedure and results in a unique intersection. This design was also modified to 9 lesions in a 3x3 grid, rather than the previous configurations where 3 lesions were planned.

This arrangement still opens up the possibility of misalignment of the imaging planes and the sides of the phantom, producing the lesions at an angle. Under such conditions, some of the lesions could fall too close to the edge of the phantom, which would result in the acoustic beam colliding with the casing. However, the phantom was designed so that the acoustic beam would have a 5mm clearance from the edges of the casing, (Figure 5-15) which would mean that even in that case it would not be a problem, and we found that visual alignment was good enough.

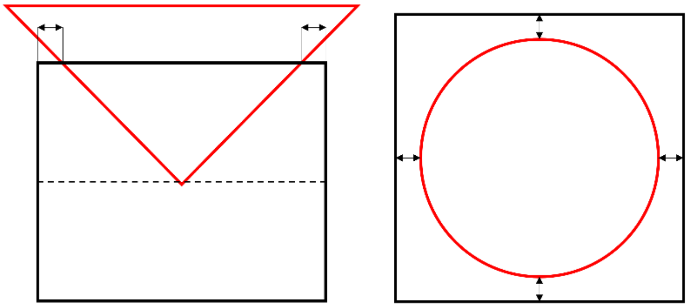

Figure 5-15: The dimensions of the casing, in black, were designed so that when the acoustic beam, in red, was targeted on the centre, there would be 5 mm clearance (indicated by the double pointed arrows) from the edge of the frame to avoid obstructing the beam. Left, side view. Right top view.

The phantom is mounted on a platform that fixes its position for the QA testing. This platform suspends the phantom above an absorbing layer to prevent reflections back into the phantom (Figure 5-16). The head of the transducer is then visually aligned with one of the sides of the phantom and then, using the ultrasound guidance system, the centre of the phantom is found.

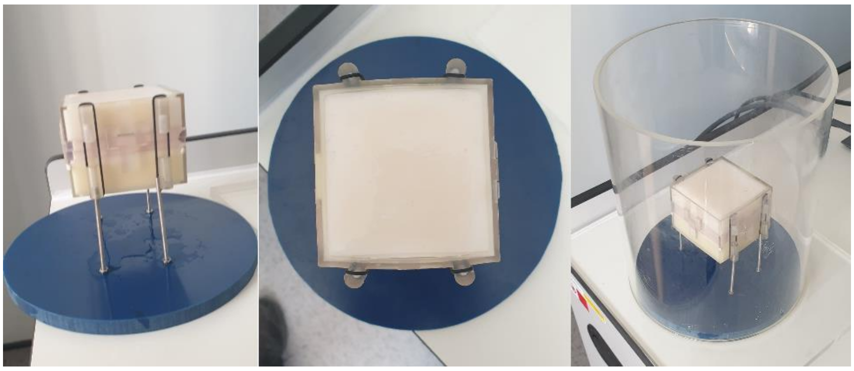

Figure 5-16: The phantom mounted atop the platform. Left, side view. Centre, top view. Right, The platform inside the tank.

5.4 QA procedure

In order to perform a QA measurement, samples must be prepared ahead of time. While the non-thermochromic layers can be prepared in advance and careful handling and storage allows their use for a week, thermochromic samples should be prepared the day before, and stored in a wet environment under a light vacuum.

The phantom must be mounted underwater to prevent the formation or trapping of bubbles in the interfaces between the samples. Once the phantom is affixed to the platform, it can be inspected using ultrasound imaging to identify the presence of bubbles, and if they are detected, the phantom is dismounted and reassembled under water.

Once the phantom is adequately mounted, the robotic arm is visually aligned with the side of the phantom, to ensure that the imaging plane is aligned with one of the sides of the phantom. The identification of the centre of the phantom can then proceed. Ultrasound imaging of the phantom at this point will show a series of features that are important to identify.

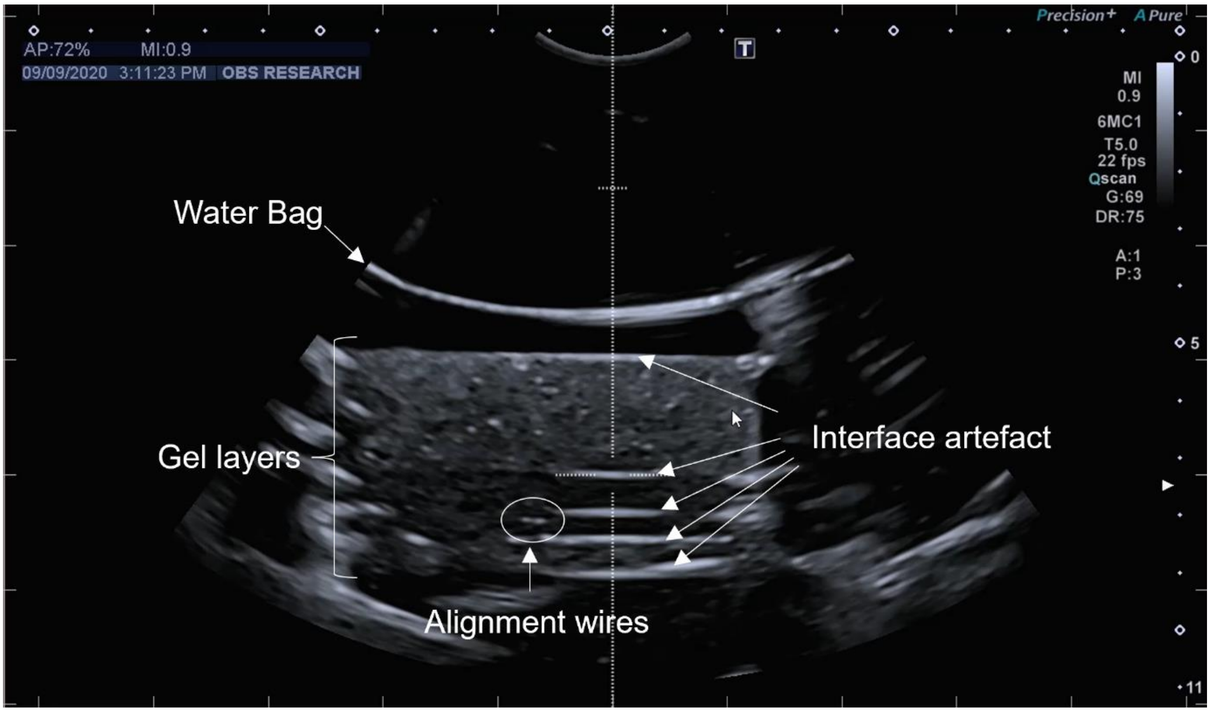

Figure 5-17: US image of the phantom with highlighted imaging features.

The alignment wires show as two bright spots that separate and move closer as the imaging plane moves away or towards the centre of the phantom respectively. The centre can be identified as the point where the two dots coalesce into one. This centring can be improved by moving away from it, causing the dots to separate again, registering the position, and moving in the opposite direction until the two points separate again to a similar extent. The midpoint between those two positions is the centre.

In order to perform the 9 exposures more easily it is recommended to save the positions of the parallel planes at +10, 0 and -10 mm relative to the centre of the phantom. At each of these planes, 3 different exposures can be made at once by using the exposure planning system to place the points. The system allows selection of a starting and finishing point, placing of any number of exposures, control of the spacing between them and adjustment of the position of the endpoints of the line. The exposure power can then be selected and the insonation can proceed. Exposures were done in continuous wave mode at the fundamental frequency (1.66MHz) for 10 with a cool down time of 5 seconds between exposures.

5.5 QA software

As part of this project, it was necessary to write software that accurately measures the size of the lesion, as it was intended to use the correlation between size and power presented in section 5.2 in order to perform QA measurements. Due to the possibility of variation in the in criteria between assessments, it was decided to develop a semi-automatic measurement algorithm.

The software requires that the sample is photographed with a grid printed on transparent plastic, which acts as a reference for the dimensions of the lesions. The grid is formed of a series of crosses spaced 5 mm apart. The grid must be placed so that the lesions lie in the centres of the squares formed by the grid.

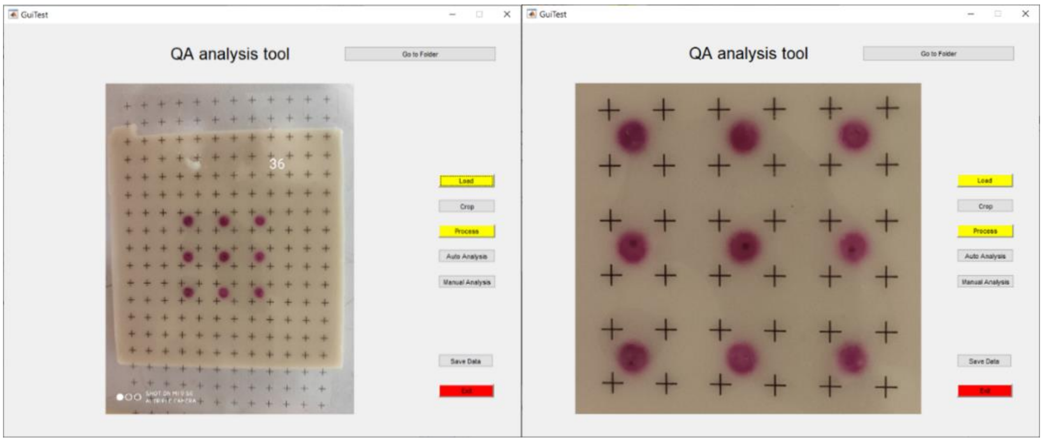

Figure 5-18: Left, the sample photographed with the grid is loaded into the MATLAB programme Right, the image is cropped for better analysis

The software first requires uploading of the image for analysis and provides the option of cropping the image (Figure 5-18). This first step allows the user to zoom in on the region where the lesions are contained, to facilitate the rest of the analysis.

The processing of the image can then start. The program requires clicking on the positions of the grid, two adjacent crosses along the vertical direction and two along the horizontal direction (Figure 5-19). These two points provide the position in pixels which is then used to calculate the calibration of millimetres to pixels.

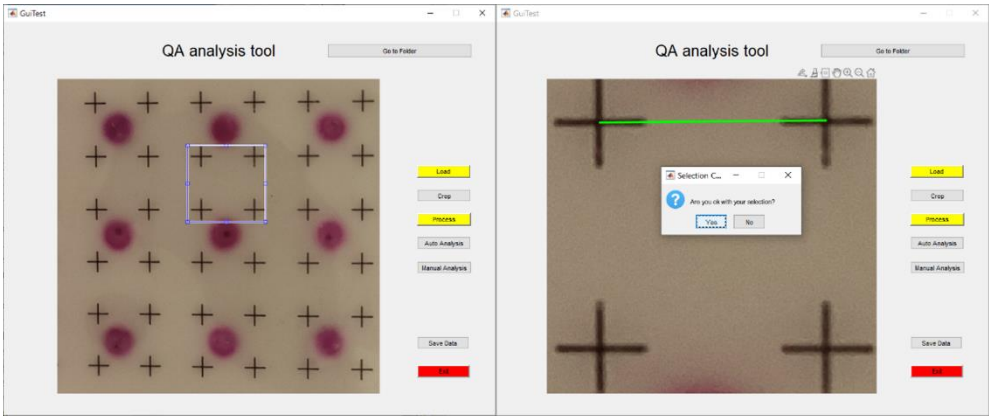

Are you ok with your selection?

Figure 5-19: Right, a region with 4 crosses is selected for the scale calibration. Left, a dialog box confirms the selection of the crosses

The software then requires clicking on the positions of the lesions (Figure 5-20, left). These positions are then used to crop the image around each of the lesions (Figure 5-20, right). The size of the cropped region is the distance between the crosses. This narrows the analysis to the region containing the lesions and ignores the rest of the image. At this point the image is considered processed and analysis can start.

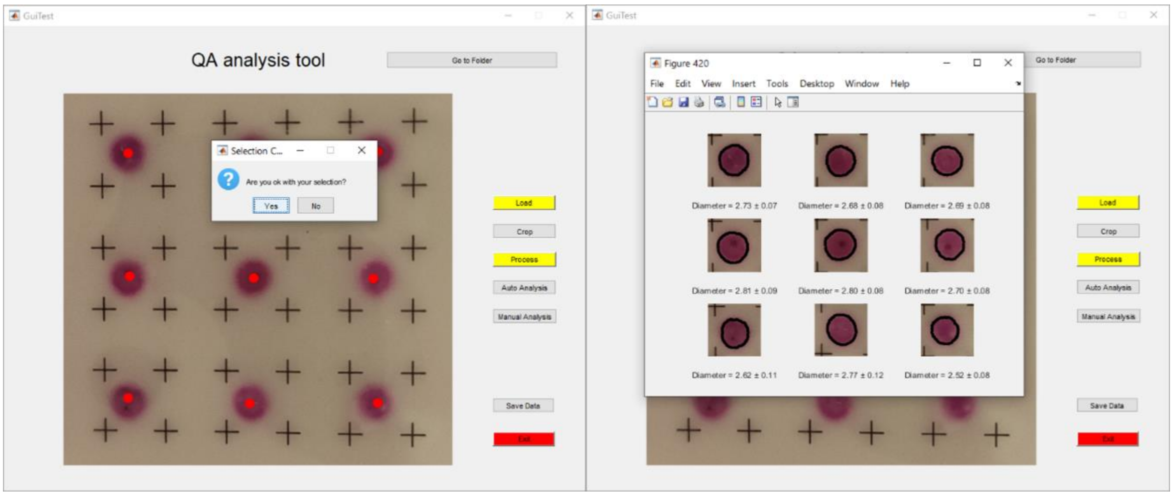

Are you ok with your selection?

```
Diameter = 2.73 ± 0.07   Diameter = 2.68 ± 0.08   Diameter = 2.69 ± 0.08
Diameter = 2.81 ± 0.09   Diameter = 2.80 ± 0.08   Diameter = 2.70 ± 0.08
Diameter = 2.62 ± 0.11   Diameter = 2.77 ± 0.12   Diameter = 2.52 ± 0.08
```

Figure 5-20: Left, the point marks the selections with red dots and provides a dialog confirmation box. Right, the auto-analysis produces a secondary figure with the subsections and the calculated diameters and outlines.

The automatic analysis function takes the images which are then used to produce a single channel image from the red colour channel minus the green colour channel. This combination was found to produce the maximum contrast of the lesions while minimizing the contrast of the crosses in the image. This effectively removes the crosses, which are visible in both channels, while only leaving the lesions, which are more visible in the green channel than in the red one as detailed in section 3.4.1. The resulting image is then turned into a histogram (Figure 5-21). The histograms of these images present bimodal distributions with peaks corresponding to the background and the lesion. From that data, the point at the colour level which is ¾ of the difference from the background to the lesion is identified as the edge of the lesion. This was a justifiable choice as it was shown in section 3.4.1 that the colour change should highlight the heated regions. Since the photograph will capture both heated and unheated regions, the colour difference within the image will be enough to identify heated regions, and the contrast between them is high enough to ensure that the difference in colour is due to the heating and not any other effects.

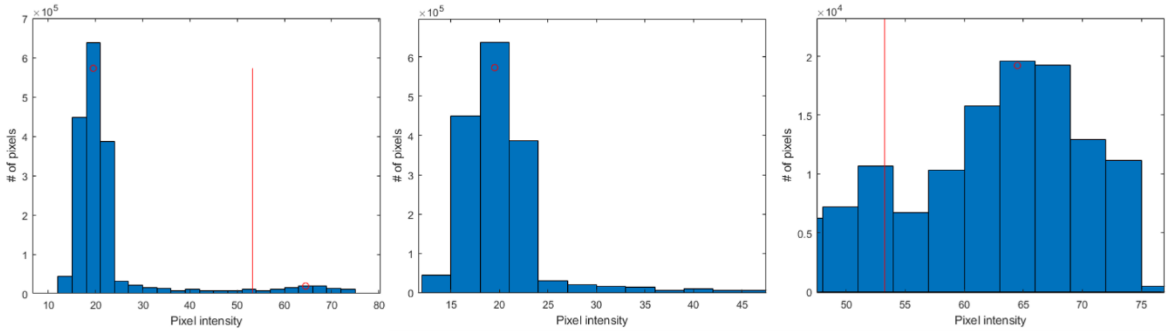

Figure 5-21: Left, the histogram of the images with a red vertical line at the point identified as the edge of the lesion. Centre, the peak of the leftmost region, the background. Right, the peak of the rightmost region, the lesion.

The software then identifies the region of the image at around that level and obtains the outline of the region. Since the lesions are roughly circular, the centre of the region is calculated as the centre of mass of the distribution which is then subtracted from the points. The coordinates of the point are then converted from cartesian into polar coordinates, the corresponding radial values are averaged to obtain the average radius of the lesion.

The manual analysis loads the cropped images of each of the lesions separately and requests that 3 different points along the edge of the lesion be clicked. These points define a unique circumference (Figure 5-22).

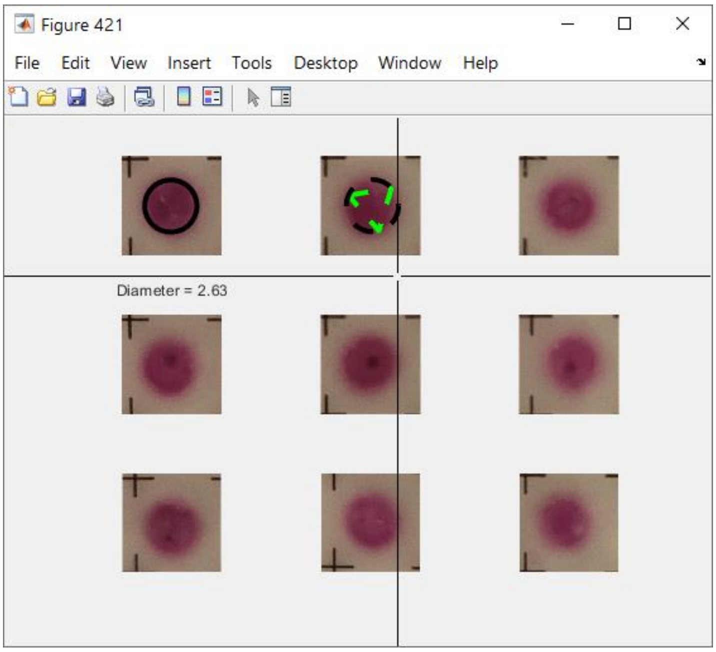

Diameter = 2.63

Figure 5-22: The manual analysis opens a new window. Upon selecting 3 points a dialog box is open. Confirmation plots the circle and shows the calculated diameter (Top left), and rejection plots a dashed black circle along with a green dashed triangle showing the previously clicked points to serve as a reference for reselection.

The data is then saved as a pdf file with the date and time of the analysis as well as the measured radii from the analysis performed.

5.6 Assessment of acoustic output

Lesions were produced across a range of intensities around an arbitrarily selected level. It was found that the diameters of these lesions increased linearly across the selected range and that the average size of the lesion correlated with the acoustic power delivered by the transducer.

Samples were then measured across a range of different intensities to measure the size of the lesion and test whether lesion size could be used to assess the exposure intensity. Measurements were performed on 3x3 grids of lesions, which were then averaged to produce each of the points in Figure 5-23.

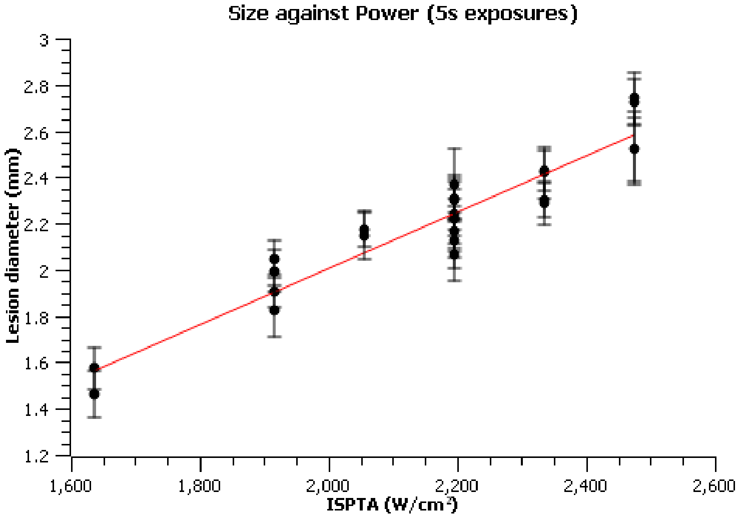

Figure 5-23: Lesion diameter against ISPTA for 5s exposures.

The data was fit to the line: $L = 0.0012\,I - 0.430$, with a value of R^2 of 0.90. Which shows a reliable trend in the data. Lesion diameters can be seen to increase linearly with intensity.

5.7 Assessment of targeting accuracy

The possibility of testing the targeting accuracy arose during the use of the TTTS-HIFU system for the assessment of acoustic power. The ultrasound imaging presented increased echogenicity in the exposed regions. The MATLAB interface included an overlay that plotted the expected in situ energy deposited by the exposures. This overlay could be adjusted to show isolines of different intensities ploted over the US image. The combination of the echogenic regions and the overlays allowed the evaluation of the targeting system by comparing the positions of the heated regions and the expected energy deposition.

When the gel is exposed to ultrasound an echogenic region which can easily be identified under ultrasound imaging forms. As can be seen in Figure 5-24, the region aligned with the targeting overlays used by the MATLAB function to indicate the regions in which ablation is to be expected.

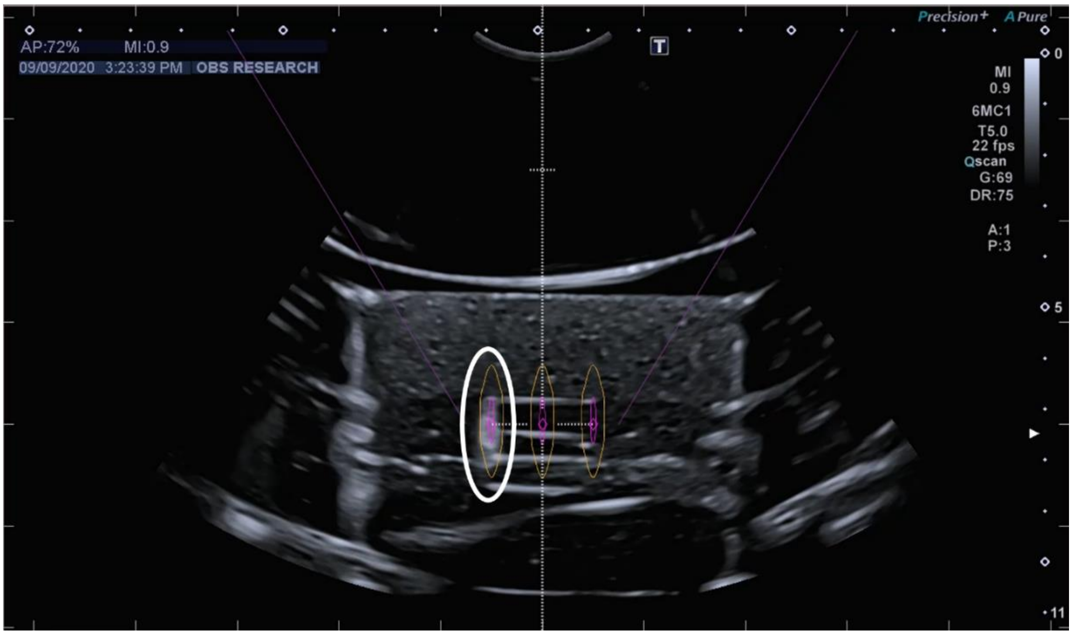

Figure 5-24: US image of the phantom after exposure. Highlighted in the white ellipse the echogenic region is contained within the orange targeting overlay.

The close up of the region after three exposures in Figure 5-25, shows how the echogenic regions align with the orange outlines of the targeting system. The lesions are contained within the two middle thermochromic layers and do not extend into the non-thermochromic layers.

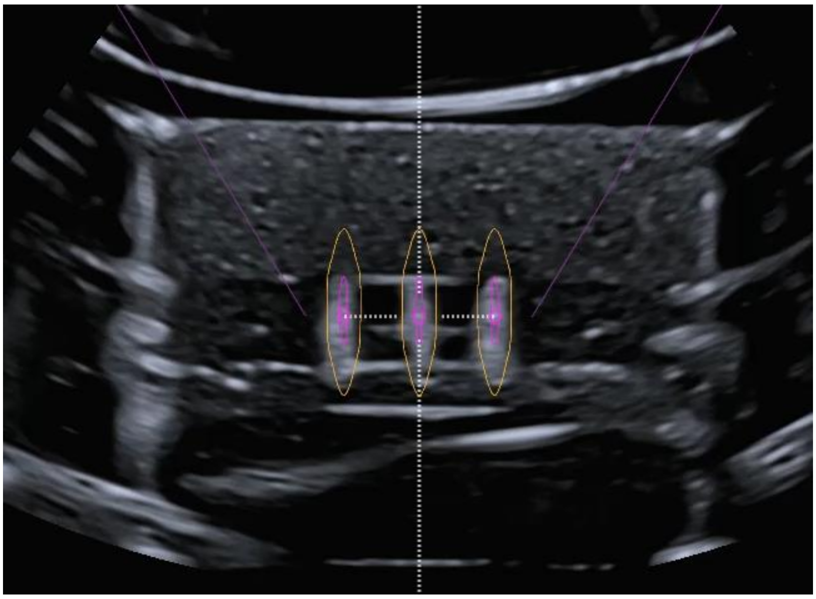

Figure 5-25: Close up of the exposed regions showing increased echogenicity

From the measurements of attenuation of gellan gum samples with and without silicon oxide, across the range of temperatures from 20 to 45°C, it can be seen that the attenuation of gellan gum drops, while the attenuation of gellan gum and silicon oxide does not. This seems to indicate that the overall contribution from gellan gum, which is mostly absorption, reduces as temperature rises and the contribution of silicon oxide, which is mostly through scattering, increases. This manifests as the increased echogenicity seen in the US images, which facilitates the identification of the heated region within the gel.

The movement of the treatment head can also be analysed by measuring the positions of the centres of the lesions. Since the plastic grid has 5 mm spacing and the separation of the lesions is 10 mm, this can be done by aligning the crosses with the centres of the thermochromic lesions to assess the spacing.

5.8 Implementation of a QA procedure

For the adequate use of the phantom for power and targeting assessment there should be a reference setup process that is used to identify the desired power. Assuming that the system is the same as the TTTS-HIFU system or that it includes similar features such as B-mode US imaging along some targeting capabilities, the steps for this should be to first identify the centre of the phantom using the US targeting and coalescence location of the wires within one of the thermochromic layers.

Secondly, a range of different power exposures should be tested to generate a series of candidate exposure conditions that would be used as a reference. this is mostly because it is impossible to know a priori the efficiency of a different system that uses the phantom and while a similar power output to the one used is likely to be usable, it is not guaranteed. The selected power should be enough to produce lesions that are contained within the thermochromic layers without extending into the non-thermochromic ones, while simultaneously producing the biggest diameter in the interface between the two thermochromic layers. Additionally, it is desirable that the exposure is capable of producing an echogenic region that can be seen under the US imaging and can be used for alignment with an overlay such as the one used by the TTTS system. In the case of the TTTS-HIFU system, the size of the profiles represents different isolines of the calculated acoustic intensity from the added exposures, selection of these to show different isolines will produce different profiles. This method should be used to identify a configuration that tightly contains the resulting lesion.

After selecting the power to be used, new thermochromic samples should be created and 9 exposures should be made at the same power. This will allow generation of a more statistically relevant measure of the expected size and its associated uncertainties. After gathering this data, additional exposures can be created at 10% greater and lower powers, so that the relationship between power and lesion size can be defined for the specific system and the associated uncertainties can be used to define the range of acceptable values that the QA procedure must use before other maintenance processes are examined.

6 Application of the TMM to a BBB opening procedure in a mouse model

6.1 Introduction

The use of ultrasound based applications in the brain is an application of interest for various neurosurgeries for treatment of chronic pain[93], Parkinson's and essential tremors[94], as well as for blood brain barrer (BBB) opening techniques which aim to enhance the delivery of drugs to the brain[94–99]. These techniques are limited by the presence of the skull[100] and the ability to accurately target and evaluate the accuracy of this devices is very important[101,102].

The possibility of localizing the focus in such circumstances may be limited, as it may not be possible to insert certain hydrophone designs into a realistic mimic. Consequently targeting assessments have relied on MR[101] and US[102] imaging techniques.

The thermochromic TMM described in section 4.7 was used to detect the heating pattern from a pre-clinical system designed to expose mice to short pulses of US with the aim of opening the blood brain barrier (BBB) to enhance drug delivery. We considered this a particularly suited application of the thermochromic capabilities of the TMM as the small murine skull is certainly not suited for any kind of hydrophone mapping and their small sizes also limit the application of imaging techniques, as the resolution of the systems relative to the size of the object of interest is significantly larger than the case of a human skull.

The BBB prevents access of toxic substances to the brain. In order to overcome this, one option is to modify the delivery of drugs being used to make them capable of crossing this barrier, and ultrasound has been applied overcome this issue[94–98]. The system being used here uses short high intensity pulses which, combined with an injection of a contrast agent (SonoVue Bracco Imaging, France), to induce cavitation, temporarily opens the BBB allowing agents to be delivered to the brain. By controlling this process, drug delivery can be improved for treatment. These techniques are currently being developed with the intent of improving drug delivery to specific parts of the brain[94–98].

As the system is designed to use short pulse high intensity exposures and produce negligible heating, the exposure conditions were changed to longer exposures capable of producing a heat rise and the associated colour change of the TMM, and the interpretation of the results from these altered exposure conditions should consider this aspect. However, the main aim of these tests was to apply the TMM to the localization of the focus by identifying the heated regions during the exposure.

While the localization of the focus would ordinarily be done through the use of hydrophone measurements, this is not a feasible option when evaluating the position of the focus within a mouse skull mimic. Similarly limited applications, where a hydrophone cannot be positioned to measure the field could benefit from the application of thermochromic phantoms.

6.2 Materials and Methods

6.2.1 Experimental setup

The system is shown in Figure 6-1. It consists of a focused transducer (H117 Sonic Concepts, Inc. Washington, USA), with radius of curvature 64 mm, diameter 63.5 mm and centre frequency 300 kHz. The transducer has a 20 mm aperture through which a small transducer (Y107 Sonic Concepts) is inserted in order to measure cavitation. This capability was not necessary during QA exposures but is necessary for the BBB opening procedures as cavitation events are responsible for the phenomenon and must be monitored to ensure the experiments are successful. The transducers are mounted in a coupling cone (C-103 Sonic Concepts). The coupling cone has been modified to have a straight cylindrical extension in order that the focus lies 4 mm beyond the rim of the cylinder.

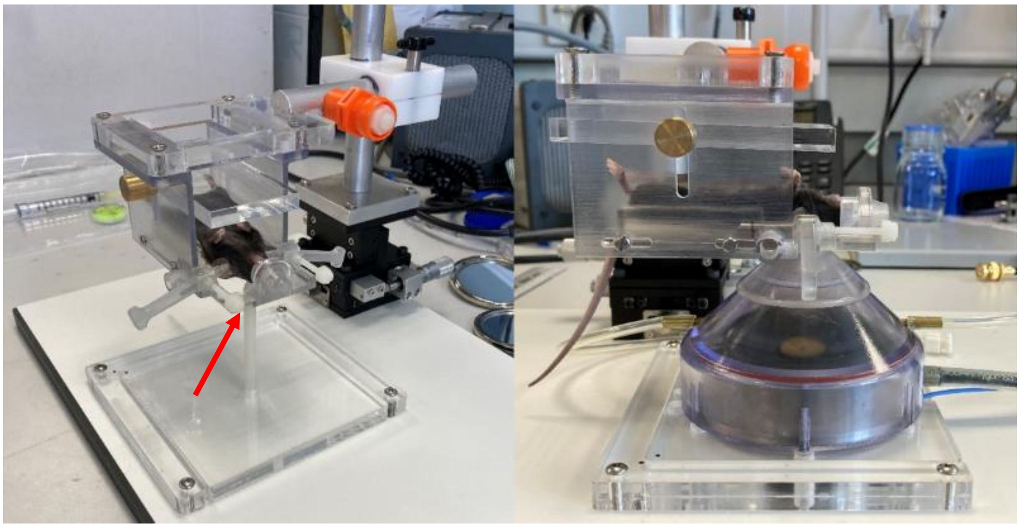

Figure 6-1:Left a mouse mounted onto the linear stage platform atop a pointer that indicates the position of the focus for alignment. The red arrow marks the tip of the pointer, below the head of the mouse. Right, the transducer in the conical container replaces the pointer for exposures.

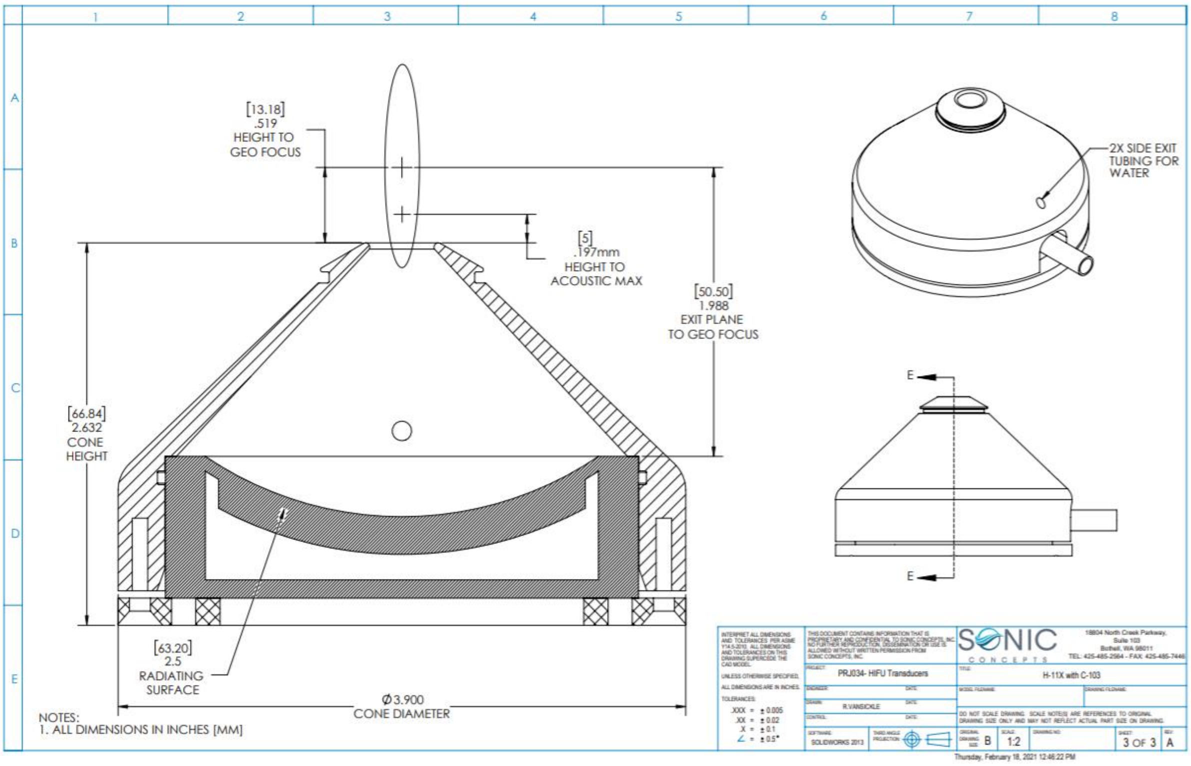

Figure 6-2: Original schematics of the C-103 cone. The cone was later modified to add a cylindrical section extending 4 mm below the focus.

The container is filled with water, which provides the coupling medium through which the acoustic waves propagate from the transducer to the mice, without the need for immersion of the mouse in a tank, thus allowing the mice to be kept out of the water, without breathing support. The cone is connected to a pump/reservoir unit (EK-Quantum Kinetic TBE 200 D5 PWM D-RGB, EK Water Blocks, Slovenia) and a membrane contractor (3M-Liqui-Cel, Lenntech, The Netherlands) to degas the water. The therapy transducer is driven by a 33250A Arbitrary Waveform Generator (Agilent, California, USA) connected in series with a A300 55dB amplifier (Electronics & Innovation Ltd. Rochester, New York, USA).

The system includes a platform mounted atop a linear stage trimming platform (GXYZ-60, Seafront) that allows control of the position of the mouse's head with submillimetric precision. Attached to the platform there is a 3D-printed bed designed to hold the mice. The bed includes locating rods that can be affixed onto the mouse to fix the position of the head in a cone that holds the snout.

6.2.2 The skull phantom

In order to reproduce the mouse skull, a single CT-scan of a skull (Mouse skull from micro-CT by Mark-U) was digitized, and 3D printed with an Object Eden 350 V (SMG3D, United Kingdom) 3D printer in VeroWhite (Sculpteo, Paris). The skull mould was divided along a transverse plane and modified for assembly. The modified phantom can be seen in Figure 6-3.

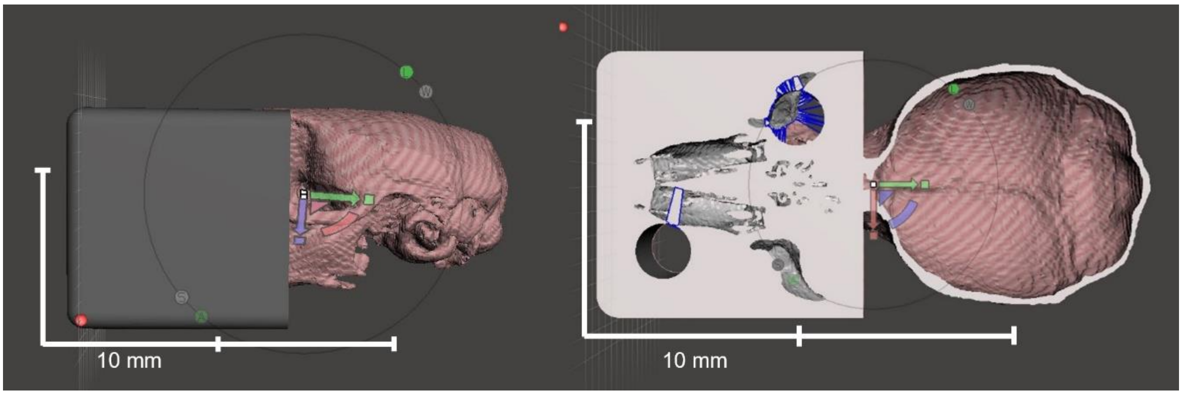

Figure 6-3: 3D models of the skull mould. Left, side view of the mould. Right, horizontal cut of the mould.

The skull had a 12.4 mm side cube added to its front for assembly. The phantom has a total length of 25.4 mm. The skull has been divided across a horizontal plane, roughly 5 mm from its bottom, 3.7 mm from its top. The skull has a thickness which varies between 0.5 and 0.6 mm

	Density (kg/m^3)	SoS (m/s)	α (dB/cm MHz^n)	n
Bakaric	1181	2475	3.615	1.020
Measured	1181 ± 21	2525 ± 24	3.525 ± 0.1	1.100 ± 0.1

Table 6-1: Acoustic properties of VeroWhite

The acoustic properties of VeroWhite shown in Table 6-1 were measured using the FAIS method presented at section 3.2, applying the correction for reflections. The density was measured by direct measurement of the weight and the dimensions of the samples. VeroWhite is sufficiently rigid to allow its measurement without damage. The values were compared with those from the work of Bakaric et al[103].

6.2.3 Phantom setup

In order to encase the TMM in the skull phantom the recipe from chapter 3 was followed and a mixture was prepared using a temperature of 55°C in order to enable the dye to be mixed while preventing gelation which occurs at 50°C.

The mixture was then poured into a heated glass plate which was itself placed in a water bath, maintained at 55°C. The plate was deep enough to contain a volume of at least 2 cm depth while being much more open than a beaker, enabling the manipulation of the gel. The 2 cm depth allowed bubbles which can form during the mixing and preparation of the gel to float to the surface and thus be avoided in the mounting of the phantoms.

10 different VeroWhite phantoms were printed in order to be able to prepare multiple samples at once. The skull phantoms were then submerged in the mixture and mounted while inside the gel. This allowed the gel to solidify into a whole brain, rather than requiring mounting in two halves.

In order to expose the phantom to the acoustic beam, the phantom was held in place using the rods in the mouse-bed. The skull mould was attached to a AAA battery using blue tack which rested on the bed for a better control of the position of the mould.

Figure 6-4: Left, the rods being used to hold the skull phantom in place. The rods, marked by the yellow outlines, were inserted into the ocular cavities of the skull phantom, marked by the black outline. Plastic screws, marked by red outlines, affix the position of the rods. Right, a battery was attached to the phantom so it could rest on the bed for better stability.

It should be noted that in order to fit the rods into the skull phantom, the skull ended up upside down meaning that the top of the skull was in the path from the beam to the brain and that the bottom of the skull was behind the brain, from the direction of propagation of the beam.

6.2.4 Acoustic exposure details

For the tests described in this work, the transducer was driven in continuous wave mode at its third harmonic (900 kHz) as the original experiment we were testing was using the H177 transducer to replicate the work of Morse et al[99] which used 1MHz. The focus was targeted on the middle of the skull using the plastic pointer seen in Figure 6-1. The pointer has been designed so that its end is at the position of the focus. Using the movement of the trimming platform the pointer can be aligned on the outside of the skull and the pointer can then be replaced with the transducer.

A 6 mm slab of the thermochromic material was mounted on the gantry and aligned with the pointer in order to identify adequate exposure conditions for subsequent tests in the brain phantom.

Figure 6-5 shows the results of the exposures in the thermochromic slab. The slab was exposed 3 times in different locations for 30 seconds. Exposures were made with a peak negative pressure of 1.36 MPa. The first and third attempt produced elliptical lesions of approximately 3 mm in diameter with 6 mm of length (they extended from one end of the slab to the opposite. The lesions where sharply delimited, with a stark contrast between the lesion and the background. The second exposure produced a significantly smaller lesion, circular in shape, with a diameter of approximately 1.5 mm, but similarly strong contrast.

Figure 6-5. 158.5 p-p mV MPa exposures on the thermochromic slabs. From first to last: top left, top right, bottom.

While slightly inconsistent, it was decided to proceed with this power setup, as the lesions were identifiable and visible.

The mouse phantom was exposed under four different conditions: the brain TMM phantom, on its own, the brain covered by the bottom and top halves of the skull separately, and the brain encased entirely by the skull.

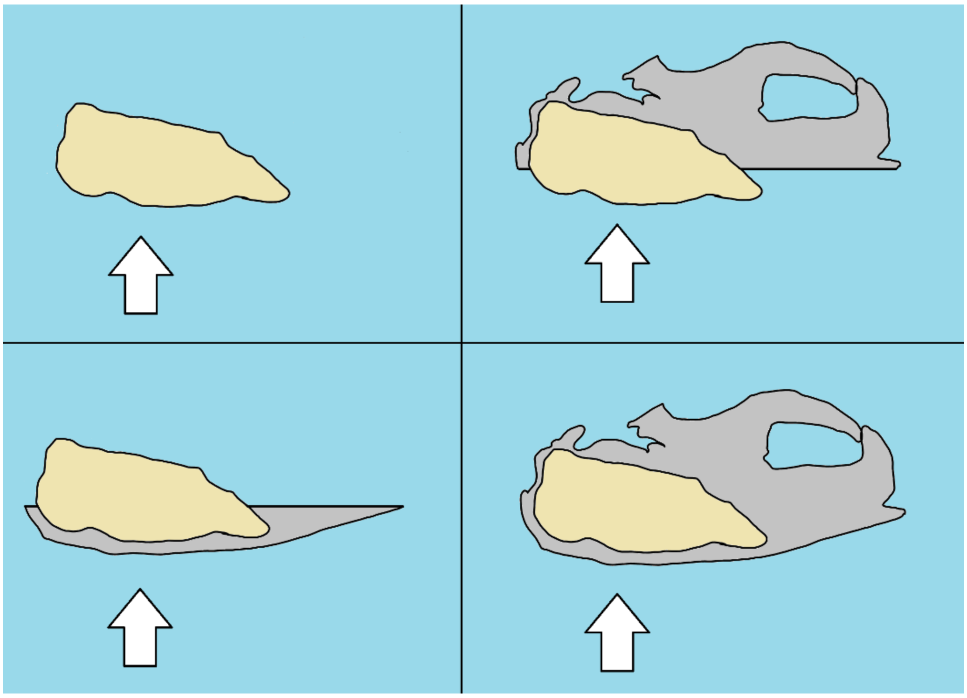

Figure 6-6: Schematic representation of the four different exposure conditions tested. The arrows indicate the direction of propagation of the acoustic beam. Due to our setup, the skull was upside down. Top left: The brain on its own. Top right, the brain with the bottom half of the skull. Bottom left, the brain with the top half of the skull. Bottom right, the brain encased in the skull

The first exposure, the brain TMM on its own, allowed us to reiterate that the selected power was capable of producing a lesion that would be contained in the gel phantom. This power could then be applied to subsequent exposures, with the possibility of increasing it if lesions could not be formed after the addition of the skull phantom. The two next exposures would show the effects of the skull separately, one of the halves being in the path between the gel and the transducer and the other half being placed behind the gel. These two halves would presumably have different effects, one directly attenuating the acoustic wave before it reached the target and the other producing reflections propagating the energy back into the target. The final exposure would then be able to combine the information gathered from the previous exposures and adjust for any expected effects.

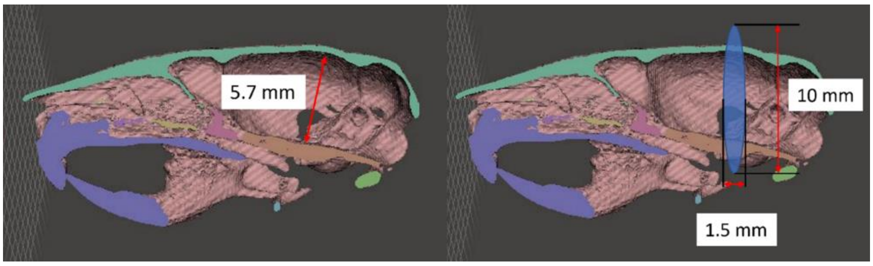

Figure 6-7: Schematic of the experimental plan. Left, sagittal cut of the skull showing the thickness of the brain. Right, the blue ellipse approximates the expected location of the focus over the skull.

Figure 6-7 shows the scale of the size of the skull along with an overlay of the expected size of the focus laid over the skull. The measured distance of 5.7 mm was used for the computer simulation in the following section.

While the aim of the test was to see how well the thermochromic TMM could be used to identify the position of the focus after propagating through the skull, the size and shape of the lesion is not determined solely by the shape and position of the focus. The absorption of the different materials and their thermal properties will also affect the distribution of heat within the phantom and consequently the size and shape of the lesion.

6.3 Results

Direct exposure of the TMM, as shown in Figure 6-6 (top left), resulted in a small lesion inside the mimicking brain (see fig 6-11), showing that the energy was able to reach the centre of the gel.

Figure 6-8. Lesions produced on the brain exposures. The brains after direct exposure. All brains show a slight pink tint, which can be seen from the outside.

The shape of the lesions was found to present a slight variation in the three different tests but were similar in size. Lesion one (Figure 6-9 top left) presents an elliptical shape with minor diameter of approximately 2 mm and major diameter of 4 mm. Lesion one is at angle relative to the craniocaudal axis because the sample rotated under the acoustic pressure. Subsequent exposures were better affixed, preventing the rotation. The second exposure (Figure 6-9 top right) presents a circular shape of 4 mm in diameter. The third exposure showed again an elliptical shape with diameters of 2 and 4 mm, minor and major respectively, which is aligned with the craniocaudal axis.

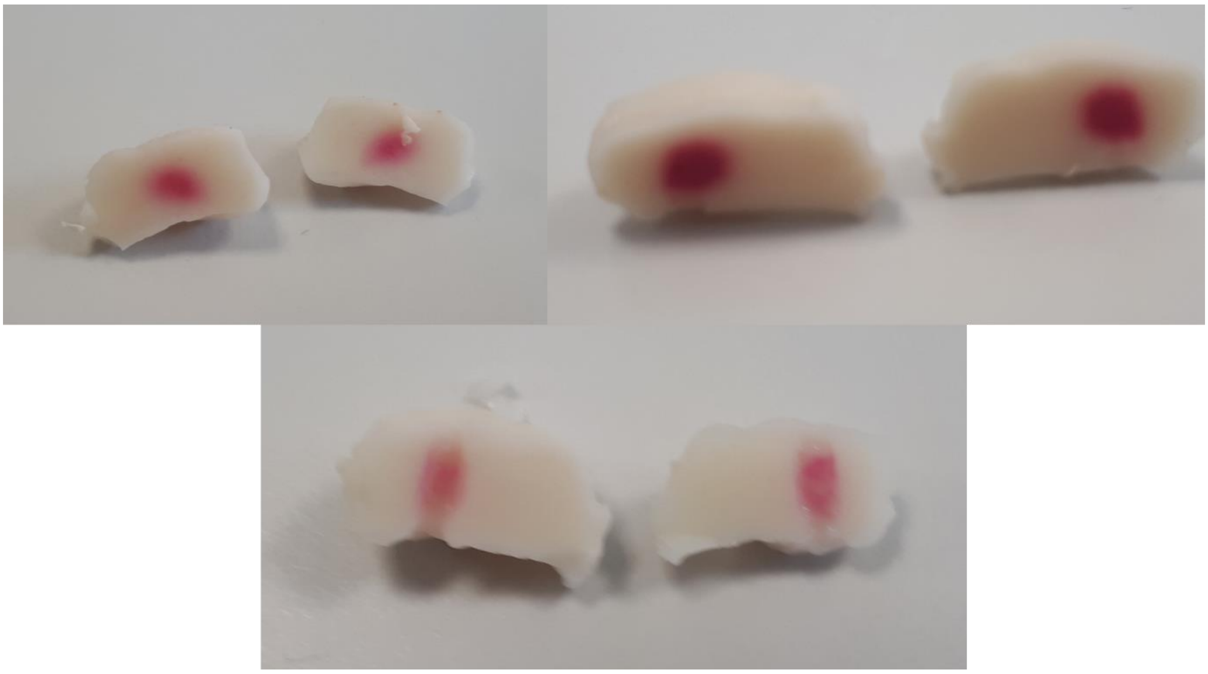

Figure 6-9: The three brains cut in half after exposure. From first to last: top left, top right, bottom.

These exposures confirmed that the system was able to create lesions in the gel. It was expected from this point that the presence of the skull in the path of the beam could attenuate the beam and reduce the size of the lesion.

Considering the position of the skull it was decided to test the exposure with the bottom half of the skull as shown in Figure 6-6 (top right). As explained in section 6.2.3, the bottom half of the skull would be behind the brain, so it was not expected to attenuate the beam and the lesion was expected to remain unaffected by its attenuation, but the effect of reflections was expected to be present.

Figure 6-10 shows the results of exposing the gel with the bottom part of the skull. The lesion was found to be largely irregular and have produced a surprising amount of melting, considering that the exposure conditions had not been changed. It was decided to repeat the exposure reducing the time to 20 seconds.

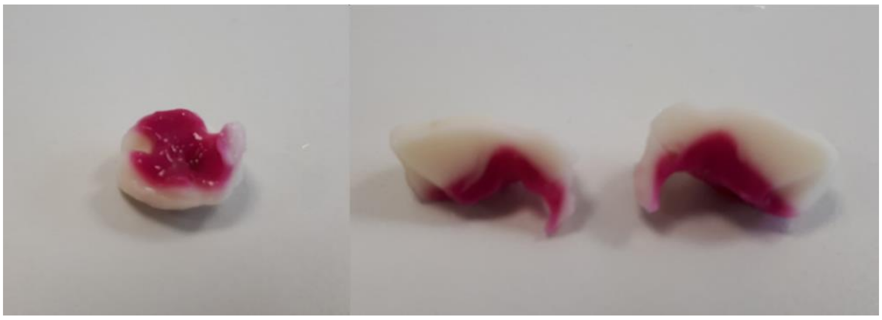

Figure 6-10: Lesion produced with the bottom of the skull attached. Left, the brain after exposure. Right, sagittal cut of the brain.

The second test, pictured in Figure 6-11, stills showed a highly irregular shape and had produced less melting, presumably due to the lower exposure time. It can be seen that in both cases the lesion had formed in the region in contact with the VeroWhite phantom and had grown into the gel through heat diffusion.

Figure 6-11: Second exposure with the bottom half of the brain.

It was then decided to test the 30 second exposure on the brain with the top part of the skull, which would lie in the path of the beam, to see the potential effect of the attenuation of the VeroWhite phantom. This exposure is represented in Figure 6-6 (bottom left).

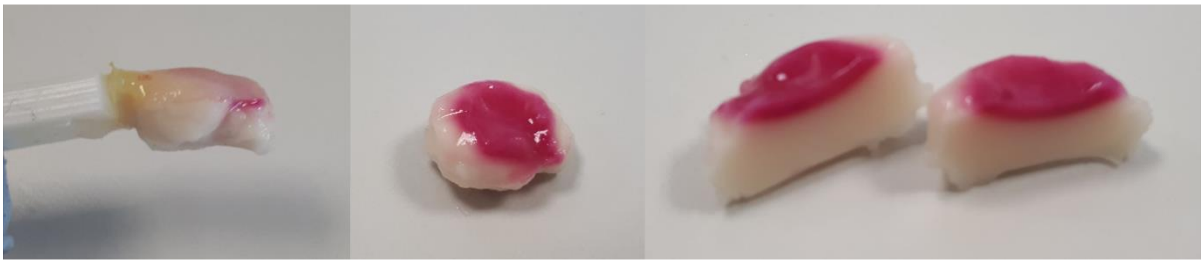

Figure 6-12: Lesions produced with the top of the skull attached. Left, the brain mounted on the skull. Centre, the brain after exposure. Right, sagittal cut of the brain.

Figure 6-12 shows the lesions produced with the top half of the skull attached. In this case, the lesion appears to have originated from the skull and extended outwards from it. A large amount of melting can be observed. It is hard to discern whether obstructing the path of the beam had a significant effect on the heat deposition, as the main factor was the contact with the skull mimic.

It was decided then to proceed with exposures with both halves of the skull as per Figure 6-6, bottom right. The result of the exposure with both halves of the skull can be seen in Figure 6-13. The lesions originate from two points of the skull and spread towards the centre of the gel. The lesion at the top part of the skull is larger than the lesion originating from the bottom, possibly due to the higher intensity of the beam, as this is the first point where it intersects with the phantom. The sagittal cut in Figure 6-13 shows a connection between the two lesions which could be a third central lesion like the one produced on the brain on its own.

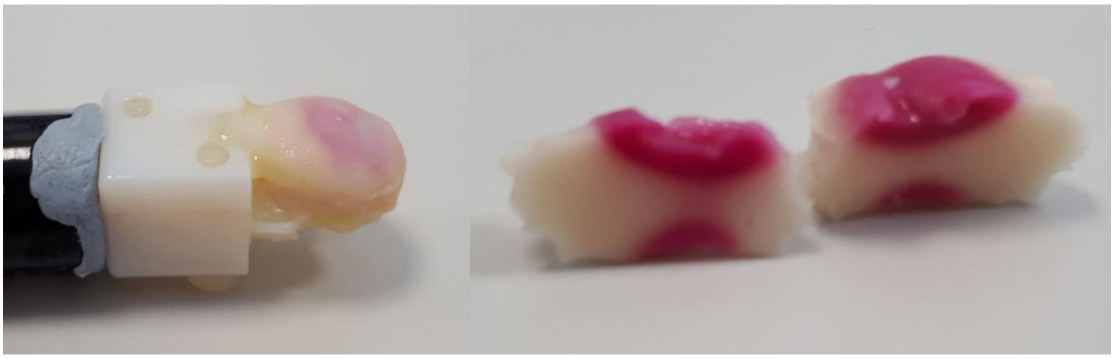

Figure 6-13: Lesions produced with the entire skull attached. Left, the brain inside the skull after exposure. Right, sagittal cut of the brain.

A second repeat was attempted, however, as Figure 6-14 shows, in this case the lesion was throughout the phantom, obscuring any possibility of discerning the pattern.

Figure 6-14: Second attempt at a lesion with the full skull phantom.

A third attempt at a 30 second exposure was made, which reproduced the initial findings.

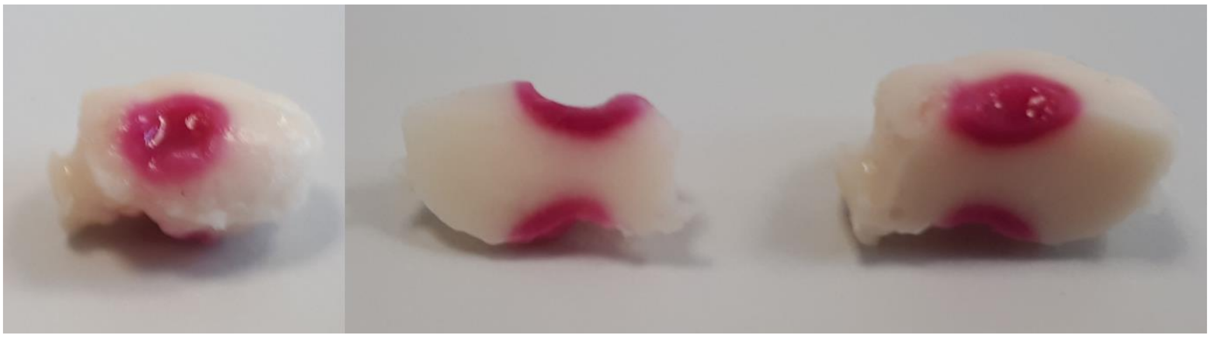

Figure 6-15: Third repeat of a 30 second exposure of the brain gel encased in the skull phantom.

A final test was made with a 5-second-long exposure to try to reduce the size of the heated region. The uncut and cut gels can be seen in Figure 6-16 and Figure 6-17

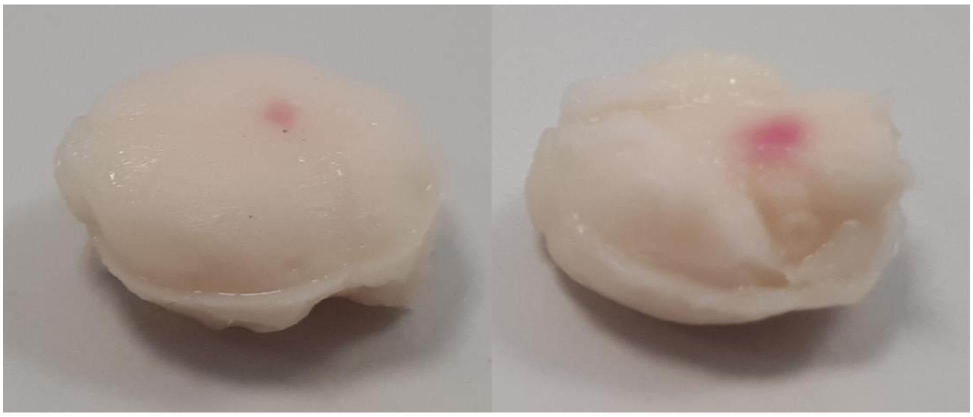

Figure 6-16: 5 second exposure of the gel brain encased in the full skull phantom.

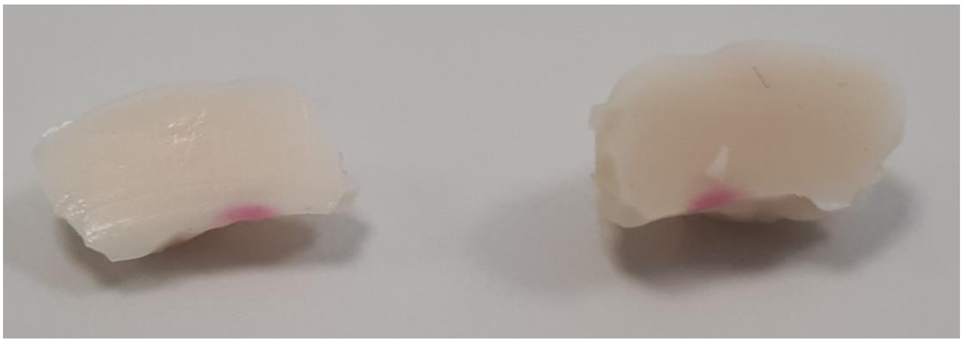

Figure 6-17: Sagittal cut of the 5 second exposure.

This last exposure seemed to reinforce the idea that lesions were originating solely from the point of contact with the VeroWhite phantom when it was present. The exposure also showed what seem to be the entry and exit points of the intersection of the acoustic beam and the mouse skull phantom.

6.4 Conclusions

Testing of the phantom showed that heat can be deposited within the phantom, and the heated regions change colour in response to the temperature increase. The setup indicates that when a bone mimicking interface is present, heat is deposited near the bone. The position of the heating showed entry and exit points for the acoustic beam that could be used to estimate the position of the focus and evaluate targeting.

One interesting effect, observed during exposures, is that the water would be pushed by the radiation force of the acoustic beam, surrounding the skull, or the brain, which produced a thin layer of water behind the target. The possible reflections produced from the water/air interface did not seem to produce a strong effect in the deposition of heat, since that effect was present in all exposure conditions, but different lesions were produced in each of the different sets of exposures.

The heat deposition patterns resulting from the addition of the skull could either have been caused by an increased local absorption, which then propagated through heat diffusion, or due to reflections originating at the interfaces between the different materials. However, considering the attenuation values measured, it would seem that the dominant effect was the localized absorption in the VeroWhite.

This test shows that the thermochromic material can be used in phantoms to locate foci in applications that do not enable the use of standard tools such as hydrophones. Additionaly, the material used in a phantom can provide useful information about hot-spots and acoustic paths.

7 Summary & Conclusions

7.1 Summary & Conclusions

During this project a phantom designed for a QA assessment of the power output and targeting capabilities of a B-mode Ultrasound guided HIFU system has been successfully developed.

The phantom incorporates ideas taken from radiotherapy phantoms into an acoustic phantom, making it adaptable, and allowing the optimisation of the use of the different materials, thus minimising costs while retaining the metrological capabilities of the system. Along with the phantom, a procedure and an evaluation tool have been developed. These facilitate the applicability of the phantom to any clinical environment, requiring only access to MATLAB and photographic equipment.

While the phantom's behaviour is significantly different from tissues behaviour, as the phantom does not include any perfusion processes and the lesions are the result of a simple colour change, as opposed to the process of ablation in human tissues, we find the phantom is still capable of providing valuable QA information and that such differences become irrelevant.

The phantom is an excellent tool for the assessment of power deposition and targeting capabilities of ultrasound guided HIFU systems as the TTTS-HIFU system. Its different constituting elements can be replaced cheaply, and the associated QA tool is accessible as it does not require expensive or complex equipment.

A tissue mimicking phantom material suitable for acoustic and radiation applications, and that is both cheap and reproducible, has been developed successfully.

The TMMs used, based on mixtures with different concentrations of gellan gum, silicon oxide and a thermochromic dye, have been evaluated and characterized across a temperature range from 20 to 45°C. A range of acoustic parameters (attenuation, speed of sound, density, acoustic impedance), thermal parameters (volumetric heat capacity, heat diffusivity, heat conductivity, melting point) and CT numbers have been quantified. The gels have been characterised after exposure to 3 kGy to assess their applicability to radiometry applications. Additional work has evaluated the application of zinc acetate as a doping material, and its effects on attenuation and speed of sound have been reported.

The acquisition of data on the materials has been comprehensive, recording, as it does, different concentrations and temperatures, and is also innovative, with the assessment of the radioresistance of the materials opening up the possibility applications in radiotherapy. The phantom improves on other HIFU phantoms by facilitating its use, improving its readability, producing consistent and repeatable results, and implementing a design fit for US-guided applications.

The applicability of these materials for combination with bone mimics is only limited by the bone mimics themselves and the effect these materials have on the deposition of heat.

7.2 Future work

Future work should evaluate the cavitation threshold of gellan gum samples to be able to establish the maximum acoustic output the system should be exposed to. While it is unlikely that QA tests would need to be done at a level where there was a risk of cavitation, this would be a very adequate characterization for any TMM in order to be able to quantifiably establish limits to the possible applications of the materials. A comparison of gellan gum against other typical gelling agents would be very valuable for high power applications, where the pressures utilized may encroach on the cavitation thresholds of the materials, to better decide which materials should be used.

The applicability of the phantom to radiotherapy applications remains to be tested. The introduction of Gafchromic film into the phantom for evaluation of dose distributions may require the creation of a bigger phantom, so that it becomes better suited for linac beams, for which 10x10 cm^2 fields tend to be tested. This is much bigger than the current 7.4x7.4 cm^2 phantom size although the current design could be used to test CyberKnife-like systems.

The phantom should also be tested for its applicability to MRI guided systems. Safety of the metallic wires used for ultrasound alignment must be assessed. The current phantom design is otherwise suitable for use with MR systems and will be able to produce images, as it contains a large percentage of water. The testing of its targeting accuracy will be enhanced in systems using MR thermometry, but physical inspection should also be able to assess the targeting by measuring the relative positions of the different lesions.

Additional work should be done in finding an appropriate way of isolating the samples to protect them from mechanical damage, similar to how CIRS phantoms are protected by a plastic casing and an outer rubbery saran-based membrane. This would significantly lengthen the shelf life of the phantom and facilitate their use. The phantom could then be tested without the use of a water tank and using acoustic gel to adequate contact between the layers. At that point it may be desirable to add a strong attenuator at the bottom of the phantom.

Isolating the phantom from its environment would also enable the use of ZnOAc, as the formation of crystals only occurred when samples were exposed to solutions with lower ZnOAc concentrations. This would further enable the design of fine-tuned phantoms where the attenuation is increased not only by addition of scatterers, which is not representative of the behaviour of tissues, but by increasing absorption. Furthermore, glycerol could also be added to increase the speed of sound if needed. All these doping agents could then be combined with different scatterers to attempt to fine tune the values of attenuation not only at a single frequency but attempting to change the exponent of the frequency dependence. This could be done by using different scatterers such as cellulose or aluminium oxide, or by using different diameter particles of SiO.

The evaluation of different scatterer combinations could be done without the need to isolate the phantom, but that discussion becomes a lot more interesting in the context of fine tuning the attenuation, absorption, and scattering properties of a phantom.Finally, while it was considered to be undesirable for our project, there could be value in the implementation of a reversible thermochromic dye. A comparison of of the recovery times of various reversible dyes could allow to identify dyes that are less susceptible to producing the misleading results due to the changes in the lesions over time. An assessment of change in the size of lesions in a reversible dye over time would produce very valuable information of the applicability and the windows of time available and whether they are fit for QA purposes.

8 References

1. Podgorsak, E. B. *Radiation Oncology Physics: A Handbook for Teachers and Students*. (IAEA, 2005).
2. Kim, Y., Rhim, H., Choi, M. J., Lim, H. K. & Choi, D. High-Intensity Focused Ultrasound Therapy: an Overview for Radiologists. *Korean J Radiol* **9**, 291–302 (2008).
3. Hill, C. R., Bamber, J. C. & Haar, G. R. ter. *Physical Principles of Medical Ultrasonics*. (John Wiley & Sons, 2004).
4. Vaupel, P., Kallinowski, F. & Okunieff, P. Blood Flow, Oxygen and Nutrient Supply, and Metabolic Microenvironment of Human Tumors: A Review. *Cancer Res* **49**, 6449–6465 (1989).
5. Pennes, H. H. Analysis of tissue and arterial blood temperatures in the resting human forearm. 1948. *Journal of Applied Physiology* **85**, 5–34 (1998).
6. KAMPINGA, H. H. & DIKOMEY, E. Hyperthermic radiosensitization: mode of action and clinical relevance. *International Journal of Radiation Biology* **77**, 399–408 (2001).
7. Franckena, M. *et al.* Radiotherapy and Hyperthermia for Treatment of Primary Locally Advanced Cervix Cancer: Results in 378 Patients. *International Journal of Radiation Oncology*Biology*Physics* **73**, 242–250 (2009).
8. Gerner, E. W. & Leith, J. T. Interaction of Hyperthermia with Radiations of Different Linear Energy Transfer. *International Journal of Radiation Biology and Related Studies in Physics, Chemistry and Medicine* **31**, 283–288 (1977).
9. Civale, J., Rivens, I. & Haar, G. ter. Quality assurance for clinical high intensity focused ultrasound fields. *International Journal of Hyperthermia* **31**, 193–202 (2015).
10. Tsai, J.-S. *et al.* Quality assurance in stereotactic radiosurgery using a standard linear accelerator. *International Journal of Radiation Oncology*Biology*Physics* **21**, 737–748 (1991).

11. Haller, J., Wilkens, V. & Shaw, A. Determination of Acoustic Cavitation Probabilities and Thresholds Using a Single Focusing Transducer to Induce and Detect Acoustic Cavitation Events: I. Method and Terminology. *Ultrasound in Medicine & Biology* **44**, 377–396 (2018).
12. Haller, J. & Wilkens, V. Determination of Acoustic Cavitation Probabilities and Thresholds Using a Single Focusing Transducer to Induce and Detect Acoustic Cavitation Events: II. Systematic Investigation in an Agar Material. *Ultrasound in Medicine & Biology* **44**, 397–415 (2018).
13. Yohannes, I., Kolditz, D., Langner, O. & Kalender, W. A. A formulation of tissue- and water-equivalent materials using the stoichiometric analysis method for CT-number calibration in radiotherapy treatment planning. *Phys. Med. Biol.* **57**, 1173 (2012).
14. Tempany, C. M. C., McDannold, N. J., Hynynen, K. & Jolesz, F. A. Focused Ultrasound Surgery in Oncology: Overview and Principles. *Radiology* **259**, 39–56 (2011).
15. Xu, Z., Hall, T. L., Vlaisavljevich, E. & Lee, F. T. Histotripsy: the first noninvasive, non-ionizing, non-thermal ablation technique based on ultrasound. *Int J Hyperthermia* **38**, 561–575 (2021).
16. Fry, W. J. & Dunn, F. Ultrasound: Analysis and experimental methods in bbiological research in 'Physical Techniques in Biological Research'. in *Special Methods* 261–394 (Elsevier, 1962). doi:10.1016/B978-1-4831-6742-8.50013-6.
17. Ainslie, M. A. & McColm, J. G. A simplified formula for viscous and chemical absorption in sea water. *The Journal of the Acoustical Society of America* **103**, 1671–1672 (1998).
18. Fitch, E. C. *Proactive Maintenance for Mechanical Systems*. (1992).
19. Vlaisavljevich, E. *et al.* Histotripsy-Induced Cavitation Cloud Initiation Thresholds in Tissues of Different Mechanical Properties. *IEEE Trans Ultrason Ferroelectr Freq Control* **61**, 341–352 (2014).
20. Atchley, A. A. *et al.* Thresholds for cavitation produced in water by pulsed ultrasound. *Ultrasonics* **26**, 280–285 (1988).
21. Brace, C. Thermal Tumor Ablation in Clinical Use. *IEEE Pulse* **2**, 28–38 (2011).

22. Diederich, C. J. Thermal ablation and high-temperature thermal therapy: Overview of technology and clinical implementation. *International Journal of Hyperthermia* **21**, 745–753 (2005).

23. Ritchie, K. P., Keller, B. M., Syed, K. M. & Lepock, J. R. Hyperthermia (heat shock)-induced protein denaturation in liver, muscle and lens tissue as determined by differential scanning calorimetry. *International Journal of Hyperthermia* **10**, 605–618 (1994).

24. Xu, Z. *et al.* Controlled Ultrasound Tissue Erosion. *IEEE Trans Ultrason Ferroelectr Freq Control* **51**, 726–736 (2004).

25. Pahk, K. J., Dhar, D. K., Malago, M. & Saffari, N. Ultrasonic Histotripsy for Tissue Therapy. *J. Phys.: Conf. Ser.* **581**, 012001 (2015).

26. Pahk, K. J., Gélat, P., Kim, H. & Saffari, N. Bubble dynamics in boiling histotripsy. *Ultrasound in Medicine & Biology* **44**, 2673–2696 (2018).

27. Pahk, K. J., de Andrade, M. O., Gélat, P., Kim, H. & Saffari, N. Mechanical damage induced by the appearance of rectified bubble growth in a viscoelastic medium during boiling histotripsy exposure. *Ultrasonics Sonochemistry* **53**, 164–177 (2019).

28. Magara, A. *et al.* First experience with MR-guided focused ultrasound in the treatment of Parkinson’s disease. *Journal of Therapeutic Ultrasound* **2**, 11 (2014).

29. Shaw, A. A buoyancy method for the measurement of total ultrasound power generated by HIFU transducers. *Ultrasound Med Biol* **34**, 1327–1342 (2008).

30. ter Haar, G., Rivens, I., Civale, J., Bunton, C. & Symonds-Tayler, R. Quality assurance and field characterisation for MRgHIFU treatments: their need and the challenges presented. *Journal of Therapeutic Ultrasound* **3**, O66 (2015).

31. Dewey, W. C. Arrhenius relationships from the molecule and cell to the clinic. *International Journal of Hyperthermia* (2009) doi:10.3109/02656739409009351.

32. Venkatesh, M. & Shrivastava, S. Medicine: Therapeutic and Other Applications Using Sealed Radiation Sources. in *Encyclopedia of Nuclear Energy* (ed. Greenspan, E.) 280–289 (Elsevier, 2021). doi:10.1016/B978-0-12-819725-7.00175-6.

33. Klein, O. & Nishina, Y. Über die Streuung von Strahlung durch freie Elektronen nach der neuen relativistischen Quantendynamik von Dirac. *Z. Physik* **52**, 853–868 (1929).
34. Solaiappan, G., Singaravelu, G., Prakasarao, A., Rabbani, B. & Supe, S. S. Influence of photon beam energy on IMRT plan quality for radiotherapy of prostate cancer. *Reports of Practical Oncology & Radiotherapy* **14**, 18–31 (2009).
35. Hoheisel, M. Review of medical imaging with emphasis on X-ray detectors. *Nuclear Instruments and Methods in Physics Research Section A: Accelerators, Spectrometers, Detectors and Associated Equipment* **563**, 215–224 (2006).
36. Lohman, T., Wang, Z. & Going, S. B. *Human Body Composition*. (Human Kinetics, 2005).
37. Kubsad, S. S. *et al.* Monte Carlo and convolution dosimetry for stereotactic radiosurgery. *International Journal of Radiation Oncology, Biology, Physics* **19**, 1027–1035 (1990).
38. Brown, A. & Suit, H. The centenary of the discovery of the Bragg peak. *Radiotherapy and Oncology* **73**, 265–268 (2004).
39. *Absorbed Dose Determination in Photon and Electron Beams (TRS-277) IAEA*. (1987).
40. *The Use of Plane-Parallel Ionization Chambers in High-Energy Electron and Photon Beams (TRS-381) IAEA*. (1997).
41. *Absorbed Dose Determination in External Beam Radiotherapy (TRS 398) IAEA*. (2005).
42. Jones, B., Dale, R. G., Deehan, C., Hopkins, K. I. & Morgan, D. A. L. The Role of Biologically Effective Dose (BED) in Clinical Oncology. *Clinical Oncology* **13**, 71–81 (2001).
43. Thariat, J., Hannoun-Levi, J.-M., Sun Myint, A., Vuong, T. & Gérard, J.-P. Past, present, and future of radiotherapy for the benefit of patients. *Nat Rev Clin Oncol* **10**, 52–60 (2013).
44. Nahum, A. E. The Radiobiology of Hypofractionation. *Clinical Oncology* **27**, 260–269 (2015).
45. Song, C. W., Park, H. & Griffin, R. J. Improvement of tumor oxygenation by mild hyperthermia. *Radiat Res* **155**, 515–528 (2001).
46. Raaphorst, G. P., Yang, D. P. & Ng, C. E. Comparison of survival and DNA double strand breaks for mild hyperthermia and low dose rate/pulsed low dose rate irradiation in human cells. *Journal of thermal biology* **25**, 305–311 (2000).

47. Rao, W. & Deng, Z.-S. A Review of Hyperthermia Combined With Radiotherapy/Chemotherapy on Malignant Tumors. *CRB* **38**, (2010).

48. Roizin-Towle, L. & Pirro, J. P. The response of human and rodent cells to hyperthermia. *International Journal of Radiation Oncology*Biology*Physics* **20**, 751–756 (1991).

49. Roti, J. L. R. Introduction: Radiosensitization by hyperthermia. *International Journal of Hyperthermia* **20**, 109–114 (2004).

50. Borasi, G. *et al.* Fast and high temperature hyperthermia coupled with radiotherapy as a possible new treatment for glioblastoma. *J Ther Ultrasound* **4**, 32 (2016).

51. Haar, G. ter & Costa, M. Where Physics Meets Biology: Quantifying the Biological Effects of Combination Treatments of Focused Ultrasound Mediated Heating and Radiotherapy. *Ultrasound in Medicine and Biology* **43**, S33 (2017).

52. Horsman, M. R. & Overgaard, J. Hyperthermia: a Potent Enhancer of Radiotherapy. *Clinical Oncology* **19**, 418–426 (2007).

53. Brüningk, S. C. *et al.* A comprehensive model for heat-induced radio-sensitisation. *International Journal of Hyperthermia* **34**, 392–402 (2018).

54. Alexander Jr., H. R. Hyperthermia and its modern use in cancer treatment. *Cancer* **98**, 219–221 (2003).

55. Durando, G. *et al.* RaCHy-Radiotherapy Coupled with Hyperthermia-18HLT06 EURAMET EMPIR Project. in *2019 IEEE International Symposium on Medical Measurements and Applications (MeMeA)* 1–5 (2019). doi:10.1109/MeMeA.2019.8802202.

56. Costa, M. *et al.* PRESAGE ® as a new calibration method for high intensity focused ultrasound therapy. *J. Phys.: Conf. Ser.* **573**, 012026 (2015).

57. Chen, W.-S., Lafon, C., Matula, T. J., Vaezy, S. & Crum, L. A. Mechanisms of lesion formation in high intensity focused ultrasound therapy. *Acoustics Research Letters Online* **4**, 41–46 (2003).

58. Eranki, A. *et al.* Tissue-mimicking thermochromic phantom for characterization of HIFU devices and applications. *International Journal of Hyperthermia* **36**, 518–529 (2019).

59. Choi, M. J., Guntur, S. R., Lee, K. I., Paeng, D. G. & Coleman, A. A Tissue Mimicking Polyacrylamide Hydrogel Phantom for Visualizing Thermal Lesions Generated by High Intensity Focused Ultrasound. *Ultrasound in Medicine and Biology* **39**, 439–448 (2013).
60. Guntur, S. R. & Choi, M. J. An Improved Tissue-Mimicking Polyacrylamide Hydrogel Phantom for Visualizing Thermal Lesions with High-Intensity Focused Ultrasound. *Ultrasound in Medicine & Biology* **40**, 2680–2691 (2014).
61. Martin, K. & Fernandez, R. A thermal beam-shape phantom for ultrasound physiotherapy transducers. *Ultrasound in Medicine and Biology* **23**, 1267–1274 (1997).
62. Qureshi, F. *et al.* Thermochromic phantom for therapeutic ultrasound daily quality assurance. *J Ther Ultrasound* **3**, P72 (2015).
63. Pennisi, M. *et al.* Neurotoxicity of Acrylamide in Exposed Workers. *Int J Environ Res Public Health* **10**, 3843–3854 (2013).
64. Chin, R. B. *et al.* A reusable perfusion supporting tissue-mimicking material for ultrasound hyperthermia phantoms. *Medical Physics* **17**, 380–390 (1990).
65. Peppas, N. A., Slaughter, B. V. & Kanzelberger, M. A. 9.20 - Hydrogels. in *Polymer Science: A Comprehensive Reference* (eds. Matyjaszewski, K. & Möller, M.) 385–395 (Elsevier, 2012). doi:10.1016/B978-0-444-53349-4.00226-0.
66. Dabbagh, A., Abdullah, B. J. J., Ramasindarum, C. & Abu Kasim, N. H. Tissue-Mimicking Gel Phantoms for Thermal Therapy Studies. *Ultrason Imaging* **36**, 291–316 (2014).
67. Yang, X., Liu, Q., Chen, X., Yu, F. & Zhu, Z. Investigation of PVA/ws-chitosan hydrogels prepared by combined γ-irradiation and freeze-thawing. *Carbohydrate Polymers* **73**, 401–408 (2008).
68. Troia, A., Cuccaro, R. & Schiavi, A. Independent tuning of acoustic and mechanical properties of phantoms for biomedical applications of ultrasound. *Biomed. Phys. Eng. Express* **3**, 025011 (2017).
69. Ambrogio, S. *et al.* A Polyvinyl Alcohol-Based Thermochromic Material for Ultrasound Therapy Phantoms. *Ultrasound in Medicine & Biology* **46**, 3135–3144 (2020).

70. Butterworth, I., Barrie, J., Zeqiri, B., Žauhar, G. & Parisot, B. Exploiting Thermochromic Materials for the Rapid Quality Assurance of Physiotherapy Ultrasound Treatment Heads. *Ultrasound in Medicine & Biology* **38**, 767–776 (2012).

71. Dabbagh, A., Abdullah, B. J. J., Kasim, N. H. A. & Ramasindarum, C. Reusable heat-sensitive phantom for precise estimation of thermal profile in hyperthermia application. *International Journal of Hyperthermia* **30**, 66–74 (2014).

72. Kulčar, R., Friškovec, M., Hauptman, N., Vesel, A. & Gunde, M. K. Colorimetric properties of reversible thermochromic printing inks. *Dyes and Pigments* **86**, 271–277 (2010).

73. Lafon, C. *et al.* Gel phantom for use in high-intensity focused ultrasound dosimetry. *Ultrasound in Medicine & Biology* **31**, 1383–1389 (2005).

74. Schreiner, L. J. Review of Fricke gel dosimeters. *J. Phys.: Conf. Ser.* **3**, 9–21 (2004).

75. Adamovics, J. & Maryanski, M. J. Characterisation of PRESAGE™: A new 3-D radiochromic solid polymer dosemeter for ionising radiation. *Radiat Prot Dosimetry* **120**, 107–112 (2006).

76. Fricke, H. Chemical dosimetry. *Radiation Dosimetry* **2**, 167–239 (1966).

77. Fricke, H. & Morse, S. The chemical action of roentgen rays on dilute ferrosulphate solutions as a measure of dose. *American Journal of Roentgology, Radium Therapy, And Nuclear Medicine* **18**, 430–432 (1999).

78. Shi, Y., Xiong, D. & Zhang, J. Effect of irradiation dose on mechanical and biotribological properties of PVA/PVP hydrogels as articular cartilage. *Tribology International* **78**, 60–67 (2014).

79. Vartak, N. B., Lin, C. C., Cleary, J. M., Fagan, M. J. & Saier, M. H. Glucose metabolism in 'Sphingomonas elodea': pathway engineering via construction of a glucose-6-phosphate dehydrogenase insertion mutant. *Microbiology,* **141**, 2339–2350 (1995).

80. Kang, K. S., Veeder, G. T., Mirrasoul, P. J., Kaneko, T. & Cottrell, I. W. Agar-Like Polysaccharide Produced by a Pseudomonas Species: Production and Basic Properties. *Appl Environ Microbiol* **43**, 1086–1091 (1982).

81. Grasdalen, H. & Smidsrød, O. Gelation of gellan gum. *Carbohydrate Polymers* **7**, 371–393 (1987).

82. Troia, A., Cuccaro, R. & Schiavi, A. New formulations for realization and characterization of homogeneous tissue mimicking materials for HIFU exposures. in *2015 IEEE International Symposium on Medical Measurements and Applications (MeMeA) Proceedings* 125–130 (2015). doi:10.1109/MeMeA.2015.7145185.

83. Amsden, B. Solute Diffusion within Hydrogels. Mechanisms and Models. *Macromolecules* **31**, 8382–8395 (1998).

84. Hot Disk | TPS 2500 S. *Hot Disk* https://www.hotdiskinstruments.com/products-services/instruments/tps-2500-s/.

85. Singh, A. & Singh, H. Time-scale and nature of radiation-biological damage: Approaches to radiation protection and post-irradiation therapy. *Progress in Biophysics and Molecular Biology* **39**, 69–107 (1982).

86. Bilaniuk, N. & Wong, G. S. K. Speed of sound in pure water as a function of temperature. *The Journal of the Acoustical Society of America* **93**, 1609–1612 (1993).

87. Pfennig, A. Kirk-Othmer Encyclopedia of Chemical Technology, 4th Ed., Vol. 10. M. Howe-Grant (Editor). John Wiley & Sons, New York 1993. 1022 S. mit zahir. Abb. und Tab., geb., £ 185.00. *Chemie Ingenieur Technik* **67**, 352–353 (1995).

88. Ilčin, M., Holá, O., Bakajová, B. & Kučerík, J. FT-IR study of gamma-radiation induced degradation of polyvinyl alcohol (PVA) and PVA/humic acids blends. *J Radioanal Nucl Chem* **283**, 9–13 (2010).

89. White, D. R., Booz, J., Griffith, R. V., Spokas, J. J. & Wilson, I. J. Report 44. *Journal of the International Commission on Radiation Units and Measurements* **os23**, NP-NP (1989).

90. McGarry, C. K. *et al.* Tissue mimicking materials for imaging and therapy phantoms: a review. *Phys Med Biol* **65**, (2020).

91. Bamber, J. C. & Hill, C. R. Ultrasonic attenuation and propagation speed in mammalian tissues as a function of temperature. *Ultrasound in Medicine & Biology* **5**, 149–157 (1979).

92. Gammell, P. M., Le Croissette, D. H. & Heyser, R. C. Temperature and frequency dependence of ultrasonic attenuation in selected tissues. *Ultrasound in Medicine & Biology* **5**, 269–277 (1979).

93. Jeanmonod, D. *et al.* Transcranial magnetic resonance imaging-guided focused ultrasound: noninvasive central lateral thalamotomy for chronic neuropathic pain. *Neurosurgical focus* **32**, E1 (2012).

94. Idbaih, A. *et al.* Safety and Feasibility of Repeated and Transient Blood–Brain Barrier Disruption by Pulsed Ultrasound in Patients with Recurrent Glioblastoma. *Clinical Cancer Research* **25**, 3793–3801 (2019).

95. Wu, S.-K. *et al.* Characterization of Different Microbubbles in Assisting Focused Ultrasound-Induced Blood-Brain Barrier Opening. *Sci Rep* **7**, 46689 (2017).

96. Hynynen, K., McDannold, N., Vykhodtseva, N. & Jolesz, F. A. Noninvasive MR Imaging–guided Focal Opening of the Blood-Brain Barrier in Rabbits. *Radiology* **220**, 640–646 (2001).

97. Beccaria, K. *et al.* Ultrasound-induced opening of the blood-brain barrier to enhance temozolomide and irinotecan delivery: an experimental study in rabbits. *Journal of Neurosurgery* **124**, 1602–1610 (2016).

98. Carpentier, A. *et al.* Clinical trial of blood-brain barrier disruption by pulsed ultrasound. *Science Translational Medicine* **8**, 343re2-343re2 (2016).

99. Morse, S. V. *et al.* Rapid Short-pulse Ultrasound Delivers Drugs Uniformly across the Murine Blood-Brain Barrier with Negligible Disruption. *Radiology* **291**, 459–466 (2019).

100. Kyriakou, A. *et al.* A review of numerical and experimental compensation techniques for skull-induced phase aberrations in transcranial focused ultrasound. *International Journal of Hyperthermia* **30**, 36–46 (2014).

101. Moser, D., Zadicario, E., Schiff, G. & Jeanmonod, D. MR-guided focused ultrasound technique in functional neurosurgery: targeting accuracy. *J Ther Ultrasound* **1**, 3 (2013).

102. Batts, A. & Konofagou, E. Targeting Accuracy of Transcranial Power Cavitation Imaging for Blood-Brain Barrier Opening Using a Theranostic Phased Array. in *2020 IEEE*

International Ultrasonics Symposium (IUS) 1–3 (2020). doi:10.1109/IUS46767.2020.9251639.

103. Bakaric, M. *et al.* Measurement of the ultrasound attenuation and dispersion in 3D-printed photopolymer materials from 1 to 3.5 MHz. *The Journal of the Acoustical Society of America* **150**, 2798–2805 (2021).

9 Acknowledgements

I´d like to express my thanks to my supervisory team. Not only for the assistance and guidance they have provided me with through this project, but also for the opportunity they granted me all those year ago when they took me in as a candidate. I´d like to thanks all my colleagues and collaborators, who taught me, assisted me, and performed measurements for me when I was unable.